An X-Ray Study of the Starburst-Driven Outflow in NGC 253

Ikuyuki Mitsuishi

Department of Physics, University of Tokyo.

Institute of Space and Astronautical Science,
Japan Aerospace Exploration Agency.

(ISAS/JAXA)

December 2011

Abstract

It is known that the intergalactic medium contains substantial amount of metals. However, how the metals are transported from galaxies to the intergalactic space is not clear. Galactic-scale starburst-driven outflow is one of the most plausible candidates of the transportation. A nearby starburst galaxy, NGC 253 is suitable to study the hot plasma filled in the disk and the halo produced by starburst activity via X-ray observation. The X-ray halo is considered to be a harbor of galactic-scale outflow which transports the heavy elements yielded by super novae II explosions from galaxies to intergalactic space. We analyzed the hot plasma in NGC 253 by three observatories, *Suzaku*, *Chandra*, and *XMM-Newton*. From a nuclear region of 128×48 pc^{-2}, we found strong Fe I and Fe XXV emission lines, which indicates the hot plasma is produced by 10–1000 SNRs in this small region. X-ray spectra from the superwind region resolved by Hα, the disk, and the halo show several emission lines from O, Ne, Fe, Mg, and Si. The abundance pattern of these regions are similar among the regions and similar to that of the product of type-II supernovae, as the number ratio of O/Fe > 10. This indicates that all of these hot gas has the same origin, and that they originated from type-II supernovae. The density and temperature distribution from the disk to the halo up to 8 kpc are obtained by *Suzaku* with its low background capability. The temperature and density drop sharply in the disk from $kT \sim 0.6$ keV to 0.2 keV, and almost flat in the halo region less than 20 % decrease in the temperature. It suggests that the hot plasma expands adiabatically in the disk and loses its energy. In the halo region, it freely expands. Although the gas cools radiatively, the observed flat temperature profile showed that the cooling is not so fast. The velocity of $\gtrsim 25$ km s^{-1} is suggested. If the expansion velocity in the star-burst region exceeds the Galactic potential, the hot plasma can expel from the disk to the outer space as the outflow.

Contents

1 Introduction

It is known that the intergalactic medium (IGM) contains substantial amount of metals. The metals are thought to originate from stars in galaxies. The mechanism of how the metals are expelled from the galaxies to intergalactic space is, however, still not clear.

Galactic-scale starburst-driven outflow is one of the most plausible candidates of the transportation (Veilleux et al., 2005). The hot gas heated by type-II supernovae in a starburst galaxy may expand to escape the galaxy gravitational potential. There are several observational indications of the outflow from starburst galaxies: hot plasma in halos of galaxies are observed, in which the metal abundance pattern is similar to that of type-II supernovae (Strickland et al., 2004; Yamasaki et al., 2009; Tsuru et al., 2007; Konami et al., 2011); Hα outflow with a velocity of $\sim$ 100 km s^{-1} is also reported (Shopbell & Bland-Hawthorn, 1998; Westmoquette et al., 2011). Nevertheless, the relation between the hot gas in the outflow and the starburst activity, especially the velocity and the kinetic energy of the hot gas is still poorly understood.

In this thesis, we observationally investigated whether the starburst-driven outflow takes place. We observed NGC 253, a nearby edge-on starburst galaxy, with three X-ray observatories: *Suzaku*, *Chandra*, and *XMM-Newton*. The three have different advantages. *Suzaku* has the best sensitibity on the emission lines from diffuse emission. *Chandra* is characterized by its superb angular resolution. *XMM-Newton* has a largest effective area and moderate angular resolution. By utilizing each instrument, we analyzed X-ray emission from NGC 253 from the small scale to the large scale, i.e, the nuclear region at the very center of the galaxy, super-wind region inside the disk, the disk region and the halo region, in order to determine the density, the temperature, and the abundance of each region. Then we discussed whether the hot gas in the disk and halo can be produced by the starburst activity, based on the abundance pattern, the temperature and density distribution, and the activity in the nuclear region.

This thesis consists of the following structure. The outflow phenomena is reviewed in Chapter 2. Chapter 3 describes the instrument. In Chapter 4, data screenings are introduced. In Chapter 5 to 7, analysis and results in four regions of NGC 253, i.e., the nuclear, the innder superwind, the disk and the halo regions, respectively. Finally, in Chapter 8 and 9, our discussions and conclusions are stated.

2 Review

2.1 Starburst-driven Outflow in Spiral Galaxies

It has long been appreciated that galactic-scale outflow activities in galaxies can have a major impact on not only dynamical throughout a mass loading (e.g. Suchkov et al., 1996) but also chemical evolution of a galaxy itself influencing basic galactic properties such as a metal abundance (e.g. Garnett, 2002). Observational facts that metals in the intergalactic medium (IGM) are found at low and high redshifts (Songaila, 1997; Tripp et al., 2000) suggest that more or less some part of all metals ever created now reside outside galaxies. Pagel (2002) have also focused the spotlight on outflows because outflows are considered to be responsible for substance diffusion which gives rise to metal contamination to the IGM.

Galactic-scale starburst-driven outflow is one of the best-studied, best-understood, and arguably most common form of outflow capable of polluting the IGM in both theoretical and observational aspects. In a theoretical standard scenario, starburst-driven galactic outflows are large-angle (opening angles $\geq 30^{\circ}$), multi-phase, galactic-scale ($R \geq$5–20 kpc) outflows and thermal pressure builds up in the interstellar medium (ISM) of a galaxy owing to supernovae shocks that results from formation of stars, and the pressure of the hot gas then removes a fraction of the ISM in the form of an outflow (Veilleux et al., 2005). The pressure of the hot gas is directly related to the rate of supernovae, or, equivalently to the star formation rate. Finally, the hot gas expands and breaks out of the disk of the host galaxy, converting thermal energy into kinetic energy in a bi-polar outflow if the injected energy is enough to break out the gravitational potential of the disk. This tenuous wind-fluid hot gas heated by supernovae shocks mainly emits X-rays, sweeps up and accelerates cooler denser ambient disk and halo gas. Thus, X-ray emitting hot gas is considered to be a direct tracer of such outflows.

From observations, Spatially-resolved X-ray images of well-studied starburst galaxies show striking X-ray halos or plumes that can extend out to 10 kpc or more away from the disk continuously along with the galaxy minor axis (e.g. Yamasaki et al., 2009; Strickland et al., 2004; Tsuru et al., 2007; Konami et al., 2011), which has been interpreted as direct evidence for galactic-scale outflows. Figure 2.1 shows an example

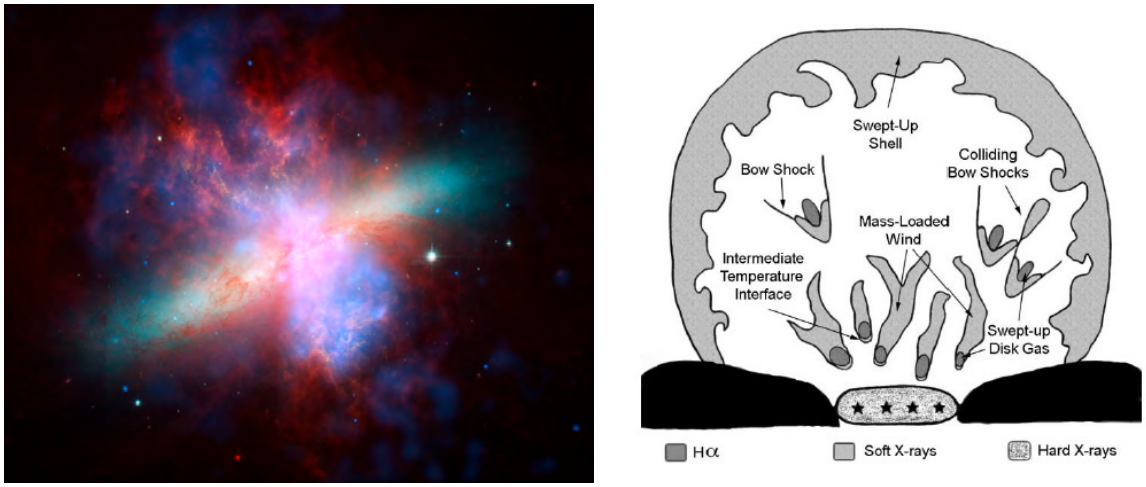

Figure 2.1 Left: a composite image of the nearby starburst galaxy M82 (`http://chandra.harvard.edu/photo/2010/m82/`). Chandra X-ray observatory data in blue, optical data from the Hubble Space Telescope in green and orange, and infrared data from the Spitzer Space Telescope in red. Image is 7.9 arcmin across corresponding to ∼10 kpc. Right: Figure 15 in Cooper et al. (2008). Schematic of the Hα and X-ray emission arising in a starburst-driven outflow and their spatial relationship.

of the starburst-driven outflow in the nearby starburst galaxy M82 and a schematic picture of the outflow. Starburst galaxies with the outflow account for ∼20 % of the high mass star formation (and hence metal production) in the local Universe, having been observed in all galaxies where the average star formation rate per unit area exceeds $\Sigma_{\rm SF} \geq 10^{-1}\ M_\odot\ {\rm yr}^{-1}\ {\rm kpc}^{-2}$ (Heckman et al., 1990; Lehnert & Heckman, 1996; Veilleux et al., 2005). This indicates that starburst galaxies in the local Universe play an important role in a star formation history from the present to the future. Furthermore, adding the following fact that the UV-selected star-forming galaxies at z ∼ 2–4 that may dominate the total star formation density at these redshifts are known to drive powerful winds that appear to be physically identical to local superwinds (e.g. Pettini et al., 2001; Shapley et al., 2003), hence to study starburst galaxies can provide us an important hint of dynamical and chemical evolutions in the Universe throughout the outflow activity.

X-ray emission from the central region of a starburst galaxy is known to be complex because of blending of various kinds of point sources and diffuse emission. Although point source emission typically dominates the hard band, in some starburst galaxies including NGC 253, the emission line from He-like Fe XXV is observed, suggesting the existence of a high temperature plasma (e.g. Pietsch et al., 2001; Boller et al., 2003; Ranalli et al., 2008). Supernova remnants (SNRs), associated with starburst activity, are considered to be a candidate of the origin. Moreover, two of the galaxies

exhibit Fe I fluorescent line (e.g. Boller et al., 2003; Strickland & Heckman, 2007). The coexistence of highly ionized and neutral Fe lines suggests the coexistence of hot and cold gases. Thus, this complex Fe K line structure is informative on the origin of the emission and the gas structure of starburst galaxies. The origin of the neutral line is, however, still poorly known.

2.2 Observational Studies of NGC 253

NGC 253 is a famous nearby edge-on Sc-type starburst galaxy and its active star formation is located in the central half kpc of this barred spiral galaxy. Despite the intensity of approximately 20 $M_{\odot}$ yr^{-1} kpc^{-2} in star formation surface density, among the highest in the sample of nearby circumnuclear starbursts in Kennicutt (1998) when mergers are excluded, the starburst luminosity ($L_{1-1000\ \mu\mathrm{m}} \sim 2\times10^{10} L_{\odot}$ in Radovich et al. (2001)), star formation rate with 1.4–9.5 $M_{\odot}$ (Grimm et al., 2003) and optical B-band luminosity of 6×10^{9} $L_{\odot}$ (Strickland et al., 2004) are not outstanding compared to other starburst galaxies (e.g. Lehnert & Heckman, 1996; Strickland et al., 2004). Geometrically, the edge-on which easily allows us to distinguish the disk from the halo and also its large apparent diameter make it a suitable target to study the spatial distribution of emission features. Thus, NGC 253 is archetypal and, therefore, one of the best targets for starburst studies. Indeed, NGC 253 has received a great deal of attention in all of wavelength ranging from radio to gamma-ray, even today (e.g. Sakamoto et al., 2011; Kaneda et al., 2009; Mitsuishi et al., 2011; Abdo et al., 2010) and it is found that NGC 253 holds interesting universal and unique structures, e.g., the complex nuclear, the inner superwind and the disk-halo outflow characterized by various wavelength ranges.

In this section, we introduce a part of observational results of NGC 253 focusing on signature 4 regions, i.e., hereafter the nuclear region, the inner superwind region, the disk region and the halo region, in both dynamical and chemical aspects associated with the outflow activity and discussions in this thesis. Not only X-rays but also other wavelength results in various scales from pc to dozens of kpc are introduced since a galaxy contains various configurations as a normal matter such as atom, molecular, ionized gas and dust characterized by various wavelength ranges.

2.2.1 Radio, IR and optical properties of NGC 253

■**Nuclear region** The nuclear region is located on just the central 100 pc region in NGC 253 including the galactic center and considered to be the most intense starburst

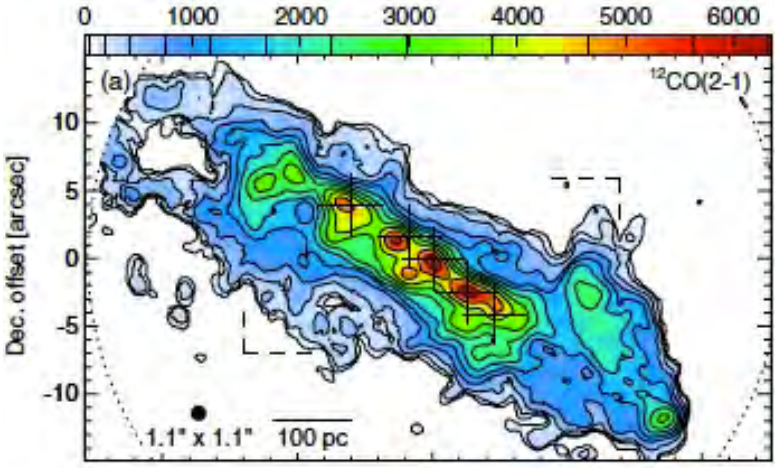

Figure 2.2 Left: ^{12}CO(2–1) molecular line map in the center of NGC 253 as an example in Sakamoto et al. (2011). The synthesized beam (FWHM) is shown in the top-right and bottom-left corners, respectively. The five brightest peaks of 1.3 mm continuum are marked with plus signs and the unit of integrated intensity is K km s^{-1}. The nth contour is at 46× n^2.

region in NGC 253 characterized by radio observations which reflects features of cold materials such as molecular clouds associated with the star formation activity. Sakamoto et al. (2011) reports observational results of molecular gas in the nuclear region of NGC 253 at 20–40 pc (1″–2″) resolution. They detected extremely dense molecular clouds on the order of $N_{H2} \sim 10^{24}$ cm^{-2} as shown in Figure 2.2. For the ^{12}CO-H_2 conversion factor of the nuclear region of NGC 253, this factor has been estimated to be 4, 1.7, 1.3 and 0.3 in units of 10^{20} cm^{-2} (K km s^{-1})$^{-1}$ by Israel et al. (1995); Weiß et al. (2008); Martín et al. (2010); Mauersberger et al. (1996), respectively. They also observed five clumps of dense (10^4 $M_\odot$ pc^{-2}) and warm (∼50 K) gas standing out in the central molecular zone at arcsecond resolution and these molecular complexes are spatially associated with the centimeter-wave radio peaks such as those found by Turner & Ho (1985). This coincidence, as well as the coincidence of the molecular complexes and other star formation tracers, suggests that these molecular complexes are the sites of the most intense star formation in the nuclear region of NGC 253. This complex structure of the nuclear molecular clouds is one the noteworthy properties of NGC 253.

■**Superwind region** The superwind region is placed just next to the nuclear region. In this region, 100 pc-scale outflow with a velocity of ∼100 km s^{-1} is observed and characterized by optical observations. In a galaxy, optical lights are emitted by mainly stars and ionized gases heated by e.g., massive stars associated with the star

formation activity and interactions between cold materials and the hot plasma.

Westmoquette et al. (2011) leads to some very important results on the inner several 100 pc scale outflow using deep optical narrow-band Hα(+[N II]) data and suggestions for also a disk-halo connection. NGC 253 holds two outflows at different levels of scale; one is the several 100 pc-scale outflow from nearby the nuclear to the inner disk and the other is the several kpc-scale disk-halo outflow stated above. The term of superwind in this thesis hereafter represents the former. They confirm the presence of an expanding outflow cone between radii of 280 and 660 pc from the nucleus, oriented along the minor axis and reveal that deprojected outflow speeds is a few 100 km s^{-1} that increases with distance above the plane as shown in Figure 2.3. Figure 2.3 right also indicates an important fact that the coherence of the Hα velocities in the outflow region (35″–55″ in x-axis) means that the 10^4 K, Hα-emitting gas layers must be quite thin and dynamically stable compared to a chaotic central region (>55″). This geometrical constraint is consistent with another Hα observation (Matsubayashi et al., 2009), an X-ray observation (Strickland et al., 2000) and a prediction of hydrodynamical models of superwinds (Strickland & Stevens, 2000) based on the superwind of M82. They also demonstrate that a significant fraction of the wind optical emission lines arise from shocked gas, with localized pockets/filaments of strongly shocked gas by using the [N II]/Hα and [S II]/Hα line ratios. Finally, they discuss the connection between the inner superwind and the kpc-scale outflow and conclude that it seems to be difficult to explain the link due to a large disparity in scales between the collimated, conical inner superwind and the widely spaced X-ray outflow.

In the chemical aspect, Origlia et al. (2005) shows stellar abundance patterns of O, Si, Mg, Ca, Al and C relative to Fe around the nuclear region and mainly the superwind region from near-IR spectra whose emissions is likely to be dominated by massive red supergiants with several atomic and molecular absorption lines. Resultant abundance patterns are more than those of the expected considering the solar abundance, which suggests that the stellar abundance is contaminated by type-II supernovae associated with the star formation activity.

■**Disk region** The disk region is outside the nuclear and superwind regions and characterized by mainly an optical B-band emission because massive stars associated with the star formation activity emit mainly in B band. In B-band, a detailed optical photometry of NGC 253 is reported in Pence (1980) (see Figure 2.4 top). The maximum detected dimension is $60' \times 26'$, or 44×19 kpc assuming the distance to 2.5 Mpc which indicates that more or less massive stars such as O and B stars exist

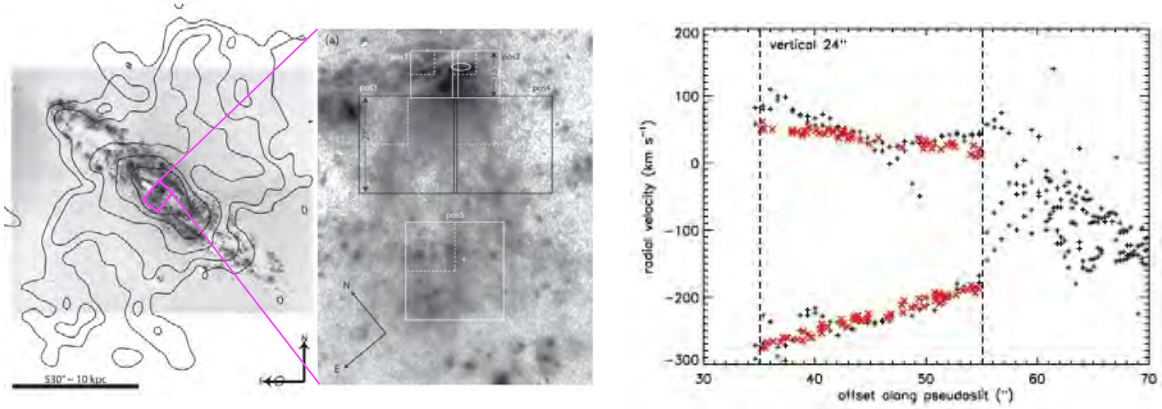

Figure 2.3 Figures 2 (a), 10 and 19 in Westmoquette et al. (2011). Left: the extent of the large-scale X-ray outflow seen with *ROSAT* is shown in contours overlaid on the WFI Hα image and a close-up view of the inner superwind. Right: an example of a position-velocity plot derived from Hα observations for the inner superwind.

even outside the disk. They also evaluated a breakdown to the total B luminosity by modeling a luminosity profile. It is well known that spiral galaxies can be resolved into two main components: a spheroidal bulge obeying the $R^{1/4}$ law, and a highly flattened disk with an exponential luminosity distribution (e.g. de Vaucouleurs, 1958; Yoshizawa & Wakamatsu, 1975). They added the third component representing the light from the spiral arms to explain the bump in the luminosity profile (see Figure 2.4 bottom left between $5'$ and $10'$). The best fits for both major and minor axes are shown in Figure 2.4 and each contribution to the total B luminosity is 15, 59 and 26 %, respectively. The B band luminosity profile is often utilized to define the optical disk of a galaxy and in the case of NGC 253, its B25 is about $28' \times 7'$. Throughout this paper, we adopt this size to the term of disk.

Heesen et al. (2009) proposes a new idea by a disk wind as a transportation method rather than the starburst activity in the nuclear region. They measure the cosmic-ray bulk speed as 300 ± 30 km s^{-1} which is constant over the extent of the disk suggesting the presence of a disk wind. In Heesen et al. (2011), the disk wind speed is calculated to be $\sim$150 km s^{-1} or more by subtracting Alfvén speed with respect to the magnetic field in spite of the large uncertainty.

■**Halo region** The halo region is outside the disk region and characterized by infrared observations. IR emissions in a starburst galaxy originate from the dust in ISM mainly heated by young massive stars associated with the star formation activity. Thus, in order to understand the dust distribution, IR observations are very useful.

It is known that NGC 253 folds a uniquely-shaped halo reaching out to $\sim$10 kpc

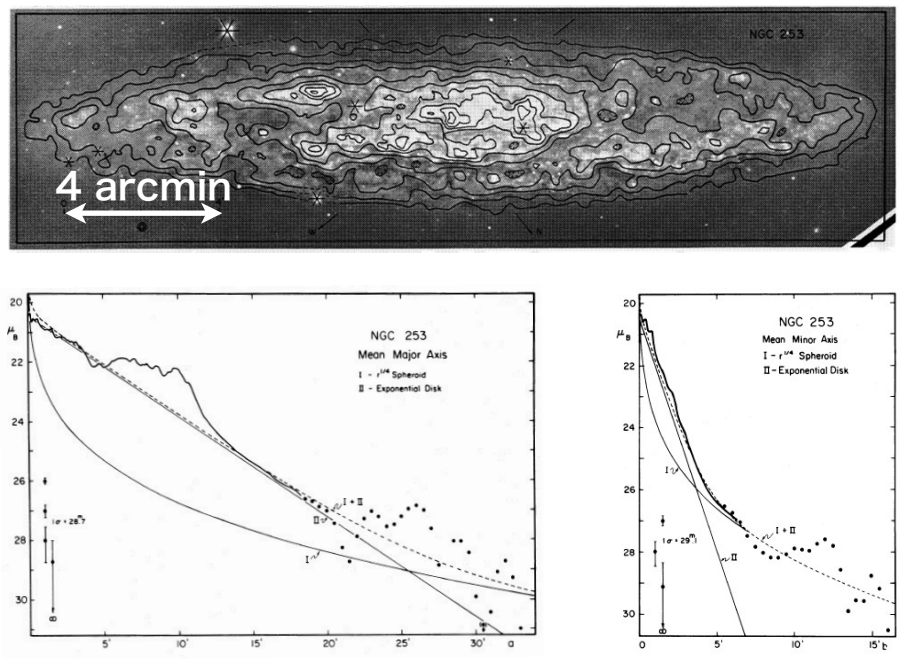

Figure 2.4 Figure 2, 9 and 10 in Pence (1980). Top: isophotes of NGC 253 superposed on a photograph reproduced from the *Cape Atlas* (Evans 1957). Contours are spaced 0.333 magnitude intervals with the outer contour at $\mu_{\rm B}$=23.0. Levels fainter than $\mu_{\rm B}$=21.0 were smoothed with a 3×3 Gaussian weighted filter whose half-power beam width is shown at the lower left. Bottom: luminosity profile of mean major axis (left) and mean minor axis. Dashed and the other lines are a sum of a spheroidal bulge and an exponential disk components and each component of the bulge and the disk, respectively.

perpendicular to the optical disk and this halo structure is often called a horn describing its shape of the halo as shown in Figure 2.5 (Kaneda et al., 2009). Interestingly, this FIR "horn" halo clearly traces an X-ray emitting gas as shown in Figure 2.5 and therefore this structure is also one of the striking properties of NGC 253 which gives us a crucial hint on a picture of the outflow. According to the 90 μm/140 μm ratio map of NGC 253 in Kaneda et al. (2009), they reveal that the temperatures of the dust in the halo are significantly lower than those in the nuclear and disk regions and especially two specific regions in the halo (red circles in Figure 2.5) show higher temperatures of 33 K and 31 K in the horn and the other regions, respectively compared to elsewhere in the halo below 20 K. They point out that there exist extra dust heating sources in the halo and this may be caused by shock through interaction between the X-ray halo and pre-existing H I clouds for the horn region. They also estimate an averaged dust outflow velocity to 300–2000 km^{-1} assuming a homogeneity of the dust in the hot plasma and the distance from the disk to 9 kpc and predicts that the

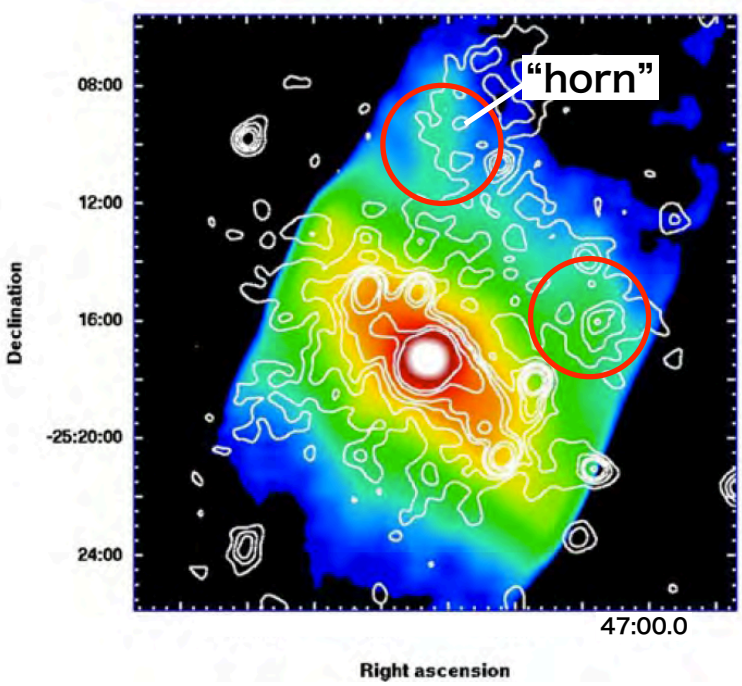

Figure 2.5 Figure 2 top in Kaneda et al. (2009). *ROSAT/PSPC* X-ray (0.1-2.4 keV) contour map of NGC 253 overlaid on the WIDE-S (90 μm) image. Two red circles correspond to higher temperature regions in the halo region determined by the 90 μm/140 μm ratio map in Kaneda et al. (2009). The color levels and contours are drawn at surface brightness levels of 10, 20, 40, 80, 160, 320, 640, 1280 and 2560 MJy str^{-1} and 1.6, 3.0, 4.4, 5.8, 9.3 and 12.8×10 counts s^{-1} arcmin^{-2} for IR and X-ray observations, respectively.

dust would be escaping from the gravitational potential of NGC 253 considering the escape velocity of 280 km s^{-1}.

In a chemical aspect, Webster & Smith (1983) shows a radial profile of the abundance of oxygen relative to hydrogen in various H II regions from 5 kpc to 10 kpc perpendicular to the disk plane in the halo region . Despite a lack of information in the inner region, the abundance of oxygen relative to hydrogen in the outer region seems to be smaller than that of the inner region and ranges from 0.35 to 0.87 compared to that of the solar abundance (Anders & Grevesse, 1989). NGC 253 is categorized in high-metallicity starburst galaxies (O'Halloran et al., 2006). Carral et al. (1994) argues that a gas phase Si abundance is about ∼30–50 % solar in central 250 pc H II region.

Finally, a schematic picture including signature 4 regions described above is shown in Figure 2.6.

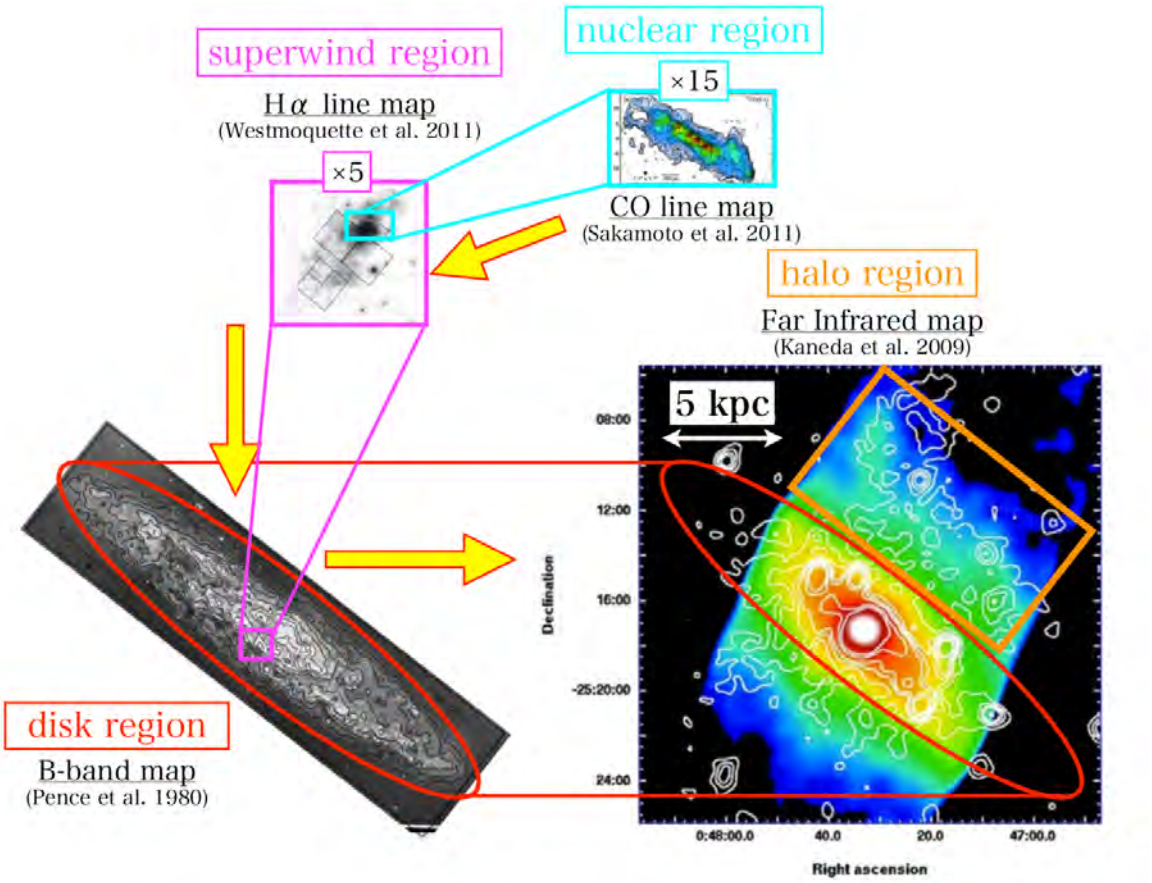

Figure 2.6 Signature 4 regions characterized by multi-wavelength observations in NGC 253.

2.2.2 X-ray properties of NGC 253

In this section, the previous X-ray observations of NGC 253 are introduced for each remarkable region, i.e., the nuclear, the inner superwind, the disk and the halo regions described above.

■**Nuclear region** Ptak et al. (1997) by *ASCA* reveals the first clear detections of O, Ne, Fe, Mg, S and Si emission lines with the first high spectral resolution and suggests the existence of Fe K line from the integrated NGC 253 spectrum including the nuclear region. In the following year, the 6.7 keV Fe K line is detected clearly by *BeppoSAX* (Persic et al., 1998) but with a not good angular resolution over arcmin. Pietsch et al. (2000) detects different diffuse emission components in the nucleus, disk and halo with a high spatial resolution of 20–60 arcsec but only in the energy band below 2.4 keV. Because emissions from the nuclear region are expected to be hard enough to emit the Fe K emission line and its apparent size is very compact on the order of 10 arcsec based on other observations in different wavelength ranges, e.g., radio, X-ray properties in the nuclear region are poorly understood in details but known to be complex.

The first *XMM-Newton* observation of NGC 253 (Pietsch et al., 2001) shows the first results with a high spatial resolution of ∼10 arcsec and good spectral quality for the nuclear region. They extracted a spectrum in just the nuclear region and this spectrum can be modeled by a three temperature plasma (∼0.6, 0.9 and 6 keV) with the higher temperatures increasingly absorbed. They argue that the high temperature component most likely originates from the starburst nucleus considering resultant SN rate of 0.2 yr^{-1} and physical parameters, e.g., intensity and equivalent width. On the other hand, Weaver et al. (2002) by *Chandra* characterized by its sub-arcsecond angular resolution advocates that an X-ray emission at the nuclear region is a combination of a power law plus emission from a photoionized plasma by a low-luminosity AGN (hereafter LLAGN) not diffuse plasmas due to its high equivalent widths of the observed emission lines.

Recently, a heavily absorbed object (N_H=7.5×10^{23} cm^{-2}) is found in Müller-Sánchez et al. (2010) and they conclude that this object is an obscured LLAGN or a spatially resolved super star cluster brightening up in X-rays most probably due to young supernovae or supernova remnants. The existence of the buried AGN and the origin of this complex emission are very important to pursue the central engine as a heating source and extract the whole picture for the outflow phenomena of NGC 253.

In the chemical aspect, although Ptak et al. (1997) tries to extract chemical abundances of hot gas and a half of heavy metal abundances can be constrained for the first time, a heavy contamination from the disk region prevents them acquiring genuine chemical compositions due to its large angular resolution.

■**Superwind region** Vogler & Pietsch (1999), Pietsch et al. (2000) and Strickland et al. (2000) provide the first spatially-resolved image of the inner superwind region and show this outflow to be a well-collimated, limb-brightened and kiloparsec-scale by taking surface brightness profiles (see Figure 2.7 left). They also find a correlation in morphology between the observed X-ray outflow and the known Hα outflow cone, which suggests that both X-ray and Hα emission come from low volume filling factor regions of interaction between the fast energetic wind of SN ejecta and the denser ambient interstellar medium not from the wind fluid itself. Strickland et al. (2000) estimates a contribution of volume-filling, metal-enriched, wind fluid itself to the observed X-ray emission and concludes that only $\leq$20 % of the total X-ray emission can come from the wind fluid itself. Although from a high spectral resolution observation with E/ΔE $\sim$200–800 in 0.35–2.5 keV by RGS on board *XMM-Newton* Bauer et al. (2007) also confirms that the O VIII (18.80–19.17 Å) line distribution as a tracer of the inner superwind extends out to $\sim$750 pc along with the minor axis, this emission is not limb-brightened. The RGS image suggests that the outflow cone is filled with clumpy-distributed O VIII and this clumpiness may be caused by mass-loading, i.e., the turbulent process of mixing in ambient ISM and infalling material.

In the chemical aspect, Strickland et al. (2000) extracts abundance ratios of Z_α $\sim$0.30 solar for α elements and $Z_{\rm Fe}$ $\sim$ 0.13 solar, respectively, but can not vary abundances of each element because of the lack of the number of photons. However, owing to strongly subsolar abundance ratios, they conclude that these results are contaminated by systematic errors, e.g., the uncertain and spatially varying instrument response.

■**Disk and halo regions** In a surface brightness profile of diffuse hot ISM below 1 keV along with a minor axis in starburst galaxies no definitive change is found Strickland et al. (2004) to distinguish the disk from the halo regions. Therefore, throughout this thesis, we adopt the optical disk B25 as the term of the disk.

Pietsch et al. (2000) shows that diffuse emission from the disk is heavily absorbed and follows the spiral structure and it can be described by a thin thermal plasma spectrum (kT=0.7 keV, intrinsic luminosity L_X=1.2$\times$10^{39} erg s^{-1}), and most likely reflects a mixture of sources such as X-ray binaries, SNRs and the hot ISM. On

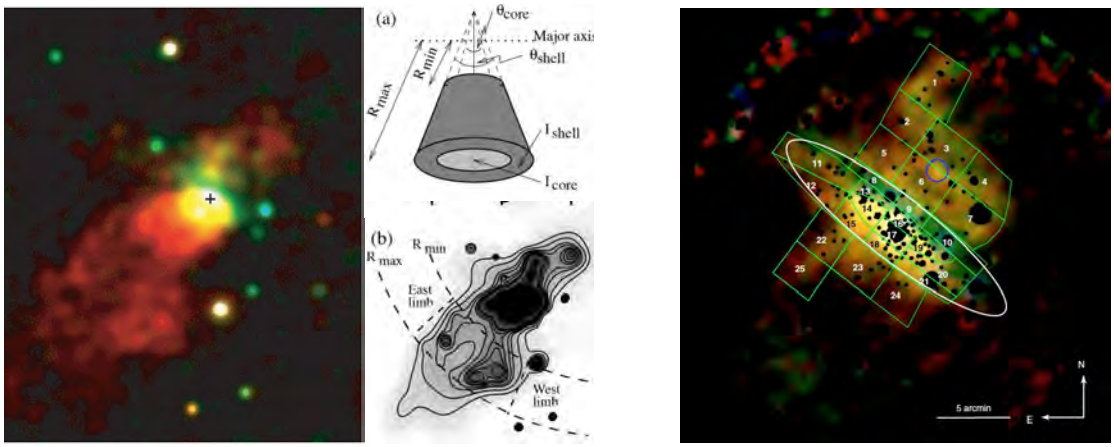

Figure 2.7 Left: Figures 1 in Weaver et al. (2002), 5 (a) and (b) in Strickland et al. (2000). Three-color composite *Chandra* X-ray image of the central $1'.75 \times 2'$. Red, yellow and blue correspond to the X-ray energy band of 0.23–1.5 keV, 1.5–4.5 keV and 4.5–8.0 keV, respectively. The plus sign marks the position of the radio core (Turner & Ho, 1985). (a) Spatial model assumed from the obtained surface brightness profiles and (b) *Chandra* 0.3–2.0 keV image showing the region of clear limb-brightening between R_{min} and R_{max}. Right: Figure 4 in Bauer et al. (2008). Adaptively smoothed EPIC PN image. The colors correspond to the energy bands of 0.2–0.5 keV in red, 0.5–1.0 keV in green and 1.0–2.0 keV in blue, respectively. Overplotted in white is the inclination corrected optical B25 ellipse and the center of the galaxy is marked with a black cross.

the other hand, the halo emission is modeled by a two temperature plasma with temperatures of 0.13 and 0.62 keV. *Chandra* observation (Strickland et al., 2002) leads to almost the same results as Pietsch et al. (2000) for both the disk and halo regions. Based on the hardness ratio analysis, they also indicates that there is no statistically significant evidence for any spatial variation in the spectral properties of the diffuse emission over scales from several ∼400 pc to ∼3 kpc. The most powerful and detailed analysis for the disk and halo regions of NGC 253 is achieved by Bauer et al. (2008). In Bauer et al. (2008), spectral analysis is performed for divided 25 regions individually as shown in Figure 2.7 right. As a result, most of the emission from the halo is at energies below 1 keV, while in the disk, also emission at higher energies is present. Models for spectral fits of the disk need two thermal plasmas with temperatures of between 0.1 and 0.3 keV and between 0.3 and 0.9 keV for the soft and the hard component. To model the spectra in the halo, two thermal plasmas with temperatures of around 0.1 and 0.3 keV are needed.

In the chemical aspect, subsolar abundances of $0.3^{+4.7}_{-0.2}$ $Z_\odot$ and $0.4^{+4.6}_{-0.3}$ $Z_\odot$ for the northwestern halo and the disk with large error bars are obtained (Bauer et al., 2008). Also in this analysis, abundances of each element are not free.

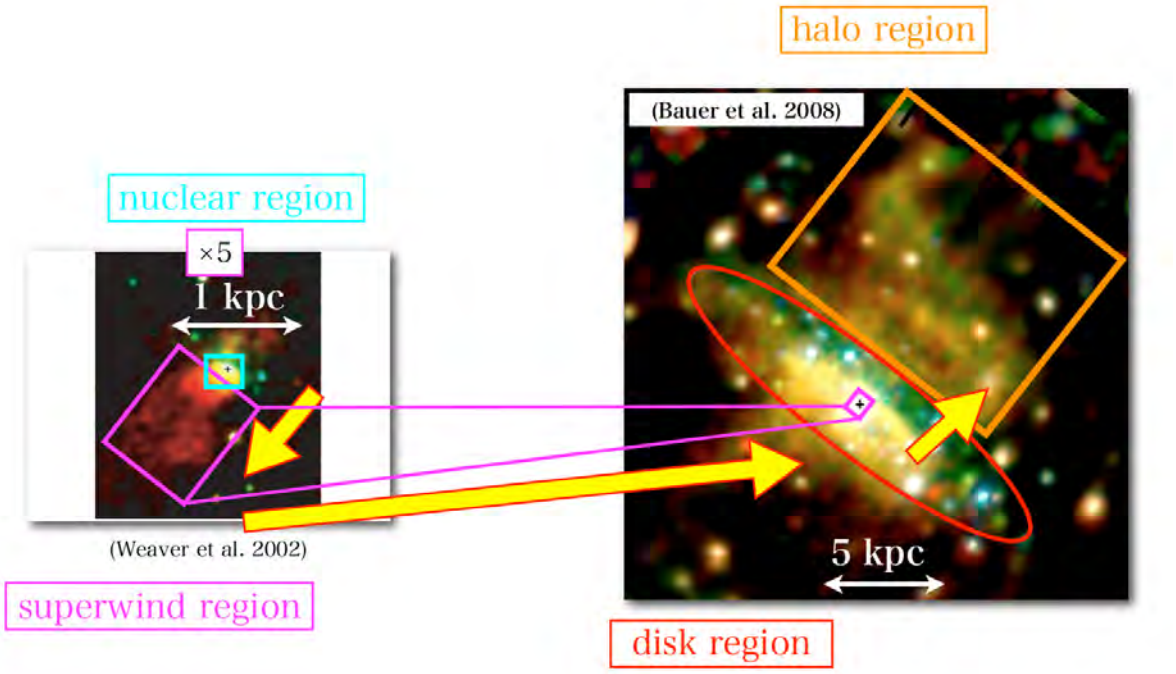

Figure 2.8 Signature 4 regions in NGC 253 by X-ray observations.

X-ray images for the above 4 regions are indicated in Figure 2.8.

2.3 Remaining issues

As shown above, the starburst galaxies are considered to be important for the pollution of the IGM through the outflow. Observations in various wavelengths have revealed the complex structure and characteristics. However, the direct evidence of the outflow, i.e., observations of the gas in the outflow, is still quite poor.

The gas in the outflow is expected to be hot, and hence to be observed in X-rays. Indeed, the hot gas is observed in the halo of the galaxies. However, the halo gas is so thin and faint that the origin of the gas has not been constrained. Although the metal abundance has been recently measured with Suzaku for a few starburst galaxies (Yamasaki et al., 2009; Konami et al., 2011), indicating the type-II supernova origin, limitation in statistics and angular resolution makes it difficult to remove the contamination of bright sources in the disk. More importantly, dynamics of the halo gas, such as velocity or kinetic energy, has hardly constrained. Therefore, it is still not clear whether the halo gas originates from the outflow due to starburst activity, nor whether the halo gas is gravitationally bound to the galaxy or escaping from the

galaxy. Sensitive X-ray measurement of NGC 253, one of the best-studied starburst galaxy, is hence desirable to give us more understanding of the outflow mechanism.

3 Instruments

3.1 *The Suzaku* Satellite

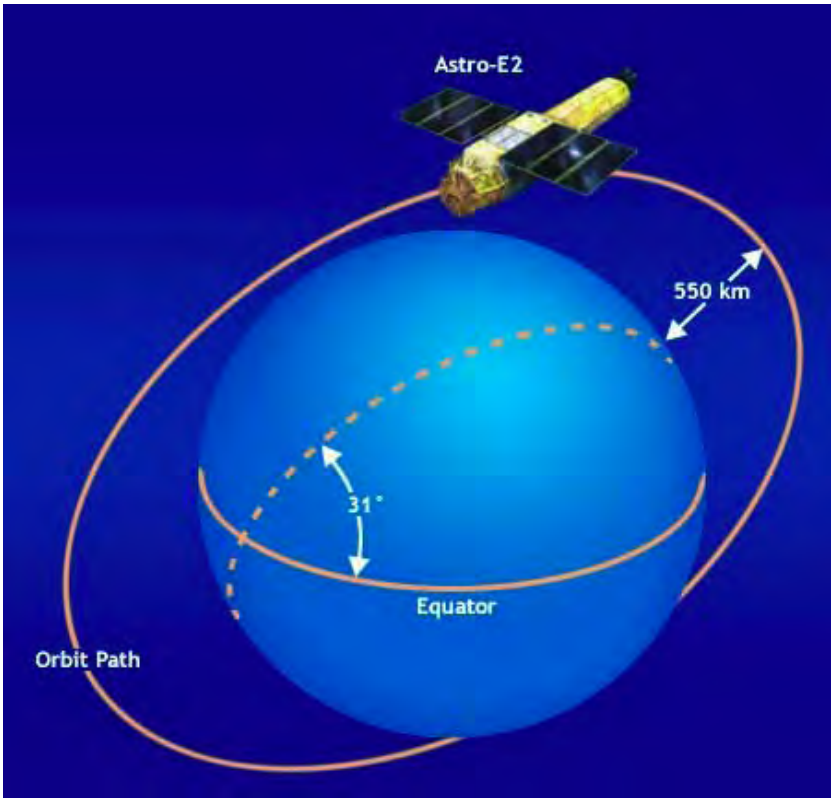

Figure 3.1 The *Suzaku* orbit. This figure was taken by the *Suzaku* technical description.

Suzaku, the Japanese 5th X-ray astronomical satellite, was launched on July, 2005 (Mitsuda et al., 2007). *Suzaku* is placed in a near-circular orbit with an apogee of 568 km, an inclination of 31.9 deg degrees, and an orbital period of about 96 minutes (figure 3.1). The maximum slew rate of the spacecraft is 6 degrees/min, and setting to the final attitude takes ∼10 minutes, using the star trackers.

The scientific payload of *Suzaku* (figure 3.2) initially consisted of three distinct co-aligned scientific instrument. There are four X-ray sensitive imaging CCD cameras (X-ray Imaging Spectrometer, or XISs), three front-side illuminated (FI; energy range 0.4–12 keV corresponding to XIS0, XIS2, XIS3) and one back-side illuminated (BI; energy range 0.2–12 keV for XIS1), capable of moderate energy resolution. Each XIS is located in the focal plane of a dedicated X-ray telescope. The second instrument is

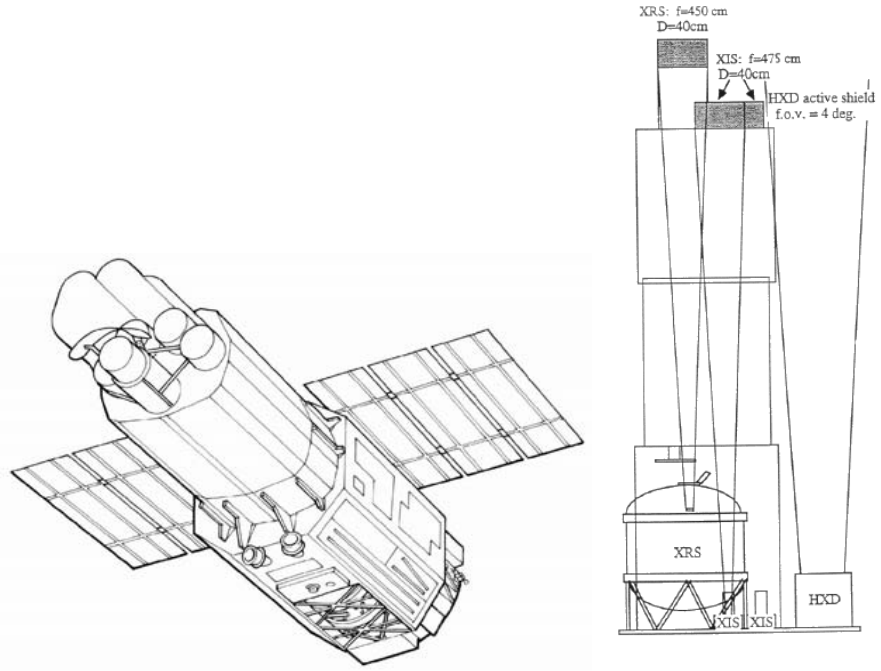

Figure 3.2 Left: Schematic picture of the *Suzaku* satellite. Right: A side view of the instruments and telescopes on *Suzaku* Mitsuda et al. (2007).

the non-imaging, collimated Hard X-ray Detector (HXD), which extends the bandpass of the observatory to much higher energies with its 10–600 keV pointed bandpass. The X-ray Spectrometer (XRS) is no longer operational.

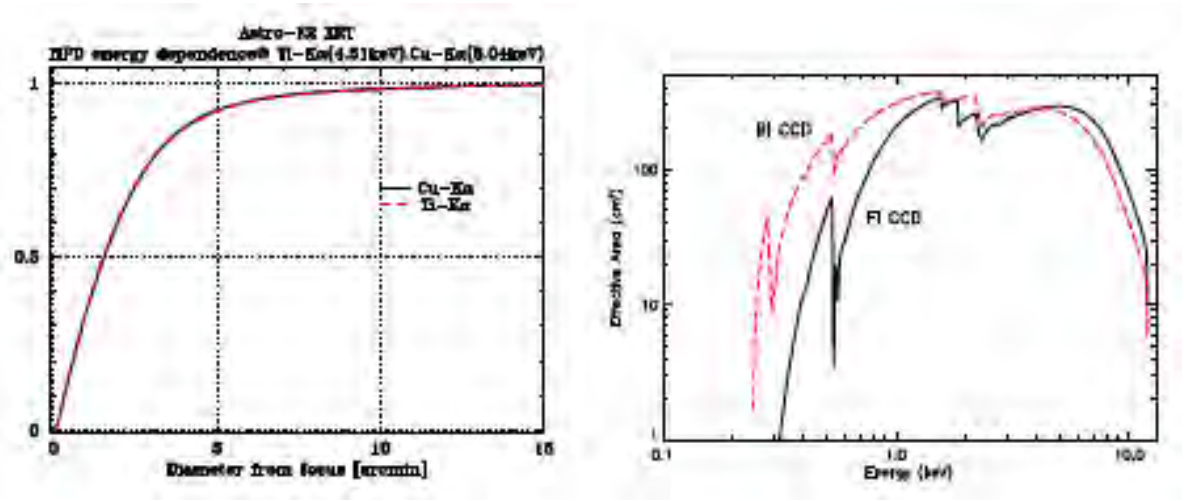

Figure 3.3 Left: The Encircled Energy Function (EEF) showing the fractional energy within a given radius for one quadrant of the XRT-I telescopes on *Suzaku* at 4.5 and 8.0 keV (Serlemitsos et al., 2007). Right: XIS effective area of one XRT + XIS system, for the FI and BI CCDs. no contamination.

All of the instruments on *Suzaku* operate simultaneously. Each of the co-aligned

XRTs features an X-ray mirror with an angular resolution (expressed as Half-Power Diameter, or HPD) of ∼2' (figure 3.3). Figure 3.3 shows the total effective area of the XIS + XRT. K-shell absorption edges from oxygen (0.54 keV) and aluminum (1.56 keV) in the blocking filter are present, as well as a number of weak M-shell features between 2–3 keV arising from the gold coated on the front surface of the XRT reflector.

The four XISs are true imagers, with a large field of view (∼18'×18'), and moderate spectral resolution.

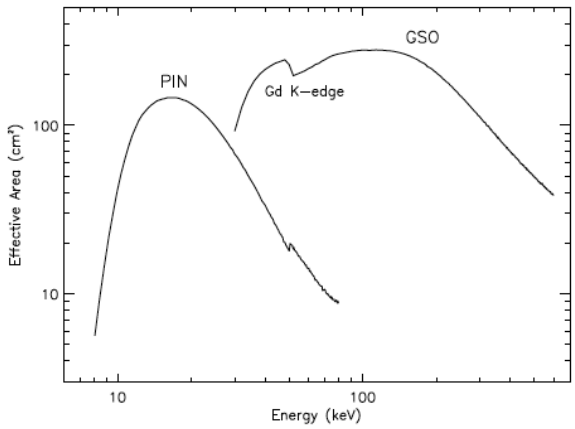

Figure 3.4 Total effective area of the HXD detectors, PIN and GSO, as a function of energy (Kokubun et al., 2007).

The HXD is a non-imaging instrument with an effective area of ∼260 cm^2, featuring a compound-eye configuration and an extremely, low background. It extends the bandpass of the mission with its nominal sensitivity over the 10–600 keV band (figure 3.4). The HXD consist of two types of sensors: 2 mm thick silicon PIN diodes sensitive over 10–60 keV, and GSO crystal scintillators placed behind the PIN diodes covering 30–600 keV. The HXD field of view is actively collimated to 4.5°×4.5° by the well-shaped BGO scintillators, which in combination with the GSO scintillators, are arranged in the so-called phoswich configuration. At energies below ∼100 keV, an additional passive collimation further reduces the field of view to 34'×34'. The energy resolution is ∼3.0 keV (FWHM) for the PIN diodes, and $7.6/\sqrt{E}$% (FWHM) for the scintillators (where E is energy in MeV). The HXD time resolution for both sensor is 60 μs. While the HXD is intended mainly to explore the faintest hard X-ray sources, it can also tolerate very bright sources up to ∼10 Crab. The HXD also has an all-sky monitor (the Wide-band All-sky Monitor, or WAM), which can detect GRB and other sources. In this paper, we only used XISs.

3.1.1 X-ray Telescopes (XRTs)

Suzaku has five light-weight thin-foil X-ray Telescopes (XRTs). The XRTs have been developed jointly by NASA/GSFC, Nagoya University, Tokyo Metropolitan University, and ISAS/JAXA. These are grazing-incidence reflective optics consisting of compactly nested, thin conical elements. Because of the reflectors' small thickness they permit high density nesting and thus provide large collecting efficiency with a moderate imaging capability in the energy range of 0.2–12 keV, all accomplished in telescope units under 20 kg each.

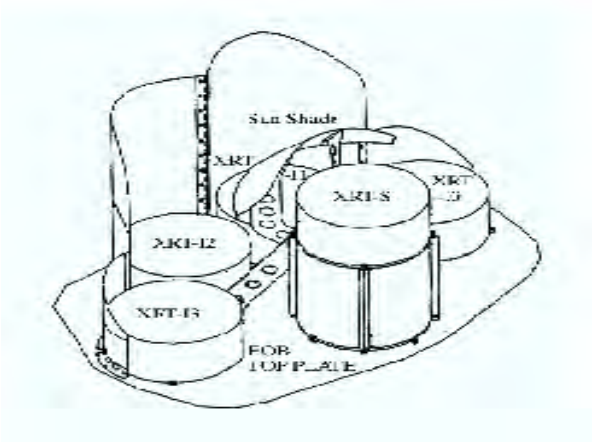

Figure 3.5 Layout of the XRTs on the *Suzaku* spacecraft Serlemitsos et al. (2007).

Four XRTs onboard *Suzaku* (XRT-I) are used for the XIS, and the other XRT (XRT-S) is for the XRS. The XRTs are arranged on the top plate of the Extensible Optical Bench (EOB) in the manner shown in figure 3.5 The external dimensions of the 4 XRT-Is are the same (see table 3.1, which also includes a comparison with the *ASCA* telescopes).

The HPD of the XRTs range from $1'.8$ to $2'.3$, which is the diameter within half of the focused X-ray is enclosed. The angular resolution dose not significantly depend on the energy of the incident X-ray in the energy range of *Suzaku*, 0.2–12 keV. The effective areas are typically 440 cm^2 at 1.5 keV and 250 cm^2 at 8 keV. The focal lengths are 4.75 m for the XRT-I. Individual XRT quadrants have their component focal lengths deviated from the design values by a few cm. The optical axis of the quadrants of each XRT are aligned within $2'$ from the mechanical axis. The field of view (the diameter for a half of the effective area) for XRT-Is is about $17'$ at 1.5 keV and $13'$ at 8 keV.

Table 3.1 Telescope dimensions and design parameters of XRT-I, compared with *ASCA* XRT.

	Suzaku	*ASCA*
Number of telescopes	4	4
Focal length	4.75 m	3.5 m
Inner diameter	118 mm	120 mm
Outer diameter	399 mm	345 mm
Height	279 mm	220 mm
Mass/Telescope	19.6 kg	9.8 kg
Number of nested shells	175	120
Reflectors/Telescope	1400	960
Geometric area/Telescope	873 cm^2	558 cm^2
Reflecting surface	Gold	Gold
Substrate material	Aluminum	Aluminum
Substrate thickness	155 μm	127 μm
Reflector slant height	101.6 mm	101.6 mm

Basic Component of XRT

The *Suzaku* XRTs consist of closely nested thin-foil reflectors, reflecting X-ray at small grazing angles. An XRT is a cylindrical structure, having the following layered components: 1. a thermal shield at the entrance aperture to help maintain a uniform temperature; 2. a pre-collimator mounted on metal rings for stray light elimination; 3. a primary stage for the first X-ray reflection; 4. a secondary stage for the second X-ray reflection; 5. a base ring for structural integrity and interface with the EOB. All these components, expect the base rings, are constructed in 90° segments. Four of these quadrants are coupled together by interconnect-couples and also by the top and base rings (see figure 3.6). The telescope housings are made of aluminum for an optimal strength to mass ratio.

Including the alignment bars, collimating pieces, screws and washers, couplers, retaining plates, housing panels, and rings, each XRT-I consists of over 4112 mechanically separated parts. In total, nearly 7000 qualified reflectors were used and over 1 million cm^2 of gold surface was coated.

Reflectors

Each reflector consists of a substrate also made of aluminum and an epoxy layer that

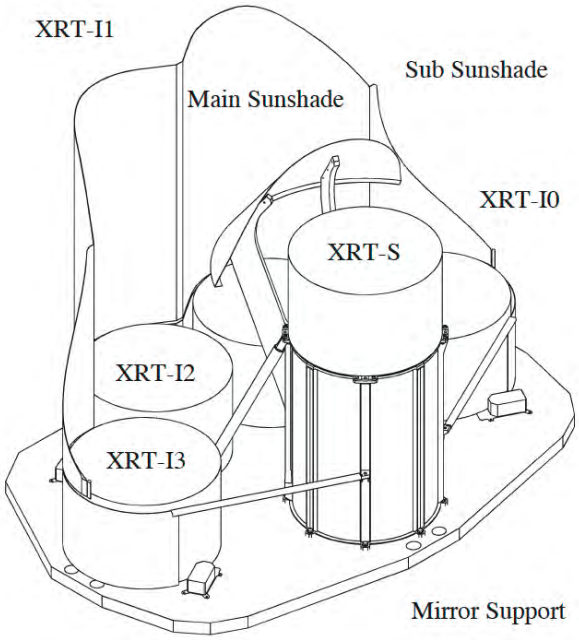

Figure 3.6 A *Suzaku* X-ray Telescope Serlemitsos et al. (2007).

couples that the reflecting gold surface to the substrate. The reflectors are nominally 178 μm in thickness. In shape, each reflector is a 90° segment of a section of a cone. The cone angle is designed to be the angle of on-axis incidence for the primary stage and 3 times that for the secondary stage. They are 101.6 mm in slant length and with radii extending approximately from 60 mm at the inner part to 200 mm at the outer part. All reflectors are positioned with grooved alignment bars, which hold the foils at their circular edges. There are 13 alignment bars at each face of quadrant, separated at approximately 6.4° apart.

In the *Suzaku* XRTs, the conical approximation of the Wolter-I type geometry is used. This approximation fundamentally limits the angle resolution achievable. More significantly, the combination of the figure error in the replication mandrels and the imperfection in the thermo-forming process (to about 4 micrometers in the low frequency components of the figure error in the axial direction) limits the angular resolution to about 1 arcmin (Misaki et al., 2004)

Pre-collimator

The pre-collimator, which blocks off stray light that otherwise would enter the detector at a larger angle than intended, consists of concentrically nested aluminum foils similar to that of the reflector substrates (Mori et al., 2005). They are shorter, 22 mm in length, and thinner, 120 μm in thickness. They are positioned in a fashion

Table 3.2 Design parameters for pre-collimator.

	XRT-I
Number of collimators	4
Height	32 mm
Blade substrate	aluminum
Blade thickness	120 μm
Blade height	22 mm
Height from blade top to reflector top	30 mm
Number of nested shells	175
Blade/Telescope	700
Mass/Collimator	2.7 kg

similar to that of the reflectors, by 13 grooved aluminum plates at each circular edge of the pieces. They are installed on top of their respective primary reflectors along the axial direction. Due to their smaller thickness, they do not significantly reduce the entrance aperture in that direction more than the reflectors already do. Pre-collimator foils do not have reflective surfaces (neither front nor back). The relevant dimensions are listed in table 3.2.

Thermal Shields

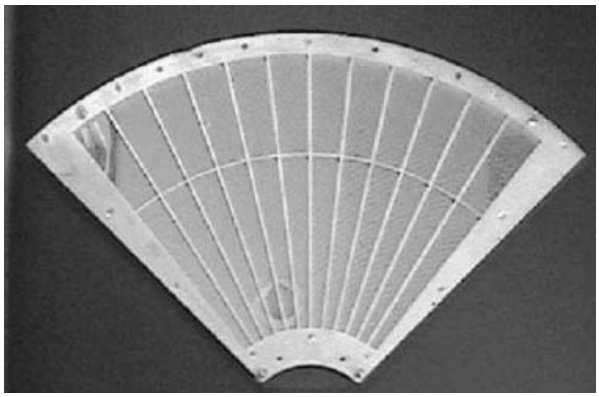

Figure 3.7 A thermal shield. This picture was adapted from Serlemitsos et al. (2007).

The *Suzaku* XRTs are designed to function in a thermal environment of 20±7.5 °C. The thermal shield (figure 3.7) is mechanically sustained by a frame made of aluminum, with a thickness of 4 mm. The frame has thirteen spokes which are along the alignment bars of the XRT. A stainless steel mesh with a wire pitch, width and

thickness of 3 mm, 0.1 mm and 0.15 mm, respectively. Finally, polyethylene teleftalate (PET) film as thin as 0.24 μm, coated with aluminum layer with thickness of 30 nm on the surface oriented to the space, is adhered to the mesh with epoxy. The reflectors, due to its composite nature and thus its mismatch in coefficients of thermal expansion, suffer from thermal distortion that degrades the angular resolution of the telescopes in temperature outside this range. Thermal gradient also distorts the telescope in a larger scale. Even though sun shields and other heating elements on the spacecraft help in maintaining a reasonable thermal environment, thermal shields are integrated on top of the pre-collimator stage to provide the needed thermal control.

Focal Positions and Angular Resolutions

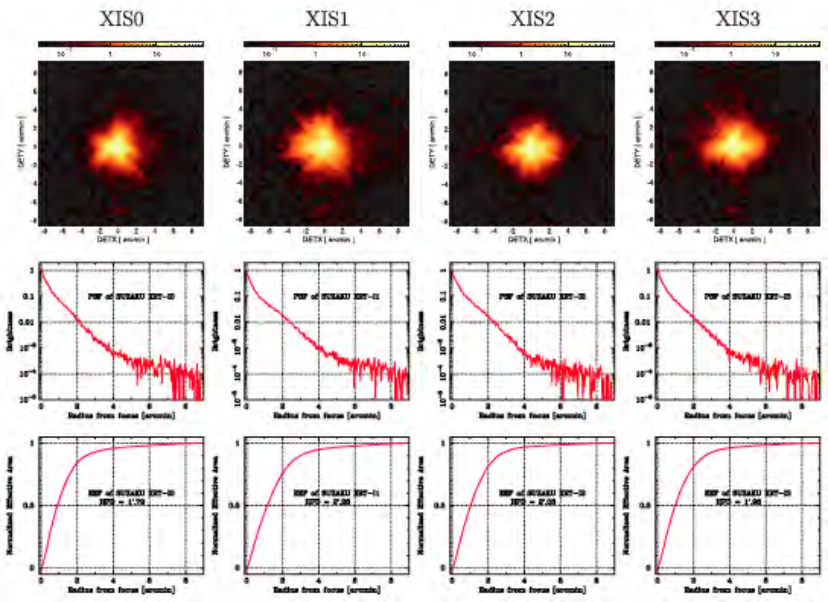

Figure 3.8 Image, Point-Spread Function (PSF), and EEF of the four XRT-I modules in the focal plane Serlemitsos et al. (2007). All the image are binned with 2×2 pixels followed by being smoothed with a Gaussian with a sigma of 3 pixels, where the pixel size is 24 μm. The EEF is normalized to unity at the edge of the CCD chips (a square of 17'.8 on a side). With this normalization, the HPD of the XRT-I0 thorough I3 is 1'.8, 2'.3, 2'.0 and 2'.0, respectively.

Verification of the imaging capability of the XRTs has been made with the data of SS Cyg in quiescence taken during 2005 November 2 01:02UT-23:39UT. Total exposure time was 41.3 ks. SS Cyg is selected for this purpose because it is a point source and moderately bright (3.5, 5.9, 3.7 and 3.5 c s^{-1} for XIS0 through XIS3), and hence, it is needless to care about pile-up even at the image core. Figure 3.8 shows the images and the point-spread functions (PSFs) of the all the XRT-I+XIS modules. The HPD is obtained to be 1′.8, 2′.3, 2′.0 and 2′.0 for XRT-I0, 1, 2 and 3, respectively. These

values are in general consistent with those expected from ground-based calibration measurements.

Optical Axes, Effective Area and Vignetting Functions

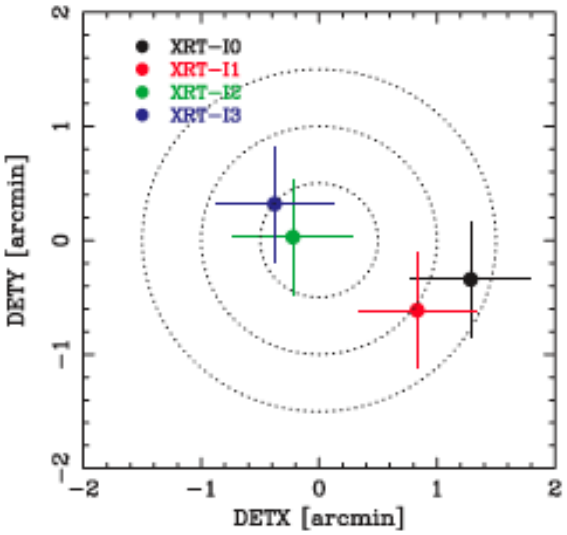

Figure 3.9 Locations of the optical axis of each XRT-I module in the focal plane determined from the observations of the Crab Nebula in 2005 August-September. This figure implies that the image on each XIS detector becomes brightest when a target star is placed at the position of the corresponding cross. The dotted circles are drawn every 30" in radius from the XIS-default position. This figure was adapted from Serlemitsos et al. (2007).

A series of offset observations of the Crab observations were carried out in August and September at carious off-axis angles of $0'$, $3'.5$ and $7'$. The intensity of the Crab nebula is evaluated for each pointing and for each XIS module separately. By finding the maximum throughput angle, we also have obtained a direction of the optical axis of each telescope. The result is shown in figure 3.9. The optical axes locate roughly within $1'$ from the XIS aim point. This implies that the efficiency of all the XRT-Is is more than 97 % even at 10 keV when we observe a point source on the XIS aim point.

The vignetting curves calculated by the ray-tracing simulator are compared with the observed intensities of the Crab Nebula at carious off-axis angles in figure 3.10. These figures roughly show that effective area is calibrated to within ∼10% over the XIS field of view. We expect most of these deviations can be attributed to scattering of the optical axis orientations of the four quadrants within a telescope.

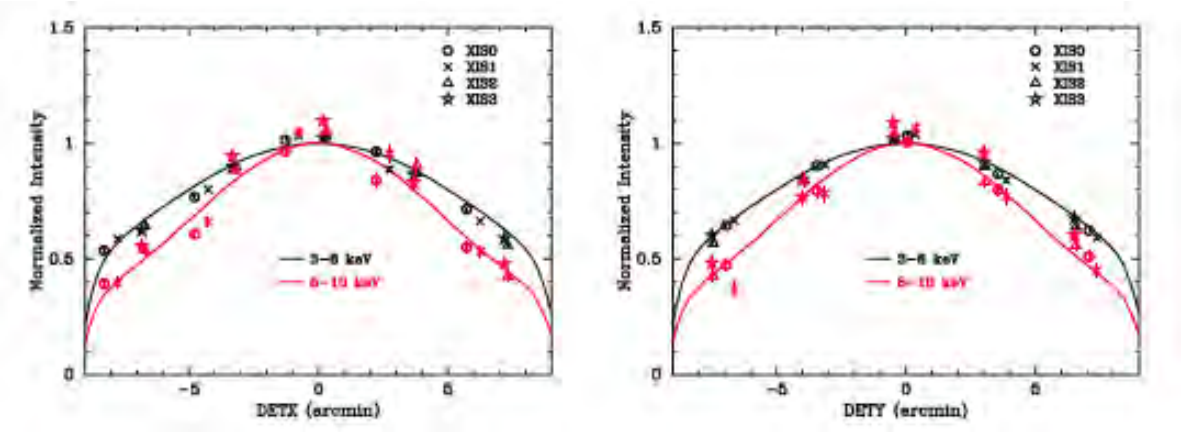

Figure 3.10 Vignetting of the four XRT-I modules using the data of the Crab Nebula taken during 2005 August 22–27 in the two energy bands 3–6 keV and 8–10 keV. The model curves are calculated with the ray-tracing simulator with the spectral parameters of $N_{\rm H} = 0.33 \times 10^{22}$ cm^{-2}, photon index = 2.09, and the normalization = 9.845 photons cm^{-2} s^{-1} keV^{-1} at 1 keV. Note that the abrupt drop of the model curves at $\sim 8'$ is due to the source approaching the detector edge. The excess of the data points of XIS1 is probably due to insufficient calibration of the BI CCD. This figure was adapted from Serlemitsos et al. (2007).

Stray Light

In-flight stray-light observations were carried out with the Crab Nebula at off-axis angles of $20'$ (4 pointings), $50'$ (4 pointings) and $120'$ (4 pointings) in August and September. Figure 3.11 shows an example of $20'$-off image of XRT-I3 together with simulation results of the same off-axis angle for the cases with and without pre-collimator. It is seen that the pre-collimator works for reducing the stray light in orbit.

Figure 3.12 shows angular responses of the XRT-I at 1.5 and 4.5 keV up to 2 degrees. The effective area is normalized at on-axis. The integration area is corresponding to the detector size of XIS ($17'.8 \times 17'.8$). The plots are necessary to plan observations of diffuse sources or faint emissions near bright sources, such as outskirts of cluster of galaxies.

The three solid lines in the plot correspond to different parameters of ray-tracing program while the crosses are the normalized effective area using the Crab pointings. For example, the effective area of the stray light at 1.5 keV is $\sim 10^{-3}$ at angles smaller than 70 arcmin off axis and $< 10^{-3}$ at angles larger than 70 arcmin off. The measured flux of stray lights are in good agreement with that of ray-tracing within an order.

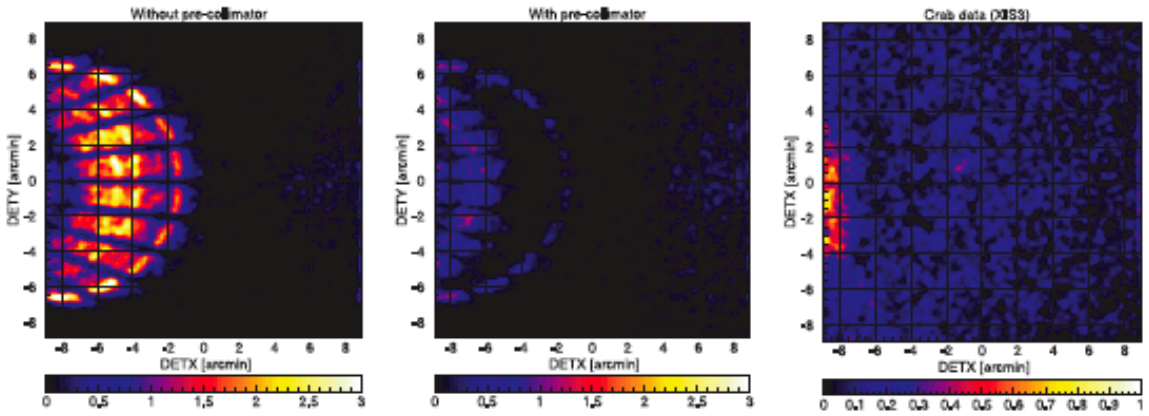

Figure 3.11 Focal plane images formed by stray light (Serlemitsos et al., 2007). The left and middle panels show simulated images of a monochromatic point-like source of 4.51 keV locating at (DETX, DETY) = (-20′, 0’) in the cases of without and with the pre-collimator, respectively. The radial dark lanes are the shades of the alignment bars. The right panels is the in-flight stray image of the Crab Nebula in the 2.5–5.5 keV band located at the same off-axis angle. The unit of the color scale of this panel is counts per 16 pixels over the entire exposure time of ∼8.4 ks. the counting rate from the whole image is 0.78±0.01 c s^{-1} including background. Note that the intensity of the Crab Nebula measured with XIS3 at the XIS-default position is 458±3 c s^{-1} in the same 2.5–5.5 keV band. All the images are binned with 4×4 pixels followed by being smoothed with a Gaussian with a sigma of 2 pixels, where the pixel size is 24 μm.

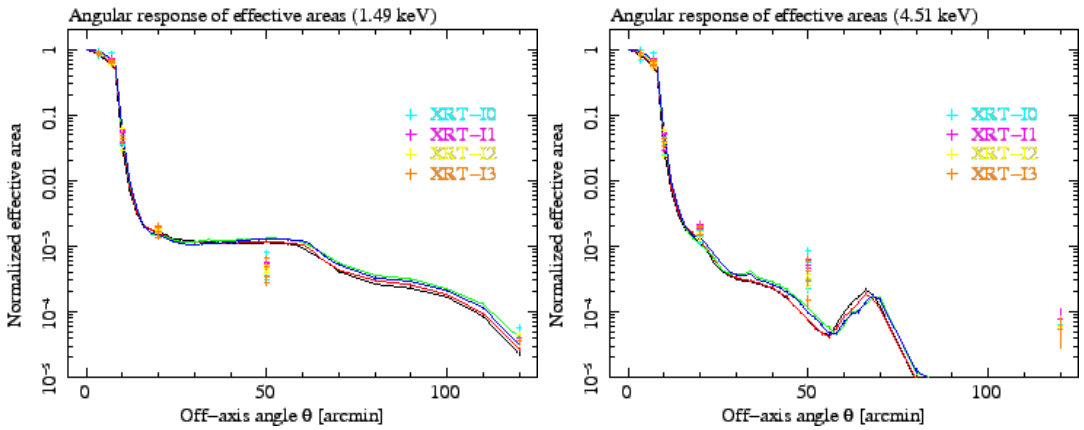

Figure 3.12 Angular responses of the XRT-I at 1.5 (left) and 4.5 keV (right) up to 2 degrees (see *Suzaku* technical description). The effective area is normalized at on-axis. The integration ares is corresponding to the detector size of XIS (17′.8×17′.8). The three solid lines in the plots correspond to different parameters of ray-tracing program while the crosses are the normalized effective area using the Crab pointings.

3.1.2 X-ray Imaging Spectrometer (XIS)

Overview of the XIS

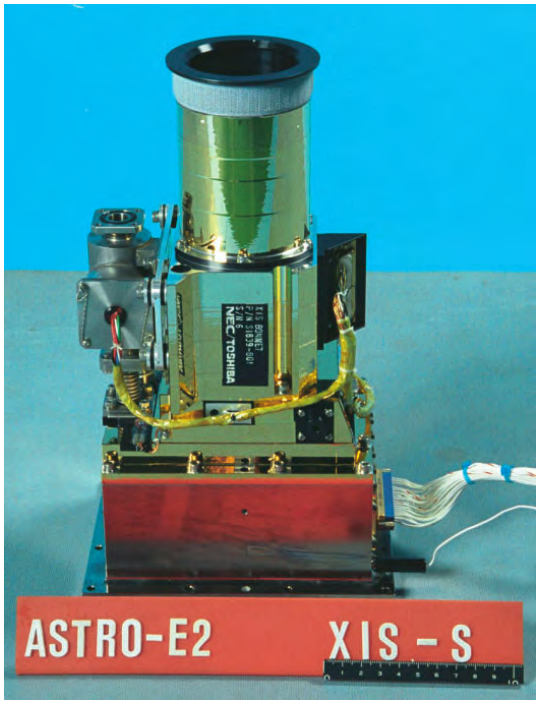

Figure 3.13 The XIS detector before installation onto *Suzaku*. This picture was adapted from Koyama et al. (2007).

Suzaku has four X-ray Imaging Spectrometers (XIS), which are shown in figure 3.13. These employ X-ray sensitive silicon charge-coupled devises (CCDs), which are operated in a photon-counting mode, similar to that used in the *ASCA* SIS, *Chandra*/ACIS, and *XMM-Newton* EPIC. In general, X-ray CCDs operate by converting an incident X-ray photon into a charge cloud, with the magnitude of charge proportional to the energy of the absorbed X-ray. This charge is then shifted out onto the gate of an output transistor via an application of time-varying electrical potential. This results in a voltage level (often referred to as "pulse height") proportional to the energy of the X-ray photon.

The four *Suzaku* XISs are named XIS0, XIS1, XIS2 and XIS3, each located in the focal plane of XRT; those telescopes are known respectively as XRT-I0, XRT-I1, XRT-I2, and XRT-I3. Each CCD camera has a single CCD chip with an array of 1024×1024 picture elements ("pixels"), and covers an $17'.8 \times 17'.8$ region on the sky. Each pixel is 24 μm square, and the size of the CCD is 25 mm×25 mm. One of the XISs, XIS1, uses a back-side illuminated (BI) CCD, while the other three use a front-side illuminated (FI) CCDs. The XIS has been partially developed at MIT (CCD sensors,

analog electronics, thermo-electric coolers, and temperature control electronics), while the digital electronics and a part of the sensor housing were developed in Japan, jointly by Kyoto University, Osaka University, Rikkyo University, Ehime University and ISAS/JAXA.

A CCD has a gate structure on one surface to transfer the charge packets to the readout gate. The surface of the chip with the gate structure is called the "front side". A front-side illuminated CCD (FI CCD) detects X-ray photons that pass through its gate structures, i.e. from the front side. Because of the additional photo-electric absorption at the gate structure, the low-energy quantum detection efficiency (QDE) of the FI CCD is rather limited. Conversely, a back-side illuminated CCD (BI CCD) receives photons from "back", or the side without the gate structure. For this purpose, the undepleted layer of the CCD is completely removed in the BI CCD, and a thin layer to enhance the electron collection efficiency is added in the back surface. A BI CCD retains a high QDE even in sub-keV energy band because of the absence of gate structure on the photon-detection side. However, a BI CCD tends to have a slightly thinner depletion layer, and the QDE is therefore slightly lower in the high energy band. The decision to use only one BI CCD and three FI CCDs was made because of both the slight additional risk involved in the new technology BI CCDs and the need to balance the overall efficiency for both low and high energy photons.

To minimize the thermal noise, the sensors need to be kept at ~ -90 °C during observations. This is accomplished by thermo-electric coolers (TECs), controlled by TEC Control Electronics, or TCE. The Analog Electronics (AE) drives the CCD clocks, reads and amplifies the data from the CCDs, performs the analog-to-digital conversion, and routes the signals to the Digital Electronics (DE). The AE and TCE are located in the same housing, and together, they are called the AE/TCE23 is used for XIS-S2 and S3. The digital electronics system for the XISs consists of two Pixel Processing Units (PPU) and one Main Processing Unit (MPU); PPU01 is associated with AE/TCE01, and PPU23 is associated with AE/TCE23. The PPUs receive the raw data from AE, carry out event detection, and send event data to the MPU. The MPU edits and packets the event data, and sends them to the satellite's main digital processor.

To reduce contamination of the X-ray signal by optical and UV light, each XIS has as Optical Blocking Filter (OBF) located in front of it. The OBF is made of polyimide with a thickness of 1000 Å of aluminum (400 Å on one side and 800 Å on the other side). To facilitate the in-flight calibration of the XISs, each CCD sensor has two ^{55}Fe calibration sources. One is installed on the door on illuminate the whole

chip, while the other is located on the side wall of the housing and is collimated in order to illuminate two corners of the CCD. The door-mounted source will be used for initial calibration only; once the door is opened, it will not illuminate the CCD. The collimated source can easily be seen in two corners of each CCD. A small number of these X-rays scatter onto the entire CCD. In addition to the emission lines created by these sources, we can utilize a new feature of the XIS CCDs, charge injection capability, to assist with calibration. This allows an arbitrary amount of charge to be input to the pixels at the top row of the imaging region (exposure area), i.e. the far side from the frame-store region. The charge injection capability may be used to measure the CTI (charge transfer inefficiency) of each column, or even to reduce the CTI. How the charge injection capability will be used is still in progress as of this writing.

Pulse Height Determination, Residual Dark-current Distribution, and Hot Pixels

When a CCD pixel absorbs an X-ray photon, the X-ray is converted to an electric charge, which in turn produces a voltage at the analog output of the CCD. This voltage ("pulse-height") is proportional to the energy of the incident X-ray. In order to determine the true pulse-height corresponding to the input X-ray energy, it is necessary to subtracted the *Dark Levels* and correct possible *optical Light Leaks*.

Dark Levels are non-zero pixel pulse-heights caused by leakage currents in the CCD. In addition, optical and UV light may enter the sensor due to imperfect shielding ("light leak"), producing pulse heights that are nor related to X-rays. In the case of the *ASCA* SIS, these were handled via a signal mechanism: Dark Levels of 16×16 pixels were sampled and their (truncated) average was calculated for every exposure. Then the same average Dark Level was used to determine the pulse-height of each pixel in the sample. After the launch of *ASCA*, it was found that the Dark Levels of different pixels were actually different, and their distribution around the average did not necessarily follow a Gaussian. The non-Gaussian distribution evolved with time (referred to as Residual Dark-current Distribution or RDD), and resulted in a degradation of the energy resolution due to incorrect Dark Levels.

For the *Suzaku* XIS, Dark Levels and Light Leaks are calculated separately in normal mod. Dark Levels are defined for each pixel; those are expected to be constant for a given observation. The PPU calculates the Dark Levels in the Dark Initial mode (one of the special diagnostic modes of the XIS); those are stored in the Dark Level RAM. The average Dark Level is determined for each pixel, and if the dark level is higher

than the hot-pixel threshold, this pixel is labeled as a *hot pixel*. Dark Levels can be update by the Dark Update mode, and sent to the telemetry by the Dark Frame mode. Unlink the case of *ASCA*, Dark Levels are not determined for every exposure, but the same Dark Levels are used for many exposures unless they are initialized or updated. Analysis of the *ASCA* data showed that Dark Levels tend to change mostly during the SAA passage of the satellite. Dark Update mode may be employed several times a day after the SAA passage.

Hot pixels are pixels which always output over threshold pulse-heights even without input signals. Hot pixels are not usable for observation, and their output has to be disregarded during scientific analysis. The *ASCA* SIS did not identify hot pixels on-board, and all the hot pixel data were telemetered and removed during the data analysis procedure. The number of hot pixels increased with time, and eventually occupied significant parts of the telemetry. In the case of XIS, hot pixels are detected on-board by the Dark Initial/Update mode, and their positions and pulse-heights are stored in the Hot-pixel RAM and sent to the telemetry. Thus, hot pixels can be recognized on-board, and they are excluded from the event detection processes. It is also possible to specify the hot pixels manually. There are, however, some pixels which output over threshold pulse-heights intermittently. Such pixels are called flickering pixels. It is difficult to identify and remove the flickering pixels on board; they are inevitably output to the telemetry and need to be removed during the ground processing. Flickering pixels sometimes cluster around specific columns, which makes it relatively easy to identify.

The Light Leaks are calculated on board with the pulse height data after the subtraction of the Dark Levels. A truncated average is calculated for 64×64 pixels (this size may be changed in the future) in every exposure and its running average produces the Light Leak. Thus, the Light Leak is basically the same as the Dark Level in *ASCA* XIS. The Dark Levels and the Light Leaks are merged in the parallel-sum (P-sum) mode, so Dark Update mode is not available in P-Sum mode. The Dark Levels, which are defined for each pixel as the case of the normal mode, are update every exposure. It may be considered that the Light Leak is defined for each pixel in P-Sum mode.

On-board Event Analysis

The main purpose of the on-board processing of the CCD data is to reduce the total amount transmitted to ground. For this purpose, the PPU searches for a characteristic pattern of charge distribution (called an event) in the pre-processed (post-Dark Levels

and Light Leaks subtraction) frame data. When an X-ray photon is absorbed in a pixel the photoionized electrons can spread into at most four adjacent pixels. An event is recognized when a valid pulse-heights in the eight adjacent pixels (e.g. it is the peak value in the 3×3 pixel grid). The coordinated of the central pixel are considered the location of the event. Pulse-height data for the adjacent 5×5 square pixels are sent to the Event RAM as well as the pixel location.

The MPU reads the Event RAM and edits the data to the telemetry format. The amount of information sent to telemetry depends on the editing mode of the XIS. All the editing modes (in normal mode) are designed to send the pulse heights of at least 4 central pixels of an event to the telemetry, because the charge cloud produced by an X-ray photon can spread at most 4 pixels. Information of the surrounding pixels may or may not output to the telemetry depending on the editing mode. The 5×5 mode outputs the most detailed information to the telemetry, i.e. all 25 pulse-heights from the 5×5 pixels containing the event. The size of the telemetry data per event is reduced by a factor of 2 in 3×3 mode.

Photon pile-up

The XIS is essentially a position-sensitive integrating instrument, with the nominal interval between readouts of 8 s. If during the integration time one or more photons strike the same CCD pixel, or one of its immediate neighbors, these cannot be correctly detected as independent photons: this is the phenomenon of photon pile-up. Here, the modest angular resolution of the *Suzaku* XRT is an advantage: the central 3×3 pixel area receives 2% of the total counts of a point source, and ∼10% of the counts fall within ∼0.15 arcmin of the image center. We calculated the count rate at which 50% of the events within the central 3×3 pixels are piled-up (the pile-up fraction goes down as we move out of the image center; this fraction is $< 5\%$ for the 0.15 arcmin radius)– although we offer no formal justification for this particular limit, this is compatible with our *ASCA* SIS experience (i.e., at this level, the pile-up effects do not dominate the systematic uncertainties).

XIS background rate

All four XISs have low backgrounds, due to a combination of the *Suzaku* orbit and the instrument design. Below 1 keV, the high sensitivity and energy resolution of the XIS-S1 combined with this low background means that *Suzaku* is the superior instrument for observing soft sources with low surface brightness. At the same time, the large effective area at Fe K (comparable to the XMM pn) combined with this low

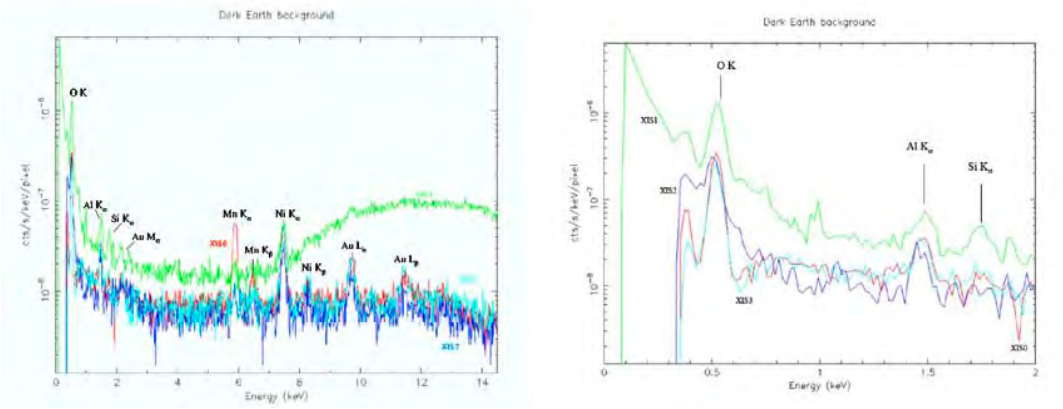

Figure 3.14 Left: The XIS background rate for each of the four XIS detectors, with prominent fluorescent lines marked. These spectra are based on ∼110–160 ksec of observations towards the dark Earth. These spectra dose not included Cosmic X-ray background (CXB). Right: The XIS background rate for each of the four XIS detectors, showing only energies between 0.1–2.0 keV. Below 0.3 keV the background rate for the FI chips cannot be determined due to their low effective area.

Table 3.3 Major XIS Background Emission Lines.

Line	Energy	XIS-S0	XIS-S1	XIS-S2	XIS-S3
	keV		10^{-9}c/s/pixel		
O-K	0.5249	18.5±0.5	$69.3^{+2.7}_{-2.6}$	$14.3^{+1.5}_{-1.3}$	$14.1^{+1.1}_{-1.2}$
Al-K	1.846	1.98±0.23	3.01±0.51	$1.50^{+0.31}_{-0.28}$	$1.57^{+0.25}_{-0.23}$
Si-K	2.307	$0.299^{+0.2080}_{-0.2074}$	2.21±0.45	0.0644(< 0.282)	$0.543^{+0.212}_{-0.213}$
Au-M	2.1229	0.581±0.234	$1.13^{+0.280}_{-0.291}$	$0.359^{+0.211}_{-0.212}$	$6.69^{+2.91}_{-2.90}$
Mn-Kα	5.898	$8.35^{+0.36}_{-0.34}$	0.648±0.289	$0.299^{+0.209}_{-0.2086}$	$0.394^{+0.181}_{-0.18}$
Mn-Kβ	6.490	$1.03^{+0.22}_{-0.216}$	0.294(<0.649)	0.00(<0.111)	$0.428^{+0.225}_{-0.226}$
Ni-Kα	7.470	7.20±0.31	6.24±0.53	$3.78^{+0.26}_{-0.25}$	$7.13^{+0.36}_{-0.37}$
Ni-Kβ	8.265	0.583±0.183	$1.15^{+0.5}_{-0.489}$	0.622±0.206	$0.983^{+0.247}_{-0.249}$
Au-Lα	9.671	$3.53^{+0.27}_{-0.28}$	$3.28^{+1.16}_{-0.99}$	$1.88^{+0.31}_{-0.28}$	$3.54^{+0.36}_{-0.35}$
Au-Lβ	11.514	$2.25^{+0.78}_{-0.59}$	2.91±1.29	$0.752^{+0.428}_{-0.340}$	$2.67^{+0.61}_{-0.53}$

background make *Suzaku* a powerful tool for investigation hot and/or high energy sources as well.

In the XIS, the background originates from the cosmic X-ray background (CXB) combined with charged particles (the non-X-ray background, or NXB). Currently, flickering pixels are a negligible component of the background. When observing the dark earth (i.e., the NXB), the background rate between 1–12 keV in is 0.11 $\mathrm{c\,s^{-1}}$ in the FI CCDs and 0.40 $\mathrm{c\,s^{-1}}$ in the BI CCD; see figure 3.14: left. Note that these are the fluxes after the grade selection is applied with only grade 0, 2, 3, 4 and 6 selected. There are also fluorescence features arising from the calibration source as well as material in the XIS and XRTs. The Mn lines are due to the scattered X-ray from the calibration sources. As shown in table 3.3 the Mn lines are almost negligible expect for XIS-S0. The O lines are mostly contamination from the day earth. The other lines are fluorescent lines from the material used for the sensor. Table 3.3 shows the current best estimated for the strength of these emission features, along with their 90% upper and lower limits.

The background rare on the FI chips (including all the grades) is normally less than 400 counts/frame (50 counts $\mathrm{s^{-1}}$) when no class discriminator is applied. On the BI chip, the rate is normally less than 150 counts/frame (18.75 counts $\mathrm{s^{-1}}$). The background rate on the FI chips is expected reduce significantly when the class discriminator is applied. But little change is anticipated for the BI chip. Since 5×5, 3×3, and 2×2 modes require on average 40, 20, and 10 bytes per event, the minimum telemetry required for any source is ∼58 kbits/s for 5×5 mode, ∼31 kbits/s for 3×3, and ∼17 kbit/s for 2×2 mode, if no class discriminator is used.

Out-of-time events

X-ray photons detected during the frame-store transfer do not correspond to the true image, but instead appear as a streak or blur in the readout direction. These events are called out-of-time events, and they are an intrinsic feature of CCD detectors. Similar streaks are seen from bright sources observed with *Chandra* and *XMM-Newton*. Out-of-time events produce a tail in the image, which can be an obstacle to detecting a low surface brightness feature in an image around a bright source. Thus the out-of-time events reduce the dynamic range of the detector. Since XIS spends 25 ms in the frame-store transfer, about 0.3% (= 0.025/8×100) of all events will be out-of-time events. However, because the orientation of the CCD chip is different among the sensors, one can in principle distinguish a true feature of low surface brightness and the artifact due to the out-of-time events by comparing the

images from two or more XISs.

Day Earth Contamination

When the XIS filed of view is close to the day earth (i.e., Sun lit Earth), fluorescent lines from the atmosphere contamination low-energy part of the XIS data, especially in the BI chip. Most prominent is the oxygen line, but the nitrogen line may be also noticed (figure 3.14). These lines are mostly removed when we apply the standard data screening criteria (XIS FOV is at least 20 degree away from the day earth) during the ground processing. However, small amount of contamination can remain. This contamination may be further reduced if we subtract appropriate background. This subtraction, however, may be imperfect. Thus, when neutral oxygen or nitrogen lines are detected in the XIS data, contamination from the day earth should be suspected.

Radiation Damage and On-board Calibration of the XIS

The performance of X-ray CCDs gradually degrades in the space environment due to the radiation damage. This generally causes an increase in the dark current and a decrease of the charge transfer efficiency (CTE). In the case of XIS, the increase of the dark current is expected to be small due to the low ($-90°$C) operating temperature of the CCD. However, a decrease in CTE is unavoidable. Thus, continuous calibration of CCD an orbit is essential to the good performance of the XIS. For this purpose, we use a radio isotope source and charge injection as explained below:
(i) Each XIS carries ^{55}Fe calibration sources near the two corners of the chip, which will be used to monitor the instrument gain.
(ii) Each XIS CCD is equipped with charge injection capability, which may be useful to measure and even suppress CTI

Nonetheless, it is difficult to predict based on existing data how well we can calibrate the long-term performance change of XIS on orbit.

On-ground event selection

Table 3.4 Parameters used in GTI selection of *Suzaku*

Parameter	Definition	Recommended value to use
SAA	Whether the satellite was in the SAA or not	eq.0
T_SAA	Time after the last SAA duration (s)	>255
ELV	Elevation angle from the Earth limb (degree)	>5
DYE_ELV	Elevation angle from the day Earth limb (degree)	>20
COR	Cut off rigidity of the cosmic ray (GeV/c/particle)	>8

Internal (non X-ray) background events can be efficiency removed using the pattern

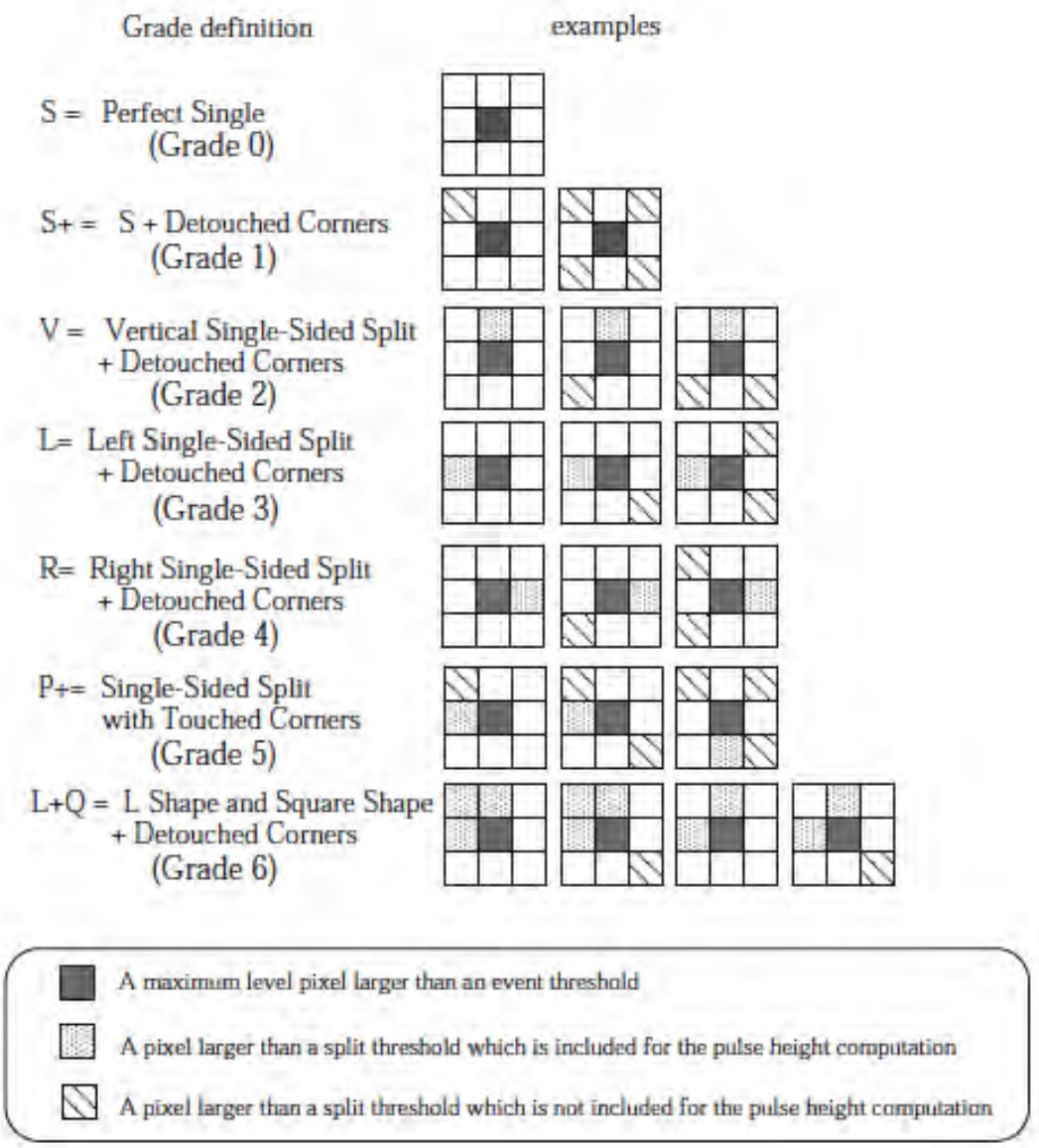

Figure 3.15 Definition of GRADE of CCD events.

on CCD pixels (GRADE), the position (STATUS) and time of an event. The definition of GRADE is shown in figure 3.15. Most of X-ray events take GRADE = 0, 2, 3, 4, or 6. On the other hand, most of the events of other GRADEs are dominated by non X-ray events, and should be excluded. STATUS parameter stores the pixels on the segment boundaries can be removed by selecting the events with STATUS<121072. The parameters used in good time interval (GTI) selection are shown in table 3.4. The signal to noise ratio can be improved with an appropriate GTI criteria, indicated in table 3.4.

Contamination correction

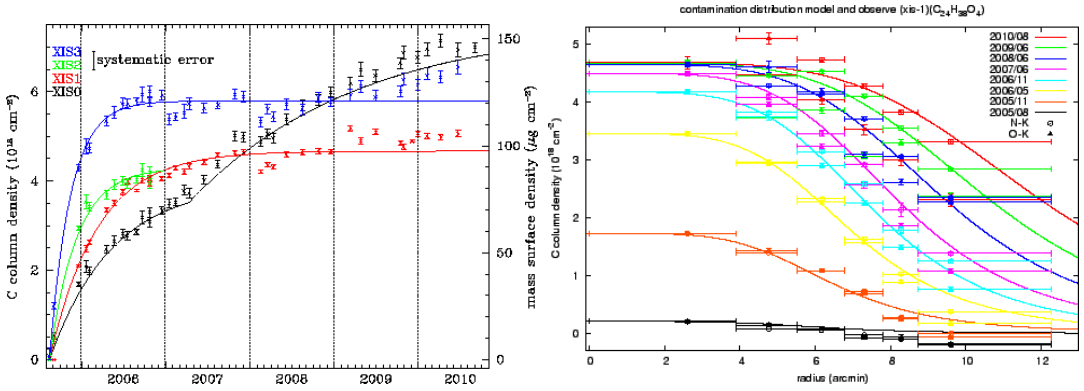

Figure 3.16 Left: The time history of the contamination of all four XIS detectors, measured at the center of the OBF. Right: The radial profile of the contamination of the BI chip.

The OBF has been gradually contaminated in time by out-gassing from the satellite. The contamination rate after the XIS door-open is unexpectedly high, and the rate is different from sensor to sensor. Moreover, the thickness of the contamination varies with position on the OBF.

The contamination has caused a significant reduction in low-energy response since launch. We therefore need to include additional, time-waring low energy absorption in the response function. This is given as a function of both the observation data after the XIS door-open, and of detector coordinates (specifying the position on the OBF). For this purpose, we measured the on-axis extra absorption by observing a NR 1E0102-72 and an isolated neutron star RX J1856.5-3754. At the time of writing, we have not conclusively determined the chemical composition for the contamination material(s). From the overall spectral shape in the low energy absorption for all the available X-ray sources and the best guess for the out-gassing source in *Suzaku*, we assume that the contamination contains predominantly C and O with the number ratio C/O = 6. Figure 3.16 shows the time histories of the contamination accumulated on the OBF. Empirically, the time dependence of the contamination thickness is assumed to follow the exponential form as; $N_{\rm c} = a - b \times \exp -day/c$, where $N_{\rm c}$ is the carbon column density in units of 10^{18} cm^{-6} (C/O = 6). To measure the off-axis absorption, we used diffuse X-ray from the bright Earth rim and the Cygnus Loop. The former emits characteristic K lines of $\rm N_I$ and $O_{\rm I}$ (neutral atoms) and the latter provides K lines from $\rm C_{VI}$, $\rm N_{VII}$, $\rm O_{VII}$ and $\rm C_{VIII}$ (He-like or H-like atoms). Since the former can be observed frequently, we trace the time history of on-axis absorption over successive one month periods after the XIS door-open (13 August, 2005). With the two reasonable assumptions that (1) the N:O line ratio is uniform over the filed of view and (2) the

contamination is azimuthal constant, we can derive the radial profiles of the column density. This radial profile is approximated by a function of $\frac{1}{[1+\{\frac{r}{a(t)}\}^{b(t)}]}$. The time dependent parameters, $a(t)$ and $b(t)$ are determined and update regularly.

3.2 *XMM-Newton* Satellite

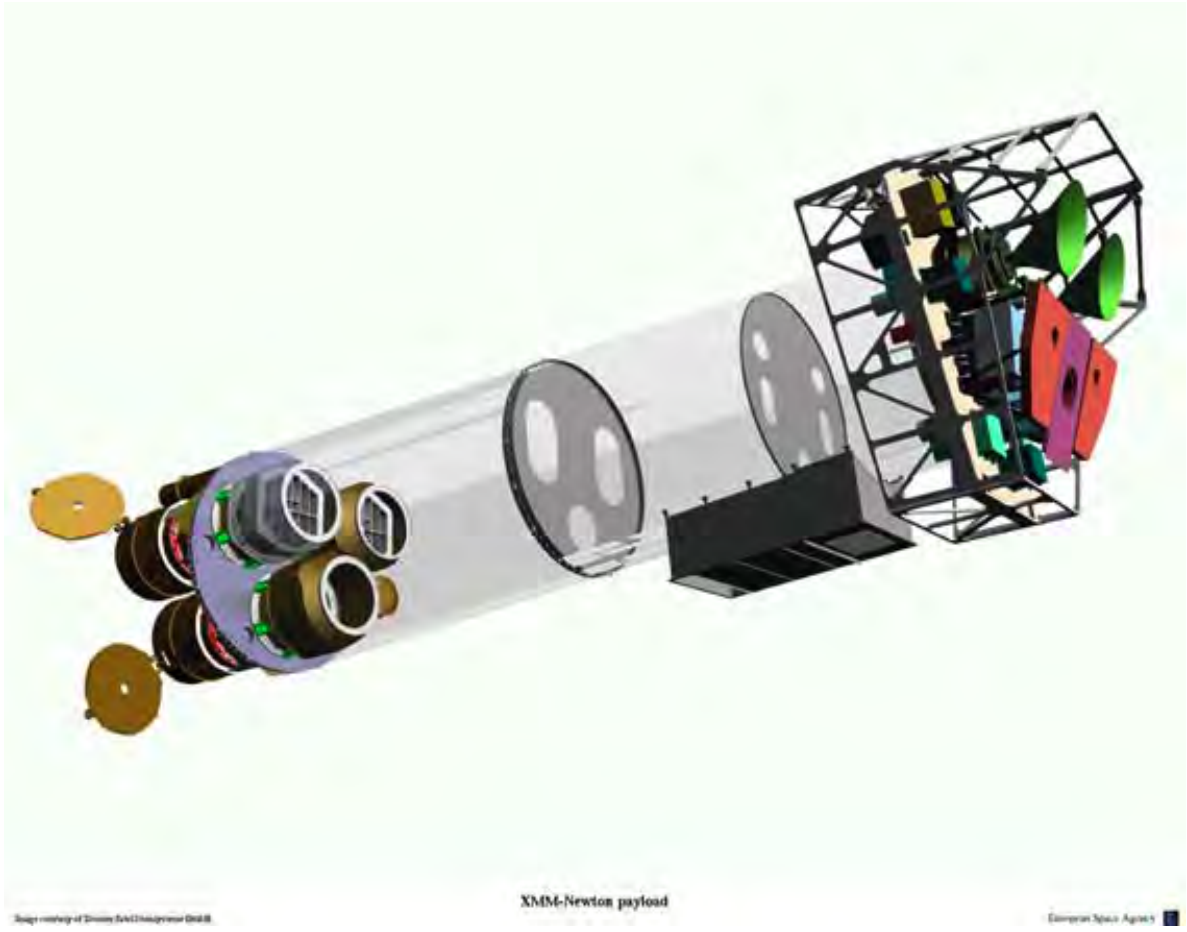

Figure 3.17 Sketch of the *XMM-Newton* payload. The mirror modules, two of which are equipped with Reflecting Grazing Arrays, are visible at the lower left. At the right end of the assembly, the focal X-ray instruments are shown: The EPIC MOS cameras with their radiators (black:green horns), the radiator of the EPIC pn camera (violet) and those of the (light blue) RGS detectors (in pink). The OM telescope is obscured by lower mirror module.

The ESA (European Space Agency) X-ray satellite *XMM-Newton* was launched on 10 December 1999 from Kourou (French Guiana), by the Ariane-V rocket (Jansen et al., 2001). It was placed into a highly eccentric orbit, with an apogee of about 115,000 km, a perigee of about 6,000 km, and an orbital inclination of 33°, which provides the best visibility in the southern celestial sky. Although the orbital period

48 hours, the exposure available for scientific data analysis is limited to 39 hours (140 ksec) per orbit. This is because observations are not carried out when the satellite altitude is less than 46,000 km, where the radiation background related to the Earth's magnetosphere is severe. *XMM-Newton* provides the following three type of science instrument; European Photon Imaging Camera (EPIC), Reflection Grating Spectrometer (RGS) and Optical Monitor (OM). The three EPIC cameras; the two different types of CCD camera, MOS and pn, and the two detectors of the RGS spectrometers reside in the focal planes of the X-ray telescopes, while the OM has its own telescope. A sketch of *XMM-Newton* payload is displayed in figure 3.17.

There are in total six science instruments on board *XMM-Newton*, which are operated simultaneously. The instruments can be operated independently and each in different modes of data acquisition.

In the following sections, we described the X-ray telescopes and EPIC cameras, because we mainly use these instruments in our study. We summarize the basic performance of the EPIC cameras in table 3.5.

Table 3.5 Basic performance of the EPIC detectors

	EPIC-MOS	EPIC-pn
Illumination method	Front illuminated	Back illuminated
Pixel size	40 μm	150 μm
	1.″1	4.″1
Field of View (FOV)	30′	30′
PSF (FWHM/HEM)	5″/14″	6″/15″
Spectral resolution	∼70 eV	∼80 eV
Timing resolution	1.5 ms	0.03 ms
Bandpass	0.15–12 keV	0.15–15 eV

3.2.1 X-ray Telescopes

Contamination correction

XMM-Newton's three XRTs are co-aligned with an accuracy of better than about 1 arcmin. Each of the three telescopes consists of 58 Wolter type-I mirrors, and the mirror grazing incidence angles range between 17 and 42 arcmin. The focal length is 7.5 m and the diameter of the largest mirrors is 70 cm. One telescope with the PN camera at the focal point has a light path as shown figure 3.18. The two others have

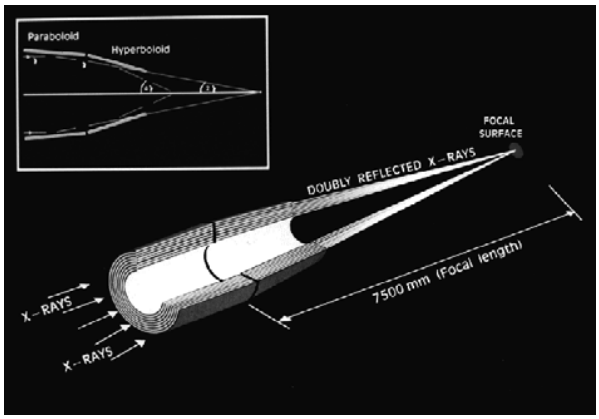

Figure 3.18 The light path in *XMM-Newton*'s XRT with the PN camera in focus.

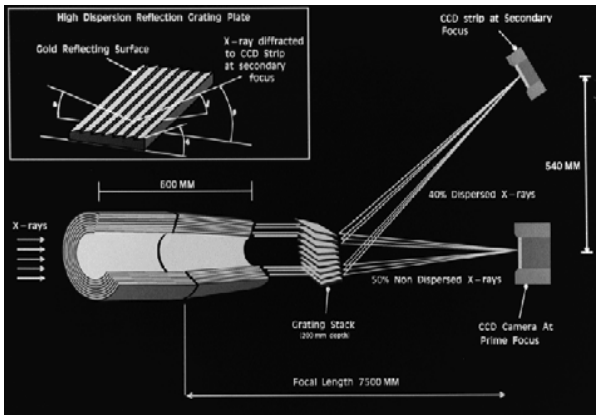

Figure 3.19 The light path in *XMM-Newton*'s XRT with the MOS camera and RGA.

grating assemblies in their light paths, diffracting part of the incoming radiation onto their secondary focus (see figure 3.19). About 44 % of the incoming light focused by the XRT is directed onto the MOS camera at the prime focus, while 40 % of the radiation is dispersed by a grating array onto a linear strip of CCDs. The remaining light is absorbed by the support structures of the RGAs.

Point-spread function (PSF) of XRTs

Table 3.6 The on-axis in orbit and on ground 1.5 keV HEW of the different XRT.

Instr.	pn	MOS1	MOS2
	orbit/ground	orbit/ground	orbit/ground
HEW [arcsec]	15.2/15.2	13.8/13.6	13.0/12.8

A point-spread function (PSF) determines the imaging quality of an XRT. Fig-

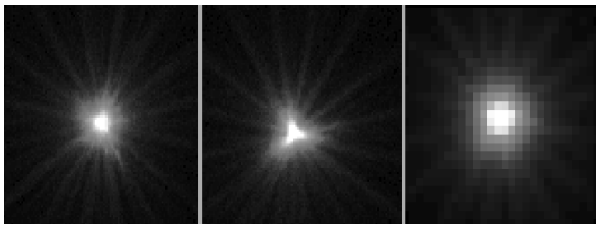

Figure 3.20 On-axis images of the MOS1, MOS2 and on XRTs (left to right). The images are 110 arcsec wide and a logarithmic scale has been used to visualize the wings of the point spread function.

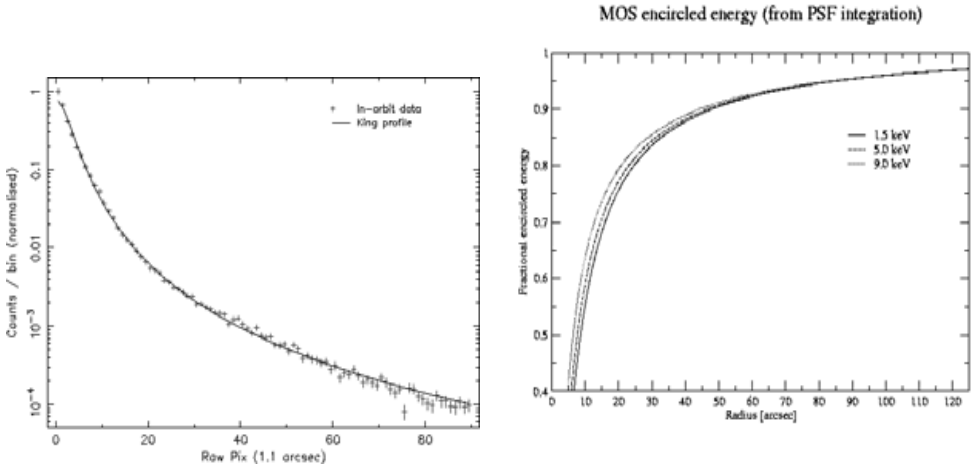

Figure 3.21 Left: Radial counts distribution for the on-axis PSF of the MOS1 XRT in the 0.75–2.25 keV energy range. The solid line indicates the best-fit King profile. Right: The encircled energy function as a function of angular radius (an-axis) at different energies. The curve are calculated assuming a fraction encircled energy of 100 % at a radial distance of 5 arcmin.

ure 3.20 shows the in orbit on-axis images obtained by each detector. The radial substructures are caused by the spiders holding the mirror shells. Figure 3.21 displays the azimuthally averaged profile of the PSF of one XRT together with the best-fit King profile, which has the form $A\left(\frac{1}{\left[\left\{1+\left(\frac{r}{r_c}\right)^2\right\}^{\alpha}\right]}\right)$, where r is the radial distance from the center of the PSF, r_c is the core radius and α is the slope of the King model. Figure 3.21 shows the encircled energy function (EEF) as a function of radius from the center of the PSF for several different energies. For on-axis source, high energy photons are reflected and focused predominantly by the inner shells of the XRTs. The inner shells apparently give better focus than the average of all shells, hence the EEF increase with increasing photon energy. A half energy width (HEW), which means the width including half of all the reflected photons, of the PSF can be derived from EEF. Table 3.6 lists the on-axis HEW of the different XRTs measured

in orbit and on ground.

The PSFs of the XRTs depend on the source off-axis angle. As the off-axis angle increases, the HEW of PSF becomes larger.

Effective Area (EA) of XRTs

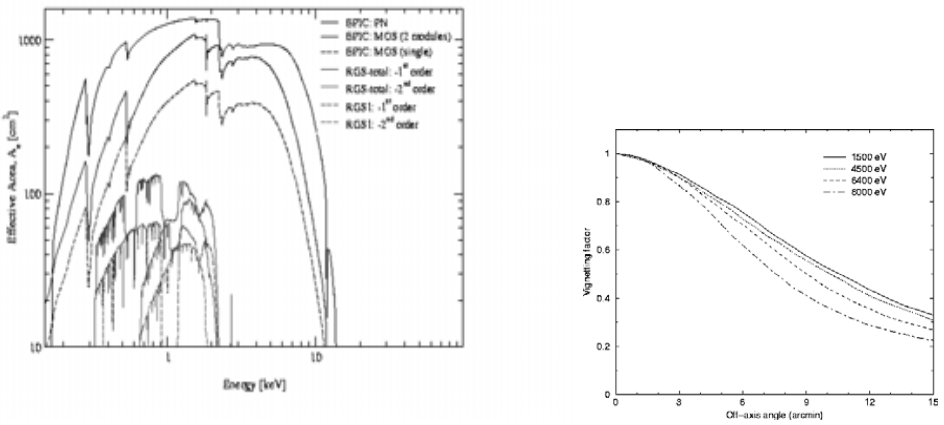

Figure 3.22 Left: The net effective area of all *XMM-Newton* XRT, combined with the response characteristics of the focal detectors. Right: Vignetting function as a function of off-axis angle at several different energies (based on simulations).

An effective area is an indicator of ability of collecting photons. *XMM-Newton* carries the XRT with the largest effective area of focusing telescope ever. The total mirror geometric effective area (EA) at 1.5 keV energy is about 1,550 cm^2 for each telescope, i.e., 4,650 cm^2 in total. Figure 3.22 shows the on-axis effective area of all *XMM-Newton* XRTs. The EAs of the two MOS cameras are lower than that of the pn, because only part of the incoming radiation falls onto these detectors, which are partially obscured by the RGAs (see figure 3.19). Not only the shape of the X-ray PSF, but also the effective area of the XRT is a function of off-axis angle within the field of view. Decreasing of photons reflected effectively in the XRT arises from an increasing off-axis angle. This effect is called vignetting. Figure 3.22 displays the vignetting function as a function of off-axis angle for several different energies. The vertical axis is normalized by the on-axis effective area.

Stray-light Rejection

X-ray stray light is produced by rays which are singly reflected by the mirror hyperbolas and which reach the sensitive area of the focal plain detectors. Thus, an

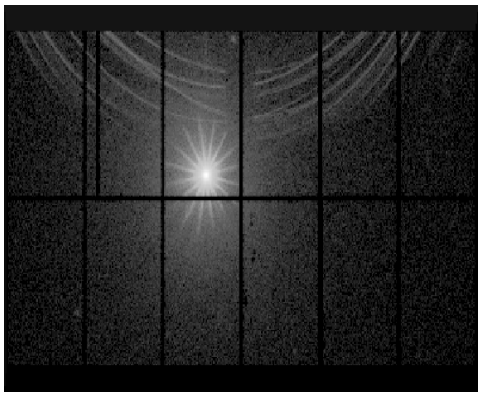

Figure 3.23 The effect of stray light in pn image of GRS 1758-258.

X-ray baffle was implemented to shadow those singly reflected rays. It consists of two sieve plates made of concentric annulus aperture stops located in front of the mirrors at 85 mm and 145 mm, respectively. The design is such that the entrance annular aperture of each mirror remains unobstructed for on-axis rays. The collecting area of stray light in the EPIC detector as a function of off-axis angle for a pint source is about 3 cm^2 for stray sources located between 20 arcmin and 1.4° from the optical axis. The ratio of the X-ray stray light collecting area to the on-axis effective area is smaller than 0.2 % at 1.5 keV for a point source located at off-axis angles of 0.4–1.4° and negligible at higher off-axis angles. Figure 3.23 displays the effect of stray light, which is obtained from the observation of GRS 1758-258 (a black hole candidate near the Galactic center). Some sharp arcs are caused by single mirror reflections of photons possibly from GX 5-1 which is located at off-axis angle of 40 arcmin to the north and outside the field of view.

3.2.2 European Photon Imaging Camera (EPIC)

Two of *XMM-Newton* X-ray telescopes are equipped with EPIC MOS (Metal Oxide Semi-conductor, Turner et al. (2001)) CCD arrays, the third carries a different CCD camera called EPIC pn (Strüder et al., 2001). The EPIC cameras offer the possibility to perform extremely sensitive imaging observations over a filed of view of 30 arcmin and the energy range from 0.15 to 15 keV, with moderate spectral ($\frac{E}{\Delta E}$ ∼20–50) and angular resolution (15 arcsec HEW). The detector layout and the baffled X-ray telescope FOV of both types of EPIC cameras are shown in figure 3.24. The PN chip array is slightly offset with respect to the optical axis of its X-ray telescope so that the nominal, on-axis observing position does not fall on the central chip boundary. This ensures that more than 90 % of the energy of an on-axis point source are collected on

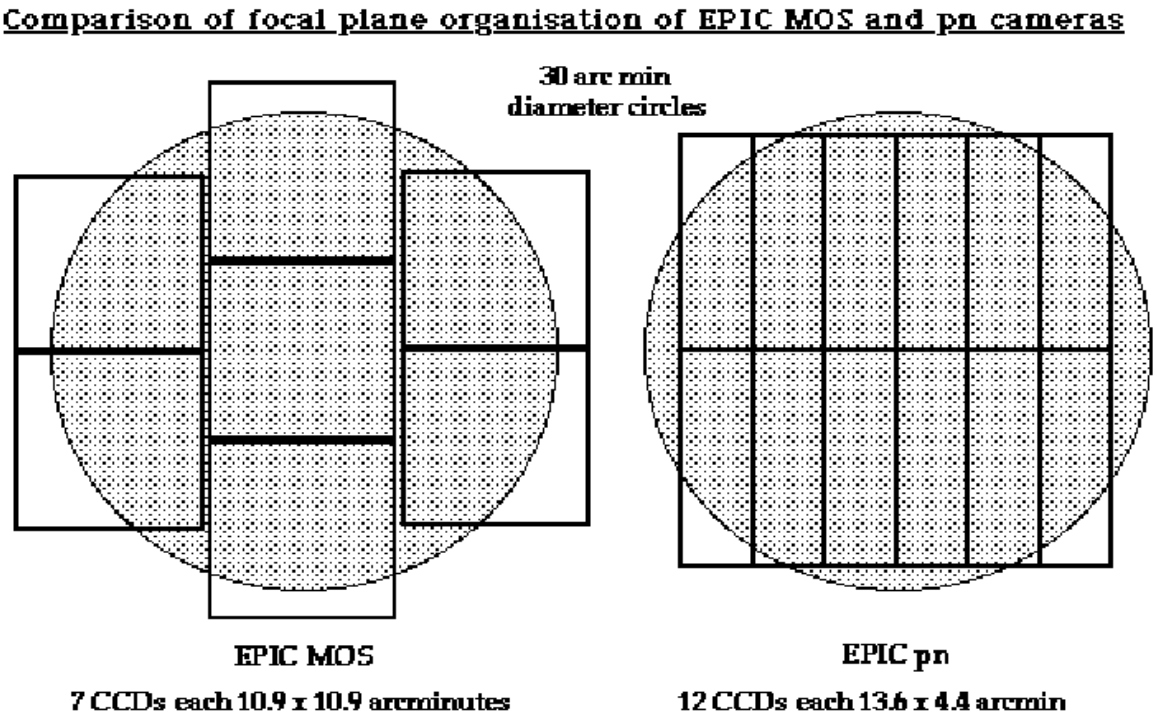

Figure 3.24 A rough sketch of the field of view of the two types of EPIC cameras (MOS, left; pn, right). The shaded circle depicts a 30 arcmin diameter area which is equivalent with the XRT field of view.

one pn CCD chip. Two EPIC MOS cameras are rotated by 90° with respect to each other. The dead spaces between the MOS chips are not gaps, but unusable areas due to detector edges (the MOS chip physically overlap each other, the center one being located slightly behind the ones in the outer ring). All EPIC cameras are operated in photon counting mode with a fixed, mode dependent frame read-out frequency.

Angular Resolution

The EPIC MOS and pn cameras have pixels with sizes of 40 and 150 μm, respectively. For the focal length of the X-ray telescopes (7.5 m), these pixel size corresponds to 1.1 arcsec and 4.1 arcsec on the sky. Since they are smaller than the HEW of XRT (15 arcsec), EPIC's angular resolution is basically determined by the PSF of the mirror modules.

Energy Resolution

The resolving power of EPIC cameras is determined by the intrinsic energy resolution of the individual pixels. Figure 3.25 shows the energy resolution (FWHM) of MOS and pn, respectively. The measured in-flight FWHM of the Al Kα (1.5 keV) and Mn Kα (5.9 keV), which are the on-board calibration lines, are also plotted in

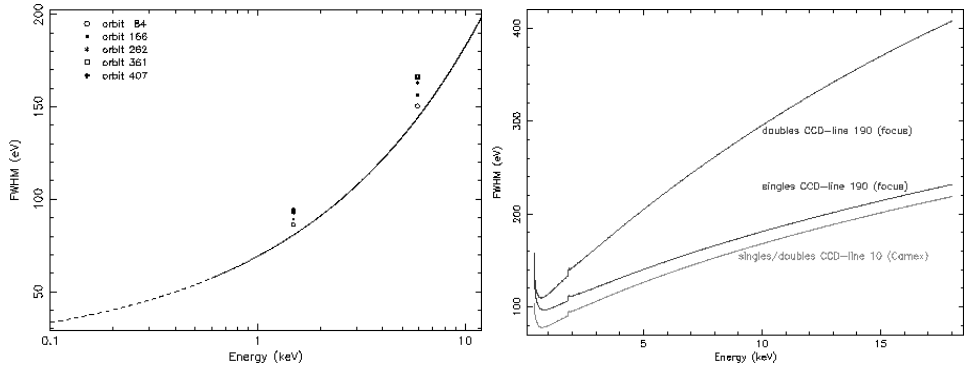

Figure 3.25 Left: The EPIC MOS energy resolution (FWHM) as a function of energy. The solid curve is a best-fit $E^{0.5}$ function to ground calibration data between 0.1–12.0 keV. Below around 0.6 keV (shown by the dotted region), surface charge loss effects distort the main photopeak significantly from a Gaussian from and, hence the effective energy resolution The measured in-flight FWHM of the Al Kα (1.487 keV) and Mn Kα (5.893 keV) lines are also plotted. Right: The EPIC pn energy resolution (FWHM) as a function of energy. Curve are given for single and double events (fill frame mode) at the focus position node.

figure 3.25. It is well known that the energy resolution of MOS cameras has been gradually decrease due to the CTI (charge transfer inefficiency) effect, which means the imperfect transfer of charge as it is transported through the CCD to the output amplifiers. The latest calibration status is found at *XMM-Newton* Science Operation Center [*1]. The accuracy of the energy determination is above 10 eV over the full energy range and for all modes expect for MOS timing mode.

Quantum Efficiencies

The quantum efficiency of both types of EPIC CCD chips as a function of photon energy is displayed in figure 3.26. These chips were calibrated using laboratory X-ray beams, synchrotron generated monochromatic X-ray beams, before launch, and celestial X-ray source measurements We can see the typical X-ray absorption fine structure (XAFS) behavior around the silicon K edge at 1.838 keV. Ground calibration measurements have shown that the quantum efficiency of MOS CCDs is uniform above 400 eV. Below this energy, spatial variations are seen as patches in the outer parts of the CCDs where the response is degraded. This inhomogeneity is currently not taken into account by the *XMM-Newton* science analysis system (SAS).

EPIC Filters

[*1] http://xmm.vilspa.esa.es/external/xmm_sw_cal/calib/documentation.shtml#EPIC

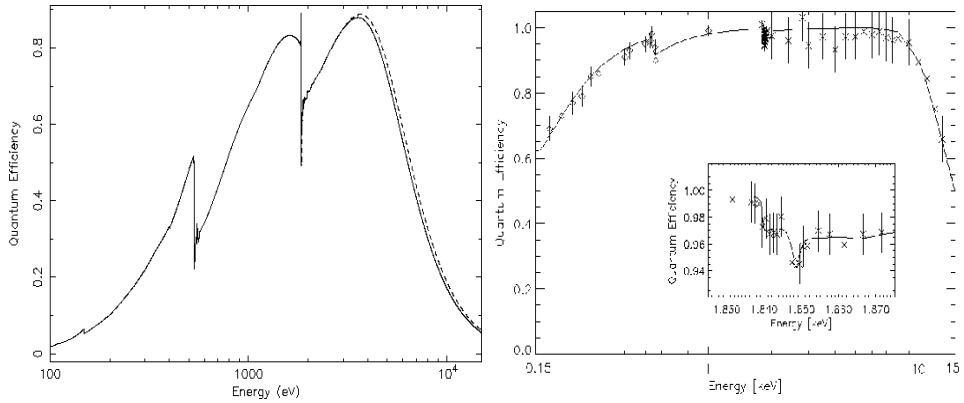

Figure 3.26 Left: Quantum efficiency of the EPIC MOS camera as a function of photon energy, Right: Quantum efficiency of the EPIC pn camera as a function of photon energy.

The EPIC CCDs are not only sensitive to X-ray photons, but also to IR, visible and UV light. Therefore, if an astronomical target has a high optical to X-ray flux ratio, there is a possibility that the X-ray signal becomes contaminated by those photons. To prevent such a contribution, each EPIC camera is equipped with a set of 3 separate aluminised optical blocking filters, named thick, medium and thin. The thick filter should be used for all point source targets up to $m_{\rm V}$ of 1–4 (MOS) or 0–3 (pn). The medium filter is about 10^3 less efficient than the thick filter, therefore, it is useful for preventing optical contamination from point sources as bright as $m_{\rm V}$ =8–10. The thin filter is about 10^5 less efficient than the thick filter, so the use of this filter will be limited to point sources with the optical magnitudes about 14 magnitudes fainter than the corresponding thick filter limitations.

Event Pattern

An absorbed sometimes deposits its energy over more than one pixels. This is called split event, and in this case the charges must be summed up over the relevant pixels. This process is automatically done by analysis software. The split pattern is classified in figure 3.27. The patterns 0–12 for MOS and 0–4 for pn are considered to be X-ray events, while the others are false events induced by charged particles. Because of its much larger pixel size than MOS, the charge split occurs less frequently in pn (Turner et al., 2001).

Any events which located at around an edge or bad pixel are flagged by negative value. These events have possibility that the energy of these events are not correct. If we make a condition that the events flag = 0, we remove the events which are located around the edge or bad pixel.

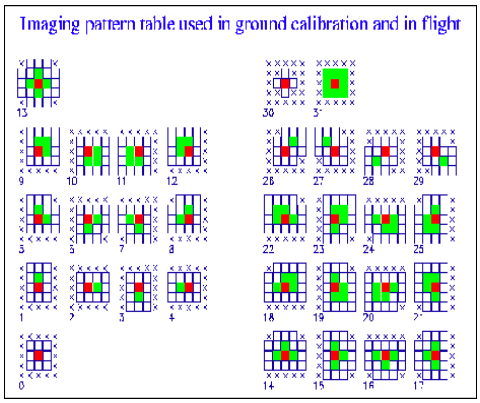

Figure 3.27 Event patterns recognized by the MOS (pn) detector. The red pixel is the centre pixel, its signal is above threshold and is the largest signal in the 3×3 inner matrix. The green pixels have signals above threshold. The white pixels have signal below threshold. The crosses indicates pixels no considered.

3.2.3 EPIC Background

The EPIC background can be divided into two parts: a cosmic X-ray background (CXB), and an instrumental background. The latter component may be further divided in to a detector noise component, which becomes important at low energy (i.e. below 200 eV) and a second component which is due to the particle interaction. This component is characterized by a flat spectrum and is particularly important at high energies (i.e. above a few keV).

The particle induced background can be divided into two components: an external 'flaring' component, characterized by strong and rapid variability, which is often totally absent and a second more stable internal component. The flaring component is currently attributed to soft protons, which are presumably funneled towards the detectors by the X-ray mirrors. The stable component is due to the interaction of high-energy particles with the structure surrounding the detectors and possibly the detector themselves. We summarize the all background component below.

- Cosmic X-ray Background
- Instrumental Background
  - Detector component (below 200 eV)
  - Particle component (above a few keV)
    - flaring component (attributed soft photons)
    - stable component (attributed high-energy particles)

In the following we describe some of the main properties of both components.

Temporal Properties

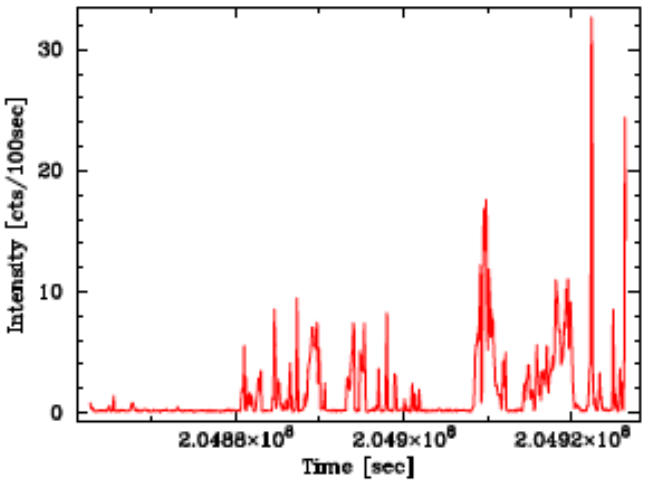

Figure 3.28 An example of light curve from a MOS1 observation badly affected by proton flares.

As shown in figure 3.28, the EPIC background count rate often exhibits sudden increases by as large as two orders of magnitudes, called 'flares'. Such phenomena are not observed in the *ASCA* SIS. This is mainly due to the difference in their orbits. *ASCA* had an almost circular orbit with an altitude of 520–620 km, while *XMM-Newton* take highly eccentric orbit, with apogees of ∼115,000 km and perigees of ∼6,000 km. Therefore, *XMM-Newton* fly mostly outside the Earth's magneto-sphere. Now it is known that the background flares are caused by soft protons with energies below 1 MeV, reflected and focused by the X-ray mirrors. The spectra of soft proton flares are variable and no clear correlation is found between intensity and spectral shape. The current understanding is that soft protons are most likely organized in clouds populating the Earth's magnetosphere. The number of such clouds encountered by *XMM-Newton* in its orbit depends upon many factors, such as the altitude of the satellite, its position with respect to the magneto-sphere, and the amount of solar activity.

The EPIC background events in quiescent (non-flaring) periods are produced mainly by the interaction of high energy particles with the structure surrounding the detectors, and the detectors themselves. This component varies only by a small fraction, and on relatively longer timescale. On a representative time scale of several tens ksec, the standard deviation of both PN and MOS count rate is about 8 % (Katayama et al. (2004); Pizzolato et al. (2001); Read & Ponman (2003)).

Spectral Properties

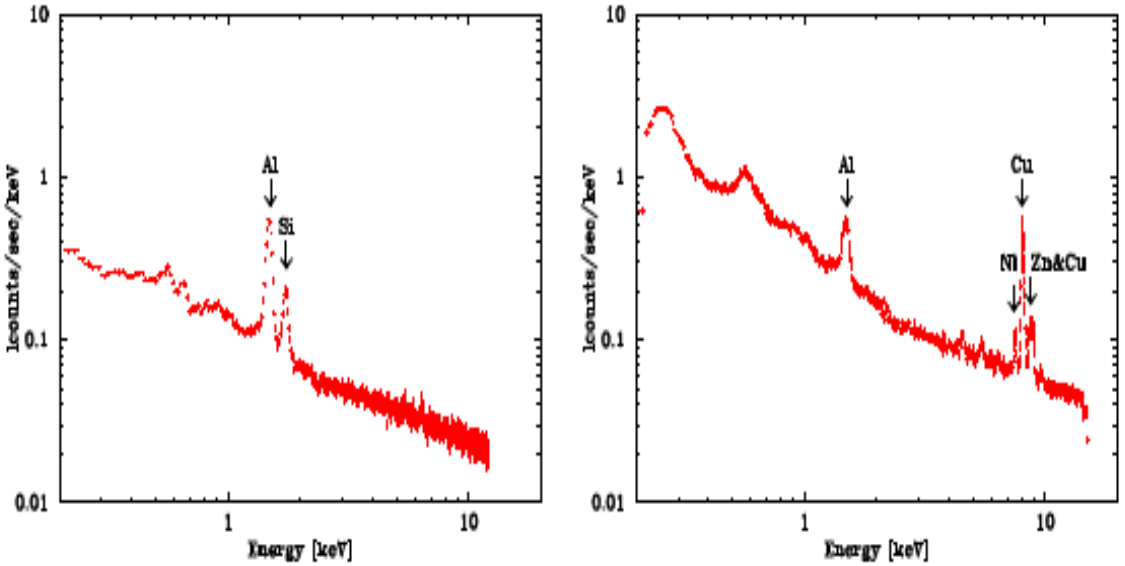

Figure 3.29 MOS1 (left) and pn (right) background spectrum from a blank sky region. In the left figure, the prominent features around 1.5 and 1.7 keV are Al K and Si K fluorescence lines, respectively. On the other hands, the prominent features, in right figure, are identified as Al-K (1.5 keV), Cr-K (5.5 keV), Ni-K, Cu-K, Zn-K (8.0 keV) and Mo-K (17.5 keV), respectively.

In figure 3.29, we show the MOS1 and pn spectra extracted from a blank sky region. These background spectra consists of non X-ray background (NXB) and cosmic X-ray background (CXB). The NXB is induced mainly by charged particles. The CXB is mainly dominates at lower energies by soft thermal emission around the solar system. The entire background spectra are dominated by the NXB at high energy regions, and the CXB becomes more important as the energy decreases. Their contributions are comparable at the energy of $\sim$ 1 keV.

Figure 3.29 shows several distinct fluorescence lines. In pn spectra, Al-K, Ni, Cu, and Zn-K complex lines are prominent, while Al and Si-K lines are outstanding in the MOS. These lines are emitted from surrounding materials such as electronic circuit boards for the signal readout, excited by high energy charges particles. Both the pn and MOS spectra rise below $\sim$0.5 keV, due to the detector noise which is more time variable than the continuum above 0.5 keV.

Spatial Properties

Because the CXB surface brightness is highly uniform, its brightness distribution on the focal plane obeys the effective area. Due to the vignetting effect, the CXB

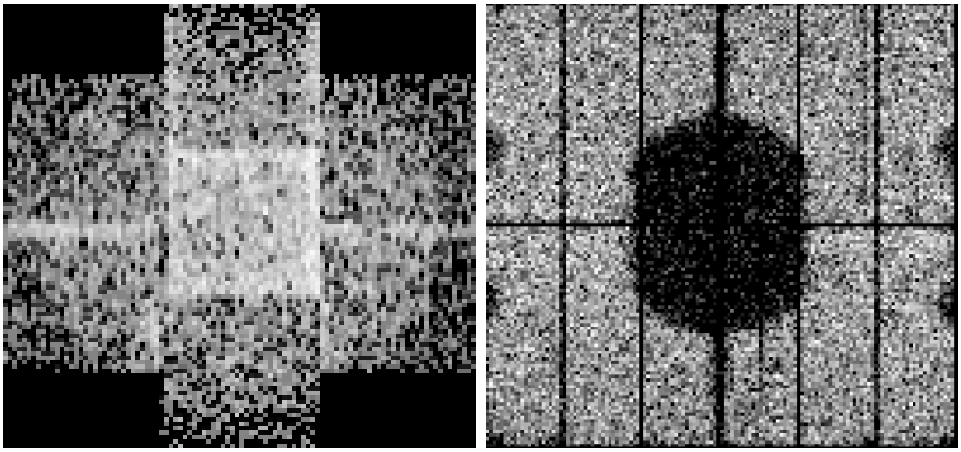

Figure 3.30 The MOS (left) and pn (right) background image. The MOS image in the energy band centered on Si-K fluorescent line region. As the same, the pn image in the Cu-K fluorescent line energy region.

brightness is highest at the detector center, and gradually decreases toward the periphery.

The distribution to Si-Kline in the MOS is concentrated along the edges of some CCDs. This is attributed to Si-K X-rays escaping from the back side of a neighboring CCD. The asymmetric distribution arises because the 7 CCD chips slightly overlap with one another when viewed from the telescope, although their 3-dimensinal positions are offset along the optical axis. This layout is intended to reduce the gaps between CCD chips.

Spatial distributions of emission lines are rather complicated. Figure 3.30 show some background images in limited energy bands. The emission in the Cu-K band is very weak at the center of pn (figure 3.30 right). Actually, the Cu-K line is insignificant in the spectrum extracted there. The Cu-K line image with the central hole agrees with the layout of electronics boards beneath the pn CCDs, indicating that the Cu-K photons come from them. The same mechanism produces semicircular dark regions at the right and reft side.

The continuum components of the NXB also have inhomogeneous distribution on the focal plane. The NXB image shows central excess brightness, by about 25 %. The shape is similar to the central hole seen in the Cu-K band image (figure 3.30), although in this case the brightness shows excess, not a deficit.

As is implied by these non-uniform distributions of carious components, the background spectrum strongly depends on the detector position. Therefore, when we use other observations as the background fields, we must extract the background spectrum from the same detector region as the analyzing target.

3.3 The *Chandra Satellite*

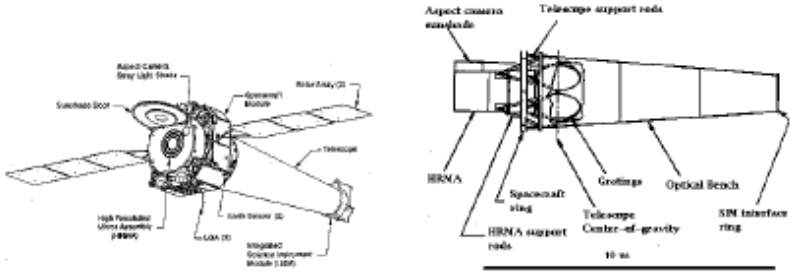

Figure 3.31 Left: The *Chandra* Observatory with certain subsystems labeled. LGA is an acronym for the Low Gain Antenna. Right: Major components of the telescope system. The grating assemblies are also shown.

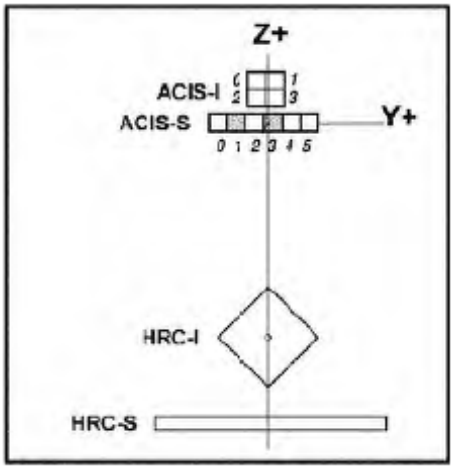

Figure 3.32 Arrangement of the ACIS and the HRC in the focal plane. The view is along the axis of the telescope from the direction of the mirrors. For reference, the two back-illuminated ACIS-S chips are shaded. Numbers indicate positions of chips I0–I3 and S0–S5. SIM motion can be used to place the aimpoint at any point on the vertical solid line.

Chandra is placed highly elliptical orbit with an apogee of 132,200 km and a perigee of 16,700 km in December 2008. This elliptical orbit allows for high observing efficiency of ∼160 ksec long continuous observation.

High Resolution Mirror Assembly (HRMA) consists of nested set of four paraboloid hyperboloid (Wolter-I) grazing-incidence X-ray mirror pairs, with the largest having a diameter of 1.2 m. The focal length is 10 m. In the optical path just behind the HRMA, two gratings spectrometers can be placed. High-Energy Transmission Graz-

ing (HETG) achieves resolving power ($\frac{E}{\Delta E}$) up to 1000 in the band between 0.4 keV and 10.0 keV when operated with ACIS-S. Low Energy Transmission Grating (LETG) provides the highest spectral resolution on *Chandra* at low (0.08–0.2 keV) energies when operated with HRC-S. The scientific payload on the focal plane consists of four distinct co-aligned instruments (figure 3.32). These are two CCD arrays (Advanced CCD Imaging Spectrometer, or ACIS), ACIS-I and ACIS-S. ACIS-I is comprised of 4 chips of CCDs and was designed for CCD imaging and spectrometry. ACIS-S is comprised of 6 CCDs and can be sued both for CCD imaging spectrometry and also for high-resolition spectroscopy in conjunction with the HETG grating. The second instruments are two microchannel plate (MCP) imaging detector (High Resolution Camera, or HRC), HRC-I and HRC-S. The HRC-I designed for wide-field imaging; and, HRC-S designed to serve as a readout for the LETG. We only use ACIS in the following analysis.

3.3.1 High Resolution Mirror Assembly (HRMA)

The *Chandra* X-ray telescope consists of 4 pairs of concentric thin-walled, grazing-incidence Wolter Type-I mirrors called the High Resolution Mirror Assembly (HRMA). The front mirror of each pair is a paraboloid ($P_{\rm n}$) and the back a hyperboloid ($H_{\rm n}$). The eight mirrors were fabricated from Zerodur glass, polished, and coated with iridium on a binding layer of chromium.

Physical Configuration

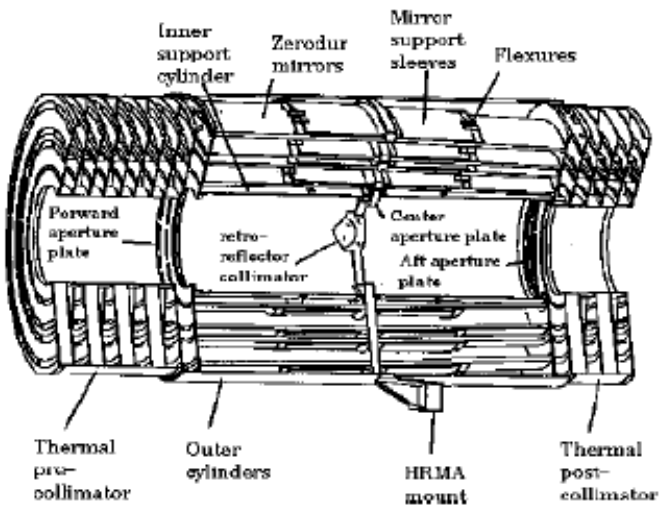

Figure 3.33 The four nested HRMA mirror pairs and associated structures.

Table 3.7 *Chandra* HRMA characteristics

Optics	Wolter Type-I
Mirror coating	Iridium (330 Å, nominal)
Focal length	10.070±0.003 m
PSF FWHM (with detector)	$< 0.''5$
Effective area:	800 cm^2 at 0.25 keV
	400 cm^2 at 5.0 keV
	100 cm^2 at 8.0 keV

The HRMA, as shown in figure 3.33, contains the nested mirrors, center, forward and after aperture plates, baffles, inner and outer cylinders, mounts, pre- and post-coliimators, fiducial light transfer components, mirror support sleeves, forward and after contamination covers, flux contamination monitors, and thermal control hardware. The pair diameters range from about 0.65 to 1.23 m. The distance from the center of the Central Aperture Plate (CAP) separating the paraboloid and hyperboloid mirrors to the HRMA focus is 10.0548 m, with each mirror pair varying slightly about this value. An annular on-axis beam enters each mirror pair, is reflected from paraboloids and hyperboloids and exits to converge to a focus. The HRMA characteristics are listed in table 3.7.

Effective Area

The unobstructed geometric aperture of the HRMA is 1145 cm^2. The obstruction of the HRMA aperture by supporting struts is less than 10 %. Since the reflectivity of the mirror optics depends on photon energy as well as grazing angle, the HRMA throughput varies with X-ray energy (figure 3.34).

Contamination Problem

There was an insignificant layer of molecular contamination on the mirrors. Subsequent in-flight gratings observations of blazers showed evidence for systematic effects near the Ir-M edges of the coating on the mirror and using these data and raytrace simulations, it was estimated that a 22 Å layer of hydrocarbon was present on the mirror optics.

Since the initial, ad-hoc, empirical correction of the HRMA model had already corrected for most of the effects of the molecular contamination, the addition of another 22 Å of contamination in the raytrace model post-launch was an over-correction.

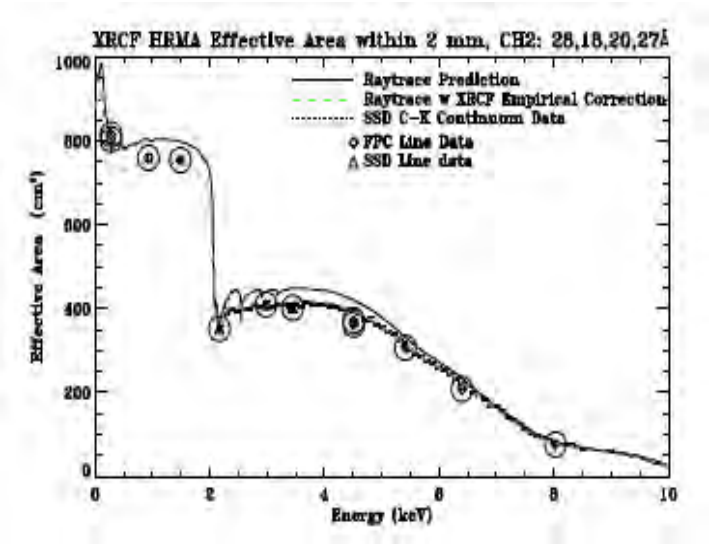

Figure 3.34 The HRMA effective area from the raytrace prediction as a function of energy. The raytrace includes the effects of molecular contamination of variable thickness on the mirrors. The dotted line (tp emphasize that these measurements were taken simultaneously) with error bars shows the data taken with a solid state detector (SSD) with a C-K continuum source. Data obtained from spectral line sources with a flow proportional counter (FPC) are shown as diamonds; obtained with a solid state detector (SSD) are shown as triangles. All the line measurements are circled for clarity. The dashed (green) line shows the absolute HRMA effective area with the X-Ray Calibration Facility (XRCF) empirical correction.

3.3.2 Advanced CCD Imaging Spectrometer (ACIS)

The advanced CCD Imaging Spectrometer (ACIS) offers the capability to simultaneously acquire high-resolution images and moderate resolution spectra. The instrument can also be used in conjunction with the High Energy Transmission Grating (HETG) or Low Energy Transmission Grating (LETG) to obtain higher resolution spectra. ACIS contains 10 planar, 1024×1024 pixel CCDs (figure 3.35); four arranged in a 2×2 array (ACIS-I) used for imaging, and six arranged in a 1×6 array (ACIS-S) used either for imaging or as a grating readout.

Energy Resolution

The ACIS FI CCDs originally approached the theoretical limit for the energy resolution at almost all energies, while the BI CCDs exhibited poorer resolution. The pre-launce energy resolution as a function of energy is shown in figure 3.36. The loss of energy resolution is due to increased charge transfer inefficiency (CTI) caused by

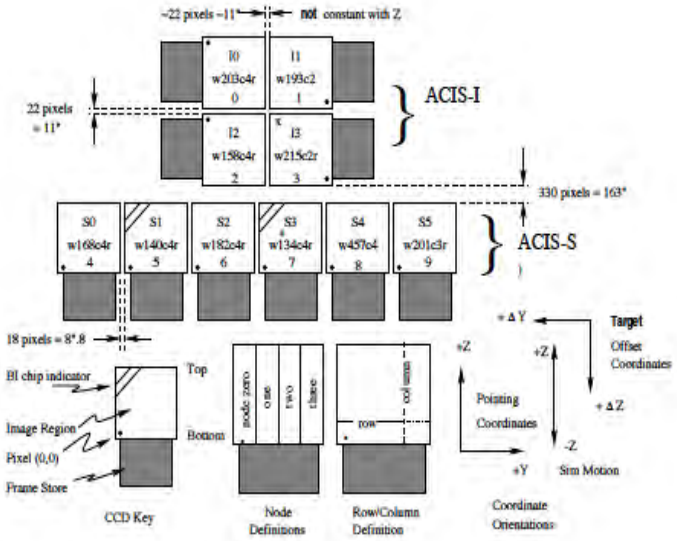

Figure 3.35 A schematic drawing of the ACIS focal plane; insight to the terminology is given in the lower left. Note the nominal aimpoints: on S3 (the '+') and on I3 (the 'x'). It is standard practice to add an offset to all observations on S3 to move the source away from the node 0–1 boundary. Note the differences in the orientation of the I and S chips, important when using Sub array. Note also the (Y, Z) coordinate system and the target offset convention as well as the SIM motion $(+/-Z)$. The view is along the optical axis, from the source toward the detectors, $(-X)$. The numerous ways to refer to a particular CCD are indicated: chip letter+number, chip serial number, and ACIS chip number. The node numbering scheme is illustrated lower center.

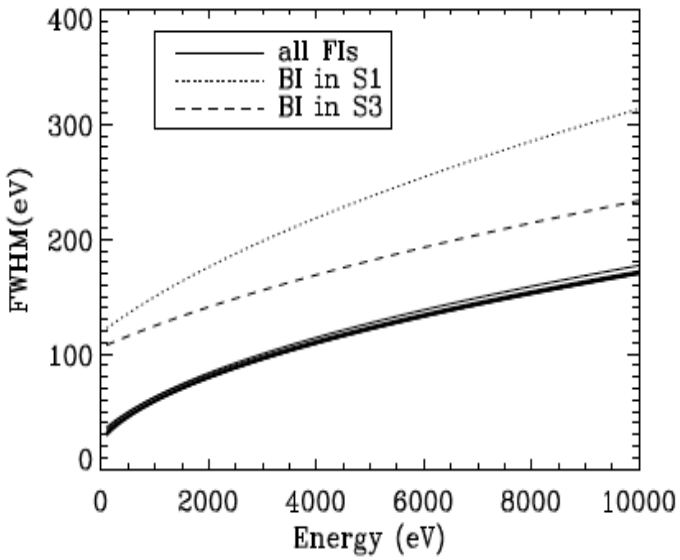

Figure 3.36 The ACIS pre-launch energy resolution as a function of energy.

low energy protons encountered during radiation belt passages and Rutherford scattering through the X-ray telescope into the focal plane. Subsequent to the discovery of the degradation, operational procedures were changed, ACIS is not left at the focal position during radiation belt passages. Since this procedure was initiated, no further degradation in performance has been encountered beyond with the proton-damage scenario - it is far more difficult for low-energy protons from the direction of the HRMA to deposit their energy in the buried channels of the BI devices, since the channels are near the gates and the fates face in the direction opposite to the HRMA. Thus the energy resolution for the two BI devices remains nearly at pre-launch values. The position-dependent energy resolution of the FI chips depends significantly on the ACIS operating temperature.

4 Observations & Data Reduction

4.1 Observations

NGC 253 is a nearby bright edge-on starburst galaxy and its large apparent diameter makes it a suitable target to study and understand not only the material circulation but also physical properties throughout the whole galaxy. Thus, this galaxy has been observed by multiband observatories, i.e., in radio, infrared, optical, ultraviolet and gamma-ray wavelength. Also in the X-ray region, many satellites directed their attention to NGC 253. In my paper, I focus on observations by the most recent three observatories among them, i.e., *Suzaku*, *XMM-Newton* and *Chandra* which help with extracting wide ranging physical properties utilizing individual advantages.

NGC 253 was observed by *Suzaku*, *XMM-Newton* and *Chandra* observatories in different periods and observational logs are summarized in Table 4.1. Because of its apparent size over 13 arcmin of the major axis of the optical disk, an offset observation just next to NGC 253 was carried out to evaluate a background level for *Suzaku*. Throughout this paper, we adopt a hydrogen column density by Galaxy of 1.5×10^{20} cm^{-2} (Kalberla et al., 2005) based on the LAB survey and we assume the solar abundance tabulated by Anders & Grevesse (1989). Throughout this paper, we adopt the distance to NGC 253 of 3.4 Mpc (Dalcanton et al., 2009) corresponding to 16 pc arcsec^{-1}.

Table 4.1 Observation log

Satellite	Seq. Num (ObsID)	Obs date	(α_{2000},δ_{2000}) [deg]	Exposure [ks]
Suzaku	805018010	2010/12/14 - 16	(11.9, -25.2)	101
Suzaku (OFFSET)	803004010	2008/12/29 - 30	(12.1, -25.0)	57
XMM-Newton	0125960101	2000/06/03	(11.9, -25.3)	35*, 31†
	0152020101	2003/06/19 - 20	(11.9, -25.3)	77, 54
Chandra	600093 (790)	1999/12/27	(11.8, -25.2)	44
	600114 (969)	2000/06/03	(11.9, -25.3)	14
	600305 (3931)	2010/09/19 - 20	(11.9, -25.3)	83 (67‡)

* Average exposure time of the MOS detectors.

† Exposure time of the PN detector.

‡ Exposure time after a background flare removal.

4.2 Data Reduction

4.2.1 *Suzaku*

For all *Suzaku* analysis, HEAsoft version 6.11 and XSPEC 12.7.0 were used. Data screenings for each region are shown in the following sections.

We analyzed only XIS-FI (XIS0 and XIS3) for the nuclear region, which has a lower background than XIS-BI (XIS1) at > 5 keV to avoid a systematic uncertainty associated with a simultaneous fitting of a different sensor. We note that the simultaneous fitting with XIS-BI and XIS-FI did not improve the fit. On the other hand, we use both XIS-FI and XIS-BI for the analysis of the superwind, disk and halo regions.

The redistribution matrix files (RMFs) and ancillary response files (ARFs) were created with the xisrmfgen and xissimarfgen ftools (Ishisaki et al., 2007), respectively. Since the bright region is within several tens of arcseconds in the nuclear region analysis, which is much smaller than the *Suzaku* point spread function (PSF; $1'.8$ as a half-power diameter), we assume the source to be a point-source when creating the arf files. For the analysis of the other regions, we assume the emission is uniform on the sky when we create the arf files.

The accumulation of dark Earth observations was used to estimate the non X-ray background (NXB) spectra, via the xisnxbgen ftool (Tawa et al., 2008). We subtracted NXB, the dominant background above 5 keV, but not the X-ray background, i.e., sum of the Galactic foreground emissions and cosmic X-ray background (CXB).

In some cases, a problem of flux discrepancy between FI and BI sensors are known, mainly due to a systematic error to estimate the effective area for diffuse sources. In this cases, we will introduce a flux scaling factor, as the same manner as Akamatsu et al. (2011) Results of spectral analysis of the offset region are shown in following chapters.

4.2.2 *XMM-Newton*

We utilized two *XMM* data sets (ObsID: 0125960101 in June, 2000 and 0152020101 in June, 2003). Since the PN detector has larger effective area than MOS detectors We focus on analysis by the PN detector with the effective exposure time of 31 and 54 ksec respectively after removal of flaring high background periods which is over 0.35 counts/sec above 10 keV. Light curves for the PN detectors during observations above 10 keV with a time binning factor of 100 sec are shown in Figure 4.1.

RMF and ARF files were made by the SAS rmfgen and arfgen tools. We extracted

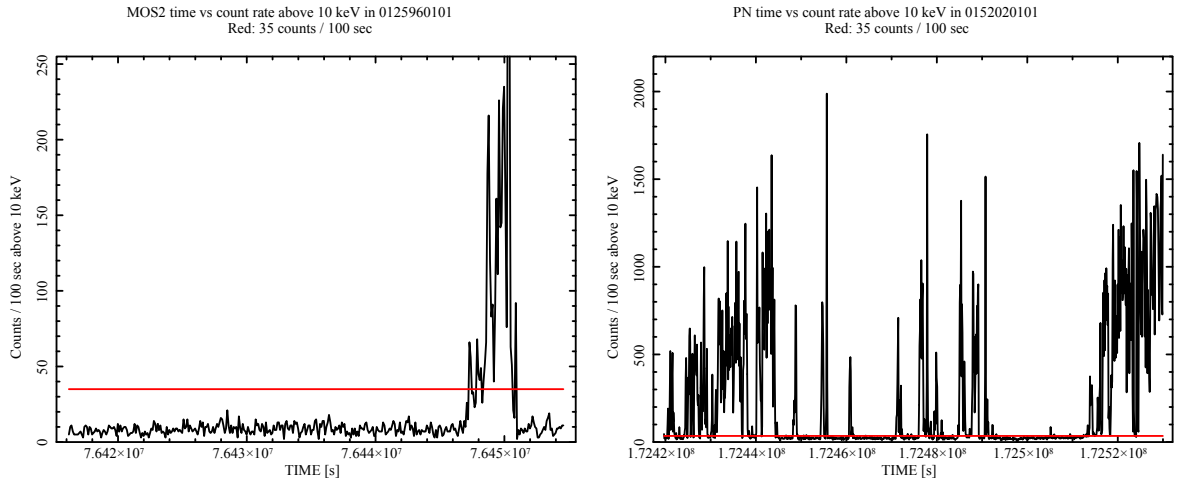

Figure 4.1 Light curves for EPIC PN detectors above 10 keV with a time binning factor of 100 sec in observations of 0125960101 (left) and 0152020101 (right), respectively. Red lines indicate the adopted threshold count rate of 0.35.

the background from a source-free region.

4.2.3 *Chandra*

The object was also observed by *Chandra* three times with the net exposure time of 14 ks (seq: 600114 in Dec, 1999), 44 ks (seq: 600093 in Dec, 1999) and 83 ks (seq: 600305 in Sep, 2003), respectively. We analyzed the level 2 *Chandra* ACIS-S event data. We used the merged data of three observations without any good-time-interval filtering because the background count rate is always <6.5 % of the source in 5.0–8.0 keV. RMF and ARF files were created using the CIAO mkacisrmf and mkwarf tools. We extracted the background from a source-free region.

5 Analysis & Results: Nuclear region of NGC 253

5.1 Introduction

As described in Chapter 2.2.2, X-ray emission from the central region of NGC 253 is known to be complex. *Chandra* suggested that the X-ray emission in the nuclear region is composed of a low-temperature thermal plasma and a heavily absorbed hard component that is expressed by a power law plus emission from a photoionized plasma emitting e.g., Fe IV–Fe XV and Fe XXV (Weaver et al., 2002). The hard component is interpreted as a buried AGN (Müller-Sánchez et al., 2010). The spectrum around the nuclear region could be modeled with three-temperature thin thermal plasmas including a high ($\sim$6 keV) temperature plasma responsible for the Fe XXV line (Pietsch et al., 2001).

In this Chapter, we report on the study of the nuclear region of NGC 253 using *Suzaku* and *Chandra*, with a particular focus on the Fe line complex. *Suzaku* has a good energy resolution to resolve the Fe line complex with a low background, while a sub-arcsecond spatial resolution of *Chandra* enables us to argue spatial distribution. We also show results by *XMM-Newton* as a complementary analysis.

5.2 Neutral, He-like and H-like Fe K lines with *Suzaku* and *XMM-Newton*

Spectra taken with *Suzaku* were extracted from a circular region with a radius of $2'.3$, indicated as R0 in Figure 5.1 left. The center of R0 corresponds to the peak position of the *Suzaku* 4.0–10.0 keV image. The size of R0 was optimized to realize the largest number of photons avoiding other disk-origin components and anomaly columns in the XIS0 detector below the nuclear region.

As shown in Figure 5.2 left, complex Fe K line structure was detected from the *Suzaku* spectrum as large residuals to a power-law continuum model. The continuum was determined in 5.0–8.0 keV but excluding 6.3–7.1 keV to avoid Fe K emission lines. The residuals can be resolved into three lines. We added Gaussian emission line

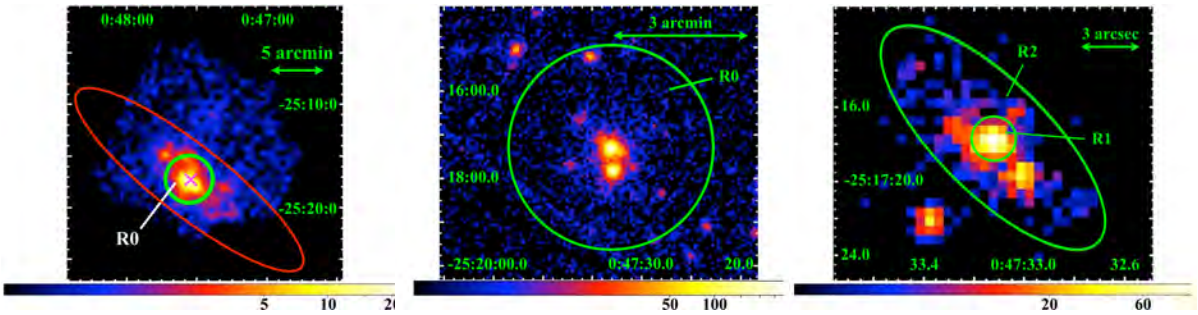

Figure 5.1 Left: *Suzaku* XIS3 image at 4.0-10.0 keV in the unit of cts s^{-1} (64 pixel)$^{-1}$ after removal of ^{55}Fe calibration sources located on the edge of the FOV. The field of view of *Suzaku* XIS is $18' \times 18'$. The red ellipse corresponds to an optical disk, while the green circle of radius of $2'.3$ and the magenta cross mark indicate the region R0 from which the spectrum was extracted and the center of the *Chanda* image (right in this figure). The image is smoothed with a kernel of $\sigma = 8''.3$. Middle: *XMM-Newton* PN image at 4.0–10.0 keV in the unit of cts s^{-1} (80 pixel)$^{-1}$ of ObsID: 0152020101. Right: close-up of *Chandra* ACIS image at the energy range between 4.0 and 10.0 keV in the unit of cts s^{-1} (1 pixel)$^{-1}$. For every image, the scale is logarithmic and vignetting is not corrected for.

models one by one to represent the three lines. The line width was fixed to 0. Fitting was significantly improved by each step. The best-fit line center, equivalent width (EW), and flux, along with their errors are summarized in Table 5.1. We considered only the error of line flux in estimating the error of EW. A systematic error in flux due to PSF modeling is bracketed by comparing two arfs: one for a point source and one for a uniformly extended source. The difference, ∼10 %, was smaller than the statistical error. *Suzaku* XIS achieved an energy scale accuracy better than 6 eV at 6 keV (Koyama et al., 2007), which means that the systematic error on the energy center is much smaller than the statistical error. The 3 σ acceptable range of the energy center of the lowest-energy line from our *Suzaku* observation is 6.29-6.43 keV, which includes Fe I to Fe XVI (House, 1969). The most natural explanation of the line is the neutral fluorescent line. We therefore interpreted the line as Fe I, although Weaver et al. (2002) indicated that it could be emission from low ionization-state ions (Fe IV-Fe XV).

We employed the Monte Carlo procedure described in Buote et al. (2009) to calculate a significance of these lines. In this process, we evaluated the reduction in the C-statistic (29.9 for Fe I and 11.4 for Fe XXVI) after adding a line with the energy center range restricted to 6.3–6.5 keV for the Fe I line and 6.87–7.07 keV for the Fe XXVI line. The two lines were added individually. We conducted 10000 Monte Carlo simulations without Fe I and Fe XXVI lines with the same exposure and binning as the observation. The fraction of simulation that improved the C-statistic by 29.9 and

11.4 are 0 and 1.1×10^{-3}, respectively. Therefore the significance of the detection of Fe I and Fe XXVI are >99.99 % and 99.89 %, respectively. This is the first clear detection of the Fe I and Fe XXVI lines in NGC 253.

We also extracted a spectrum from R0 using *XMM-Newton* as a complementary analysis and found the same complex Fe K lines with the PN detector as shown in Figure 5.2 middle. As is the case of *Suzaku* analysis, the same fitting procedure was performed. The best-fit line centers, fluxes and EWs are summarized in Table 5.1. Resultant intensities for three lines are consistent with those of *Suzaku*. Due to a higher background, we could not obtain a spectrum of the same quality from R0 using *Chandra*.

5.3 Spectral Analysis with Chandra

We utilized *Chandra*, characterized by a sub-arcsecond angular resolution, for determining the emission region of the Fe K lines. Although the emission in the *Suzaku* image (Figure 5.1 left) seems extended, this is due to the PSF of the mirror. From a *Chandra* image, we see that most of the emission above 4 keV is concentrated in $\sim 8''$ area (Figure 5.1 right). We divided the compact area into two regions, R1 and R2, as indicated in Figure 5.1 right to examine whether the emission lines are associated with the AGN. R1 is a circular region of a radius of $1''.2$ whose center is the peak of 4–10 keV surface brightness. The buried AGN is located in R1 (Müller-Sánchez et al., 2010). R2 is an ellipse with the major and minor axes of $8''$ and $3''$, respectively, but excluding R1. First, we extracted the spectrum from the whole (R1 + R2) region. The spectrum around the Fe K line complex is shown in Figure 5.2 right. We performed the same analysis as we did with the *Suzaku* and *XMM-Newton* data. The results are summarized in Table 5.1. Flux of Fe XXV and Fe XXVI are consistent among three observatories to within statistical errors, which suggests that these lines mostly originate from this compact region. On the other hand, the flux of Fe I observed with *Suzaku* and *XMM-Newton* is twice larger than those with *Chandra*. Hence, the neutral emission may be more extended than the ionized emission or variable. The smaller EWs of the *Suzaku* and *XMM-Newton* observations are because of a higher continuum due to the emission from the disk.

We also extracted the spectra from R1 and R2 to evaluate the contribution from the buried AGN. As is shown in Table 5.1, Fe E and Fe XXV lines are observed in the R2 region, while only an upper limit is obtained for Fe XXVI. The contribution to Fe I and Fe XXV is even larger in R2 than in R1. Thus the AGN is not the dominant

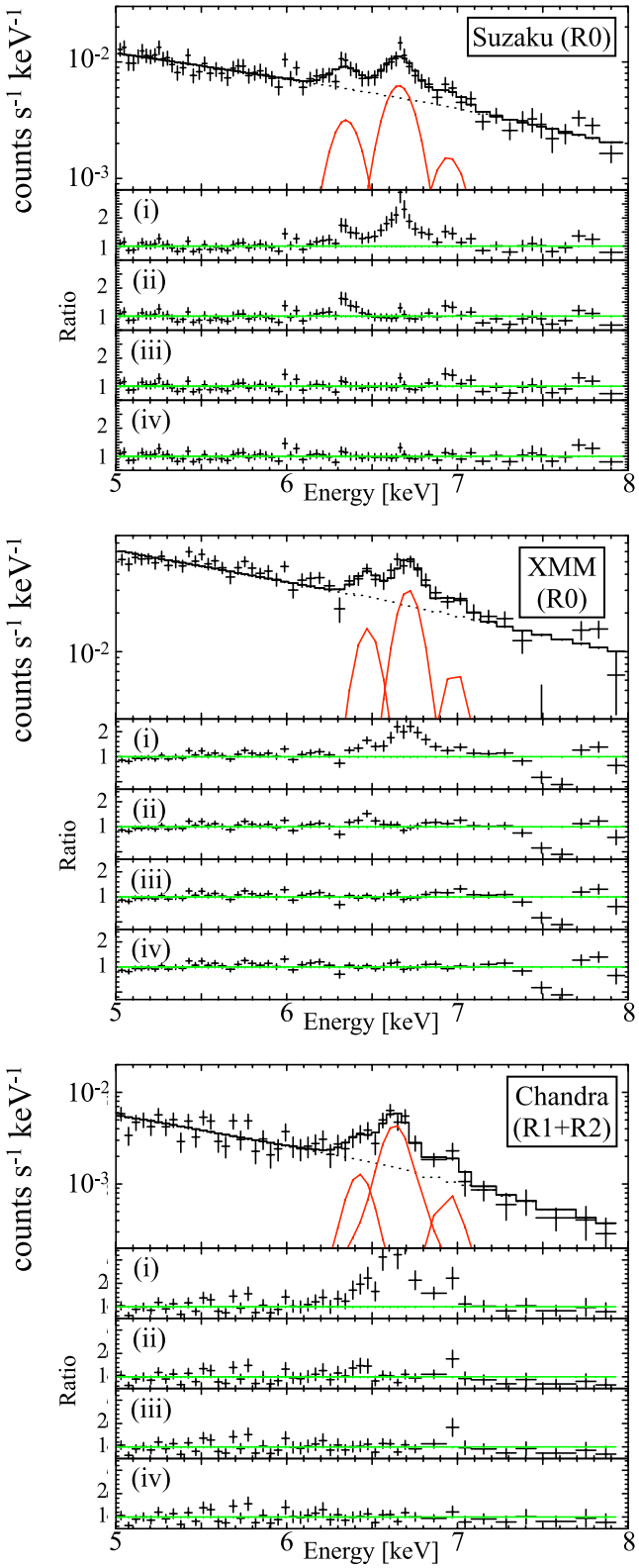

Figure 5.2 Spectra with residuals in 5.0–8.0 keV of *Suzaku* FI (top), *XMM* PN (middle) from R0 and *Chandra* ACIS (bottom) from (R1 + R2). The regions are defined in Figure 5.1. Each residual panel indicates that to the model of *power-law*, (ii) *power-law + gaussian*, (iii) *power-law + 2gaussian* and (iv) *power-law + 3gaussian*. The power-law continuum was determined by excluding 6.3–7.1 keV to avoid the contamination from Fe K emission lines.

Table 5.1 Energy and flux of complex Fe K lines.

Region		neutral Fe	Fe XXV	Fe XXVI
		Suzaku		
R0	Energy (keV) *	$6.36^{+0.04}_{-0.03}$	6.67±0.02	6.96±0.06
	Flux †	$3.8^{+1.2}_{-1.1}$	$8.4^{+1.4}_{-1.3}$	$2.3^{+1.2}_{-1.1}$
	EW (eV)	84^{+27}_{-24}	220^{+37}_{-34}	60^{+31}_{-29}
		XMM		
R0	Energy (keV) *	$6.49^{+0.03}_{-0.05}$	$6.72^{+0.02}_{-0.03}$	$6.99^{+0.08}_{-0.07}$
	Flux †	$3.8^{+1.0}_{-1.2}$	8.0±1.3	2.1±1.0
	EW (eV)	77^{+20}_{-24}	189±31	52±25
		Chandra		
R1	Energy (keV) *	6.40 (fix)	$6.66^{+0.04}_{-0.05}$	6.97 (fix)
	Flux †	<0.6	$2.1^{+1.1}_{-1.0}$	<1.0
	EW (eV)	<22	253^{+133}_{-120}	<83
R2	Energy (keV) *	6.45±0.09	$6.64^{+0.03}_{-0.02}$	6.97 (fix)
	Flux †	$1.2^{+1.0}_{-0.8}$	$4.8^{+1.3}_{-1.2}$	<1.1
	EW (eV)	86^{+72}_{-57}	617^{+167}_{-154}	<81
R1+R2	Energy (keV) *	$6.43^{+0.06}_{-0.07}$	$6.64^{+0.03}_{-0.02}$	$6.95^{+0.07}_{-0.06}$
	Flux †	$1.7^{+1.2}_{-1.0}$	$7.1^{+1.6}_{-1.4}$	$1.7^{+1.3}_{-1.1}$
	EW (eV)	75^{+53}_{-44}	427^{+96}_{-84}	82^{+63}_{-53}
P1	Energy (keV) *	$6.46^{+0.11}_{-0.14}$	$6.65^{+0.06}_{-0.05}$	6.97 (fix)
	Flux †	$0.8^{+0.9}_{-0.6}$	$1.9^{+0.8}_{-1.0}$	<0.8
	EW (eV)	176^{+198}_{-132}	662^{+279}_{-348}	<65

* Energy center at the rest frame.

† Photon flux in the unit of 10^{-6} photons s^{-1} cm^{-2}.

source of the two lines and these emission lines are distributed over the (R1+R2) regions.

5.3.1 Imaging analysis with Chandra

As described above, the observed Fe K complex is unlikely to be explained by the AGN alone. In this section, we conducted imaging analysis to demonstrate the spacial distribution of this structure. Figure 5.3 shows the *Chandra* narrow band line flux image for the Fe XXV (6.6–6.8 keV) line. Contribution of the continuum was subtracted from the images in the following way. We simply assumed that the continuum above 5 keV is expressed by a single power-law with the same photon index (2.0) in the whole region. The contribution from the continuum in 6.6–6.8 keV is calculated pixel by pixel using the photon index and the counts in 5.0–6.0 keV, where no line feature exists. The assumption of a uniform photon index is rather crude, because this can be applied for only the same spectrum properties. We also confirmed that the following results did not change with different assumption of photon indices (1.0 and 4.0). In R1, a heavily absorbed non thermal component from the buried AGN instead of a high temperature plasma dominates the hard band above 3 keV. Despite poor statistics, the map suggests that the line emission is not concentrated in R1, i.e., the location of the buried AGN. In contrast, two bright regions of Fe XXV line are found in P1 and P3 defined in Figure 5.3.

We also extracted the line flux image for the neutral Fe K line. However, the statistics are too poor to do any analysis. Hence we focus on the Fe XXV. To confirm the strong line emission in P1 and P3, we extracted spectra from four regions as indicated in Figure 5.3 denoted as P1, P2, P3 and P4. P1 and P4 are circles with a radius of $1''.5$ while P2 and P3 are rectangles of $1''.5 \times 3''$. P1 and P3 include the peak position while P2 and P4 are selected from darker areas for comparisons. P1 shows a strong line feature, while no line feature is found in P4. The resulting line fluxes in P1 are shown in Table 5.1. $\sim$50 % and 30 % of the observed total Fe I and Fe XXV lines are emitted only from P1 as shown in Figure 5.5 top. P2 and P3 have the same continuum flux but the resulting line flux of P3 for Fe XXV is twice larger than that of P2. Spectra and the best fit intensities in P1, P2, P3 and P4 are summarized in Figure 5.4 and Table 5.2.

The coordinates of peak pixel centers in P1 and P3 are $(\alpha_{2000},\ \delta_{2000}) = (00^{\rm h}47^{\rm m}33^{\rm s}.20,\ -25^\circ17'17''.2)$ and $(00^{\rm h}47^{\rm m}33^{\rm s}.01,\ -25^\circ17'19''.7)$, respectively. These are coincident with the peak positions of 1.3 mm continuum in the radio observation (Sakamoto et al., 2011) to within the position resolutions. The 99 %

uncertainty of absolute X-ray position by *Chandra* is 0″.8, while the beam size of the radio observation is 1″.1×1″.1. Thus, the Fe XXV line shows a clear association with the two peaks of molecular clouds. P1 is the most luminous in mid infrared and is suggested to be a super star cluster (Keto et al., 1999). P3 is the brightest in the 1.3 mm radio continuum and is featured by the water maser associated with star formation (e.g. Henkel et al., 2004).

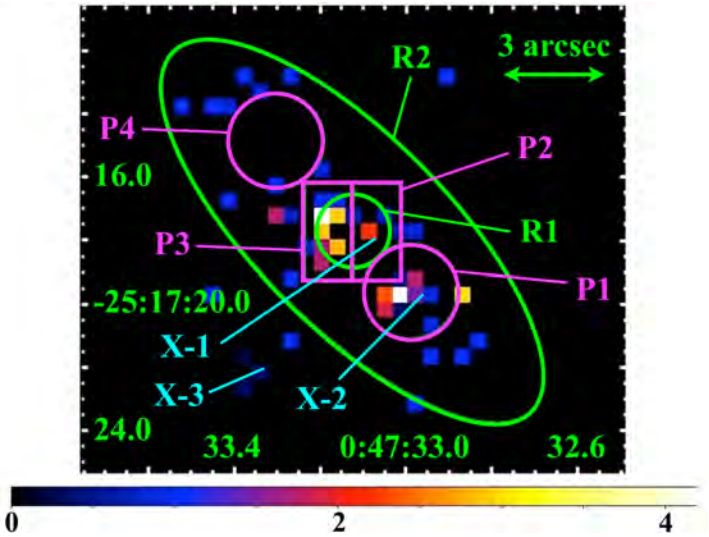

Figure 5.3 Narrow band line image by *Chandra* for the Fe XXV line (6.6–6.8 keV) after subtracting a continuum contribution. The color is in units of cts $(141\ \mathrm{ks})^{-1}$ $(1\ \mathrm{pixel})^{-1}$. The vignetting is not corrected for and the scale is linear. Green and magenta regions indicate regions from which spectra were extracted in this paper. Three X-ray sources (X-1, X-2, and X-3) found by Müller-Sánchez et al. (2010) are indicated by cyan.

Table 5.2 Fe XXV intensities in P1, P2, P3 and P4

Region	Line intensity of Fe XXV*
P1	$2.0^{+0.8}_{-0.7}$
P2	$0.7^{+0.9}_{-0.7}$
P3	$1.2^{+1.0}_{-0.8}$
P4	$0.2^{+0.4}_{-0.2}$

* Photon flux in the unit of 10^{-6} photons s^{-1} cm^{-2}.

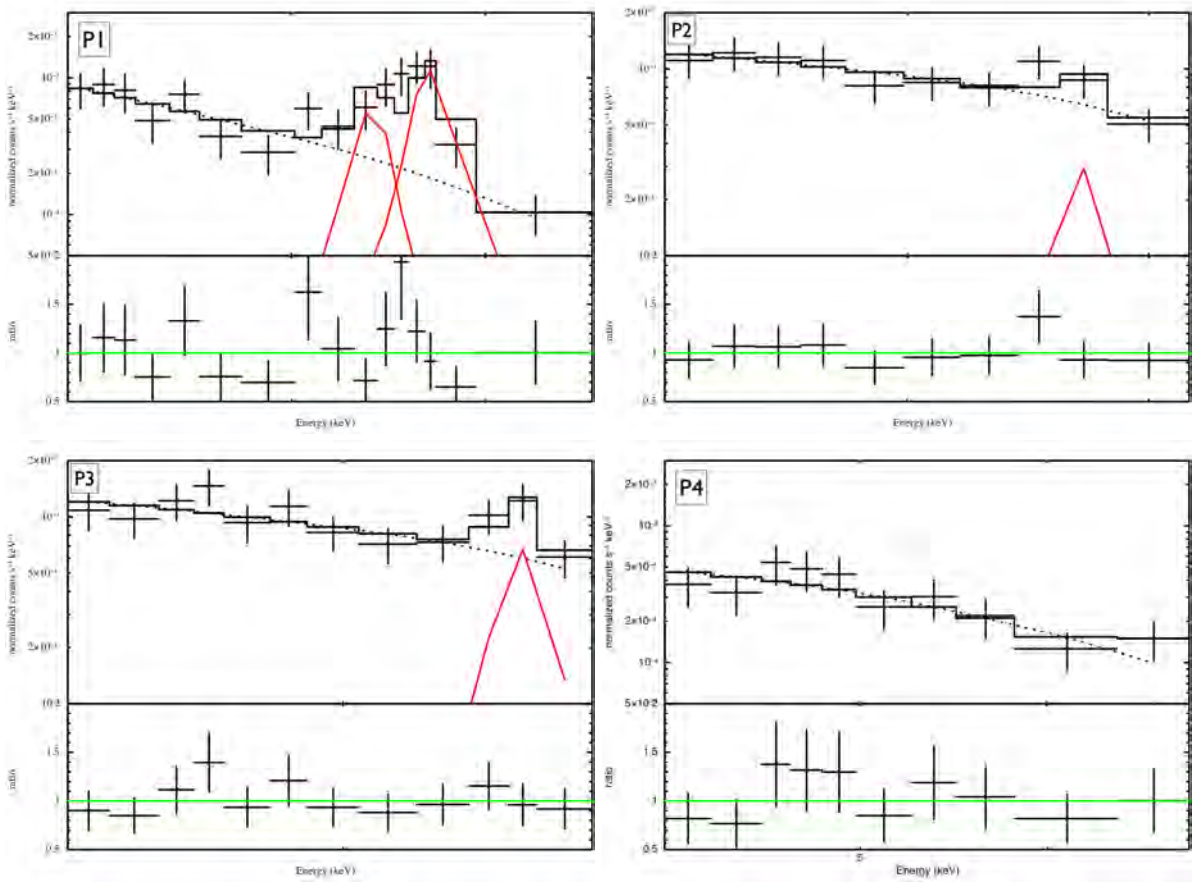

Figure 5.4 Spectra fitted with *power-law + gaussian* for P2, P3 and P4 and *power-law + 2gaussian* for P1 around Fe K line complex in 5.0–7.0 keV. Due to poor statistics, the energy band between 4.0 keV and 7.0 keV was adopted for P4. In a gaussian model, line energies are fixed to 6.4 keV and 6.7 keV for Fe I and Fe XXV emission lines, respectively.

5.3.2 Wide-band Spectrum fitting of the P1 region

To extract physical parameters in P1 we fitted the wide-band spectra (0.8–10 keV), where the highest line flux was confirmed. We adopted two-temperature thermal plasmas in collisionally ionization equilibrium plus a Gaussian whose centroid is 6.4 keV as the neutral Fe K line. One plasma represents highly-ionized Si and S emission lines and the other makes up for continuum above 3 keV and the Fe XXV emission line. The spectrum with the best-fit model is plotted in Figure 5.5. The abundance is fixed at solar values. The spectrum is well represented with the C statistic/$d.o.f$ of 132/95. The temperature of the higher-temperature plasma is $2.5^{+0.5}_{-0.3}$ keV. This plasma is responsible for the Fe XXV and Fe XXVI lines. The unabsorbed luminosity, thermal energy and total iron mass of the higher-temperature plasma are calculated to be $(8.6\pm1.4)\times10^{38}$ erg s^{-1} in 0.5–10.0 keV, $5.4^{+0.5}_{-0.6}\times10^{52}$ erg and 20 ± 2 M$_{\odot}$, respectively.

The unabsorbed luminosities of the Fe I and Fe XXV lines in P1 are also calculated to be $1.2^{+1.3}_{-0.9} \times 10^{37}$ and $2.7^{+1.2}_{-1.5} \times 10^{37}$ erg s^{-1}. Note that P1 has a radius of 24 pc and the spherical volume of 5.8×10^4 pc^3.

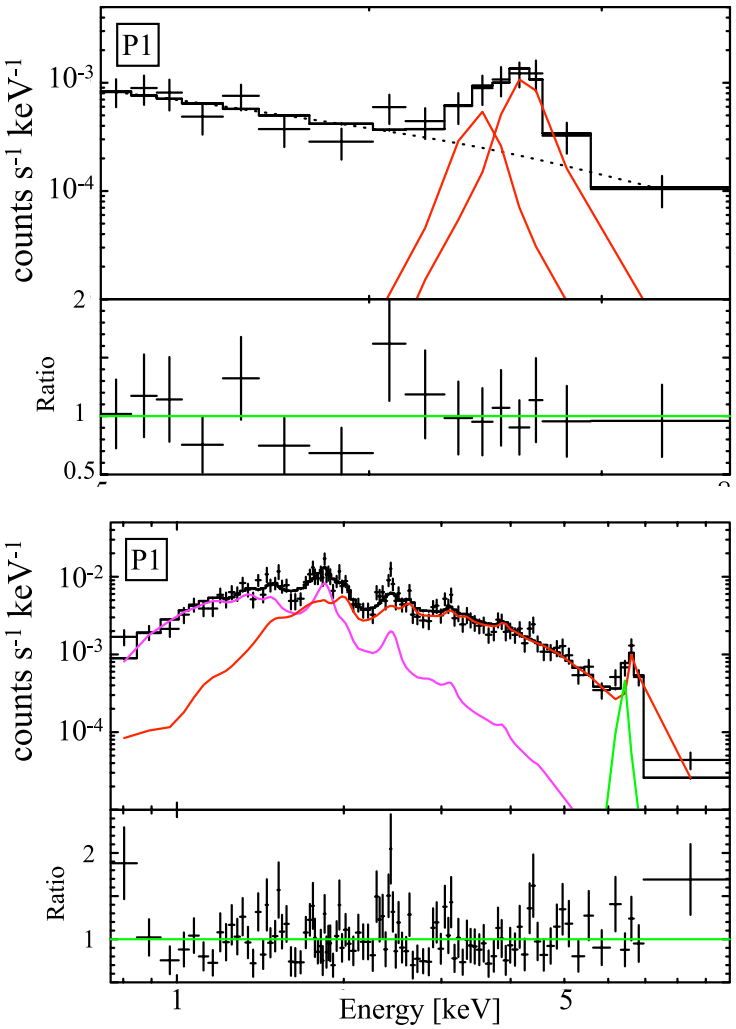

Figure 5.5 *Chandra* ACIS-S spectra of the P1 region. Top: spectrum in 5.0–8.0 keV fitted with *power-law + 2gaussian* corresponding to Fe I and Fe XXV lines (red). Bottom: wide-band spectrum in 0.8–10 keV. Magenta, red and green lines indicate thin thermal plasmas and the neutral Fe K line.

5.3.3 Wide-band Spectrum fitting and physical parameters of the whole nuclear region

To extract physical parameters of the whole nuclear region (R1 + R2), the wide-band spectrum fitting in 0.6–8.0 keV was performed. Three-temperature ISMs with each absorption column density, the heavily-absorbed non thermal plus neutral Fe K line was adopted. The second term corresponds to the buried AGN component

reported in Müller-Sánchez et al. (2010). In the spectrum fitting of (R1 + R2), parameters on the buried AGN were fixed to the best fit values determined in spectrum analysis of R1 where the buried AGN was expected to be. We confirmed that the best fit parameters on the buried AGN were consistent with the obtained by Müller-Sánchez et al. (2010). In a gaussian model, the line energy was fixed to 6.4 keV. Resultant spectrum and physical parameters are shown and summarized in Figure 5.6 and Table 5.3.

From the fitting, the temperature kT, flux and $\int f n_H^2 dV$ can be determined, where f is a volume filling factor. By assuming a distance, the luminosity L is derived. To calculate a hydrogen density, we assumed a spheroidal volume of $9.7{\times}10^{61}$ cm^3 with two axes of $8''$ and $3''$ corresponding to (R1 + R2). The pressure is calculated as $P = n_H kT$ and the thermal energy as $E_{th} = 3nkTV/2$. We also calculated the radiative cooling time $t_{cool} = 3kT/\Lambda n_e$. Those values are also shown in Table 5.3.

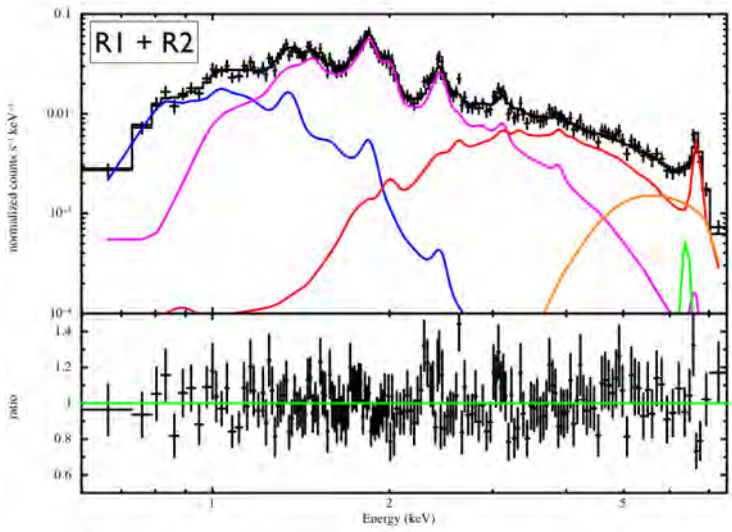

Figure 5.6 *Chandra* ACIS-S Wide-band spectrum in 0.6–8 keV of the (R1 + R2) region fitted with $phabs_{\rm Galaxy}\times(phabs_{\rm NGC253}\times apec_{\rm ISM:1T}$ + $phabs_{\rm NGC253}\times apec_{\rm ISM:2T}$ + $phabs_{\rm NGC253}\times apec_{\rm ISM:3T}$ + $phabs_{\rm NGC253}\times$*power-law*) + *gaussian*. The last two terms correspond to the buried AGN (orange) and the neutral Fe emission (green) line fixing the line energy to 6.4 keV. Parameters on the buried AGN are fixed to the best fit values determined in spectral analysis of R1.

Table 5.3 Physical parameters for the three-temperature plasma in the nuclear region

Parameters \ Plasma	ISM1	ISM2	ISM3
kT [keV]	$0.31^{+0.10}_{-0.06}$	1.0 ± 0.1	$3.0^{+1.3}_{-0.9}$
L^* [10^{39} erg s^{-1}]	$3.0^{+3.6}_{-1.9}$	$7.9^{+1.3}_{-1.0}$	$3.1^{+2.8}_{-0.8}$
n_H [$f^{-1/2}$ cm^{-3}]	$1.2^{+1.4}_{-1.0}$	$1.6^{+0.7}_{-0.6}$	$1.3^{+1.3}_{-0.8}$
P/k [$f^{-1/2}$ 10^6 K cm^{-3}]	$4.3^{+8.1}_{-3.7}$	19^{+11}_{-8}	45^{+84}_{-33}
E_{th}† [$f^{1/2}$ 10^{52} erg]	$8.1^{+9.1}_{-4.4}$	37^{+5}_{-4}	90^{+95}_{-41}
t_{cool}‡ [$f^{1/2}$ Myr]	$0.72^{+5.06}_{-0.46}$	$2.3^{+1.7}_{-0.8}$	$11.7^{+31.9}_{-7.6}$

* Unabsorbed luminosity in 0.5–10.0 keV assuming the distance to 3.4 [Mpc].

† Thermal energy.

‡ Radiative cooling time using 3 kT / Λn_e.

6 Analysis & Results: Superwind/Disk regions of NGC 253

6.1 Introduction

As the next analysis of the nuclear region, we focused on so-called the "superwind" region just outside the nuclear region but very inner side in the disk region because the direct wind from the nuclear region is considered to be flowed into this region. Then, according to a standard scenario of the outflow, the superwind flow is expected to come through the disk region into the halo continuously. Thus, in order to understand the galactic-scale starburst-driven outflow, these regions are worthy to be analyzed. In this section, we especially concentrate on chemical abundances to extract chemical compositions as a new proof to pursue the origin of the outflow itself.

6.2 Superwind region in the disk with *XMM-Newton*

According to a *Chandra* image, the superwind region seems to be connected to the nuclear region continuously. The size of the superwind region in an X-ray band is on the order of $1' \times 1'$. Thus, we selected *XMM-Newton* which has an advantage to extract metal abundances including oxygen from the low temperature plasma around 0.2 keV compared to *Chandra*. Among instruments on board *XMM-Newton*, MOS detectors were chosen due to its higher energy resolution. The extracted region is shown in Figure 6.1. This region is located $\sim 35''$ away from the nuclear region to avoid a contamination. Considering the EEF profile of the MOS detector, only <15 % emission from the bright nuclear region can reach the superwind region. Indeed, an observed flux of the superwind region in 0.5–1.0 keV which is expected to be dominated by ISM emissions is an order of magnitude larger than the observed in the nuclear region, which suggests that almost all observed emissions come from the superwind region. We also confirmed that no Fe K line feature as the nuclear-specific emission was found in the spectrum of the superwind region. We extracted a background region from the same CCD chip considering a spatial dependence of the

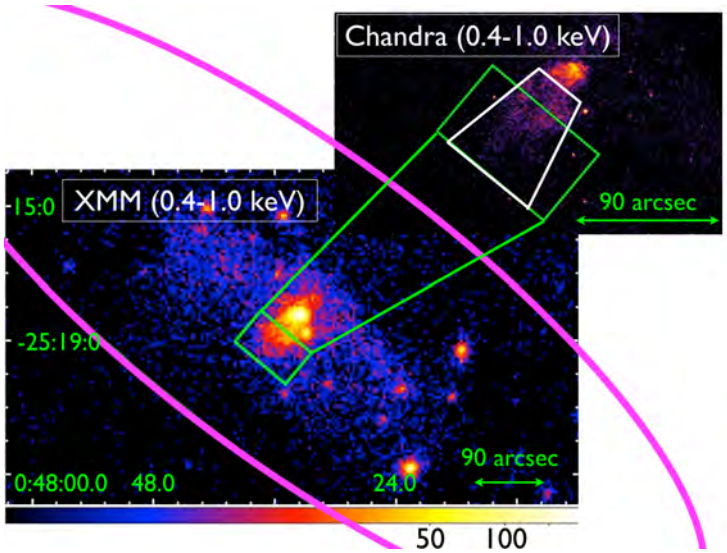

Figure 6.1 *XMM-Newton* MOS1 image and a close-up image of *Chandra* in 0.4–1.0 keV. Green rectangle and magenta ellipse indicate an extracted region for analysis named the superwind region and the optical disk. White trapezoid shows an extracted region to acquire the physical parameters in the superwind region.

background in the MOS detector (Lumb et al., 2002). After background subtraction, we fitted spectra with the ISM by the $vapec_{\rm ISM:1\ T,\ 2\ T\ or\ 3\ T}$ model and a sum of an emission from point sources modeled by *zbremss* with a temperature fixed 10 keV for the hard component due to mainly low mass X-ray binaries (LMXBs). In our interesting energy band below 5 keV, the difference of adopted models to express point-source emissions such as *zbremss* and *power-law* is small and we confirmed that the best fit parameters are consistent with obtained by models of *zbremss* with a temperature of 7 keV or 10 keV and *power-law*. Resultant spectra and the best fit parameters are shown in Figure 6.2 and Table 6.1. For the 1 T model, residuals e.g., around O VII and Mg XII lines, still remain because resulting temperature of k$T \sim 0.38$ keV can not emit observed lines at the same time. Therefore, we added another plasma component with a different temperature whose metal abundances were linked to the other. The low temperature plasma of k$T \sim 0.21$ keV is responsible for mainly O and Ne lines, while the high temperature plasma of k$T \sim 0.62$ keV makes up for mainly Fe L, Mg and Si lines and the fit improved dramatically. Although we also tried the 3 T model, the fit did not improve significantly. The temperature of the additional plasma is above 18 keV, which means that the third plasma is required to cover a continuum emission above 2 keV substituting the *zbremss* model to explain the sum of emissions from point sources. Therefore 2T seems sufficient to reproduce

the temperature structure in the supwerwind region. Since we are interested in the abundance ratio, we extracted abundance ratios for 2 T and 3 T models fixing the Fe abundance to the best fit values, respectively as shown in Figure 6.3. The obtained abundance ratios in this thesis are normalized by solar ratios that we assume. This means that the observed abundance ratios of [Z/Fe] are [Z/Fe] / $[Z/Fe]_{\odot}$ in full. Thus, to convert these observed abundance ratios to number ratios, the solar abundance table we utilize is needed and shown in Appendix B. To confirm our assumption that the abundance ratio does not change for the absolute value of the Fe abundance, we also extracted abundance ratios fixing the Fe abundance to 0.1 and 1 $Z_{\odot}$ for both 2 T and 3 T models. Abundance ratios for these cases are consistent with each other within the statistical errors and are shown in Figure 6.4.

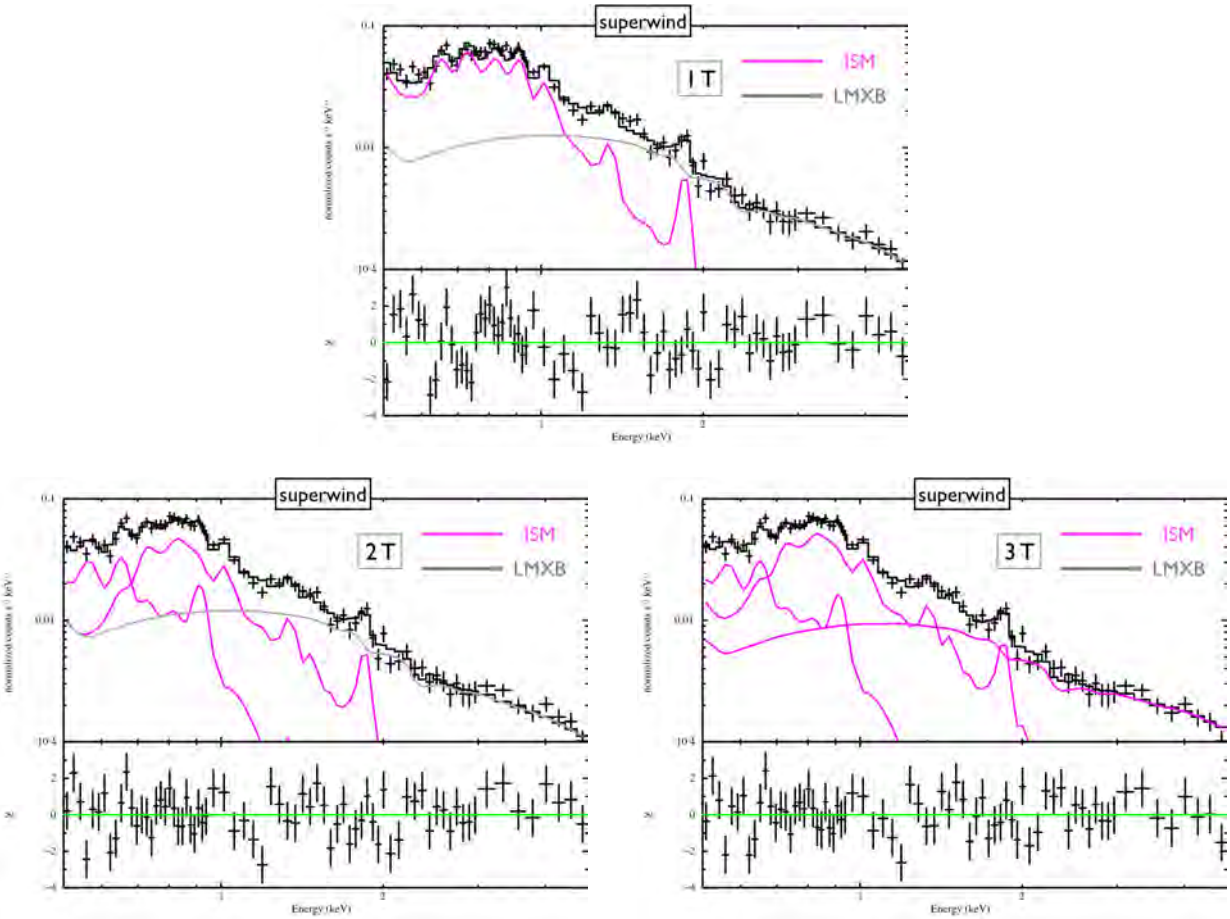

Figure 6.2 Spectra obtained by *XMM-Newton* MOS detectors at the energy band of 0.5 and 5.0 keV in the superwind region after background subtraction. Each spectrum is fitted with the ISM consisting of one- (top), two- (bottom left) or three-temperature (bottom right) thermal plasmas and the sum of the emission from point sources.

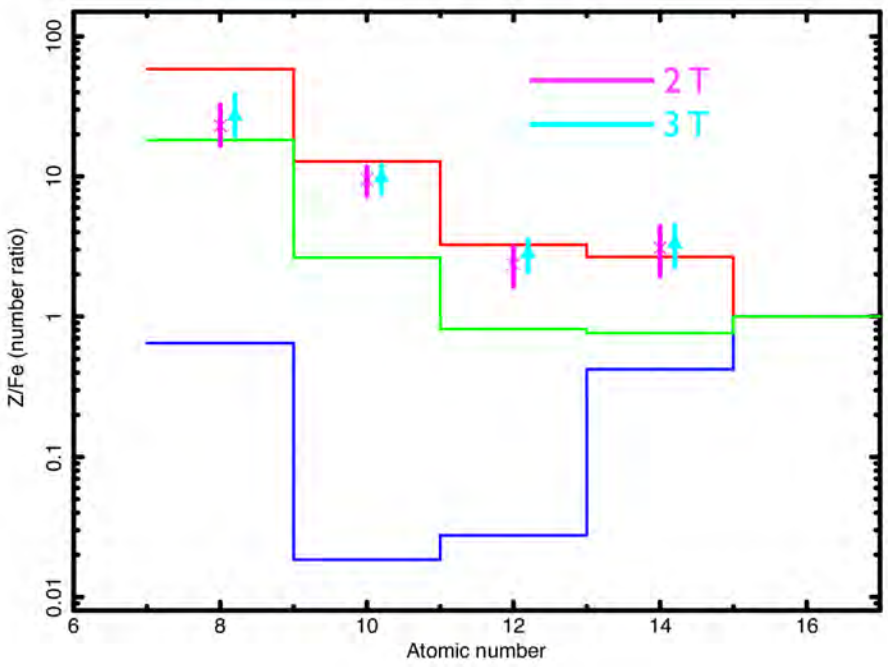

Figure 6.3 Number ratios of O, Ne, Mg, and Si to Fe calculated from resultant abundance ratios for the 2 T and 3 T models with *XMM-Newton* in the superwind region. As comparisons, the number ratios for the solar abundance, SN II and SN Ia products are also plotted (Anders & Grevesse, 1989; Iwamoto et al., 1999; Nomoto et al., 2006).

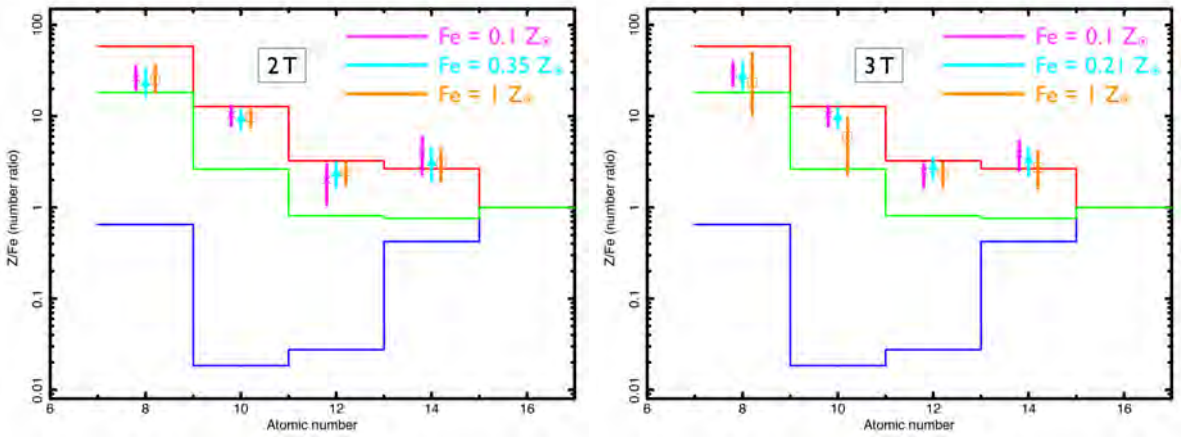

Figure 6.4 Abundance ratios of O, Ne, Mg, and Si to Fe for the 2 T (left) and 3 T (right) models with *XMM-Newton* in the superwind region. In each panel, the abundance of the Fe element is fixed to 0.1, the best fit values as shown in Table 6.1 and 1 $Z_{\odot}$.

6.2.1 Physical parameters in the superwind region with *Chandra*

To derive physical parameters from the spectrum in the superwind region, we utilize the spectrum obtained by *Chandra* not *XMM-Newton* because the "pure" su-

Table 6.1 Best fit parameters for the superwind region by *XMM-Newton*.

Region	Superwind				
Model	$1T$	$2T$	$2T$ (Fe fix)	$3T$	$3T$ (Fe fix)
zphabs ($\times 10^{21}$ [cm^{-1}])	<0.2	<0.5	<0.5	<0.4	<0.4
$kT_{\rm ISM}$ [keV]	0.38±0.02	0.21±0.02	0.21±0.02	0.22±0.02	0.22±0.02
O [Z$_\odot$]	$0.32^{+0.31}_{-0.13}$	$0.44^{+0.60}_{-0.20}$	$0.44^{+0.18}_{-0.12}$	$0.32^{+0.30}_{-0.12}$	$0.32^{+0.14}_{-0.09}$
Ne [Z$_\odot$]	$0.67^{+0.61}_{-0.24}$	$1.3^{+0.99}_{-0.53}$	$1.3^{+0.30}_{-0.29}$	$0.80^{+0.82}_{-0.31}$	$0.80^{+0.19}_{-0.18}$
Mg, Al [Z$_\odot$]	$0.49^{+0.54}_{-0.24}$	$1.0^{+1.1}_{-0.6}$	$1.0^{+0.32}_{-0.31}$	$0.74^{+0.39}_{-0.29}$	0.74±0.19
Si, S, Ar, Ca [Z$_\odot$]	$1.9^{+2.2}_{-0.9}$	$1.4^{+1.1}_{-0.8}$	$1.4^{+0.61}_{-0.52}$	$0.93^{+0.60}_{-0.32}$	$0.93^{+0.33}_{-0.29}$
Fe, Ni [Z$_\odot$]	$0.17^{+0.16}_{-0.06}$	$0.35^{+0.38}_{-0.14}$	0.35 (fix)	$0.21^{+0.16}_{-0.06}$	0.21 (fix)
$Norm_{\rm ISM}$ *	2.0±0.9	$0.84^{+0.99}_{-0.36}$	$0.84^{+0.70}_{-0.25}$	$1.1^{+0.85}_{-0.34}$	$1.1^{+0.78}_{-0.33}$
$kT_{\rm ISM2}$ [keV]		0.62±0.04	0.62±0.04	0.63±0.04	0.63±0.04
$Norm_{\rm ISM2}$ *		$0.70^{+0.41}_{-0.37}$	$0.70^{+0.16}_{-0.09}$	$1.2^{+0.41}_{-0.63}$	$1.2^{+0.22}_{-0.15}$
$kT_{\rm ISM3}$ [keV]				>12	>18
$Norm_{\rm ISM3}$ *				$1.7^{+0.1}_{-1.0}$	$1.7^{+0.1}_{-0.8}$
O/Fe*	$1.9^{+3.8}_{-1.3}$	$1.3^{+3.6}_{-0.9}$	$1.3^{+0.5}_{-0.4}$	$1.5^{+2.6}_{-0.9}$	$1.5^{+0.7}_{-0.4}$
Ne/Fe*	$3.9^{+7.4}_{-2.6}$	$3.6^{+6.9}_{-2.6}$	$3.6^{+0.9}_{-0.8}$	$3.7^{+7.0}_{-2.4}$	3.7±0.9
Mg/Fe*	$2.8^{+6.3}_{-2.1}$	$2.9^{+7.0}_{-2.3}$	$2.9^{+0.9}_{-0.9}$	$3.5^{+4.1}_{-2.3}$	3.5±0.9
Si/Fe*	$10.8^{+25.0}_{-7.7}$	$4.1^{+7.5}_{-3.2}$	$4.1^{+1.7}_{-1.5}$	$4.4^{+5.8}_{-2.7}$	$4.4^{+1.6}_{-1.4}$
$kT_{\rm LMXB}$ [keV]	10.0 (fix)	←	←	←	←
$Norm_{\rm LMXB}$ ‡ ($\times 10^{-5}$)	5.3±0.3	5.0±0.3	5.0±0.3	<2.9	<4.5
$\chi^2/d.o.f$	132/65	90/63	90/64	83/61	83/62

* Normalization of the *apec* model divided by a solid angle Ω, assumed in a uniform-sky ARF calculation (20' radius), i.e. $Norm = (1/\Omega)\int n_e n_H\, dV/(4\pi(1+z)^2)D_A^2)$ cm^{-5} sr^{-1} in unit of 10^{-14}, where D_A is the angular diameter distance.

† Surface brightness of the $power-law$ model in the unit of photons s^{-1} cm^{-2} sr^{-1} keV^{-1} at 1 keV.

‡ i.e. $Norm = \int n_e n_H dV/(4\pi D^2)$ cm^{-5} sr^{-1} in the unit of 3.02×10^{-15}, where D is the distance to the source.

* Abundance ratios of [Z/Fe] to solar ratios of [Z/Fe]$_\odot$.

perwind phenomenon occurs nearby the nuclear region which needs an arcsecond spatial resolution to separate. Thus, we carry out spectrum analysis as is the case of *XMM-Newton* and also extract abundance ratios to confirm the consistency with *XMM-Newton* analysis. The extracted region is indicated in Figure 6.1 as the white trapezoid. This region is placed 20″ away from the nuclear region because Westmoquette et al. (2011) shows Hα-emitting gas layers must be dynamically stable from 20″ away from the nuclear region along with the minor axis compared to a chaotic central region within 20″ region. From this point of view, 20″ can be an indicator as a boundary between the nuclear and the superwind regions. This is almost consistent with that of 27″ by Strickland et al. (2000). We adopt a narrow 26° opening angle (Strickland et al., 2000) for the superwind rather than that of 60° (Westmoquette et al., 2011) to reduce the uncertainty of a filling factor. Resultant spectra, abundance

ratios and the best fit parameters are shown in Figures 6.5, 6.6 and Table 6.2. As with *XMM-Newton* analysis, a two temperature model seems to be preferable because a ∼0.3 keV plasma in a one-temperature model is forced to emit an emission line of Si with an unacceptable abundance ratio and the third plasma does not be required physically (see Figure 6.5 right). Temperatures and abundance ratios are consistent with those obtained by *XMM-Newton* although several emission line features that are detected by *XMM-Newton* can not be observed. Therefore, for abundance ratios, we adopt results of *XMM-Newton* as a final result.

We extract physical parameters from the fitting results with the model $2T$ with the Fe abundance set as a free parameter. A volume is assumed to be a conical shape and calculated to be 1.7×10^{64} cm^{-3}. Resulting parameters are indicated in Table 6.3. As a typical distance from the nuclear region to the disk region, we adopted 7.6×10^{2} pc] which indicated a distance from the nuclear region to the middle point in the extracted superwind region. The equations used to derive the values in Table 6.5 is the same as for Table 5.3.

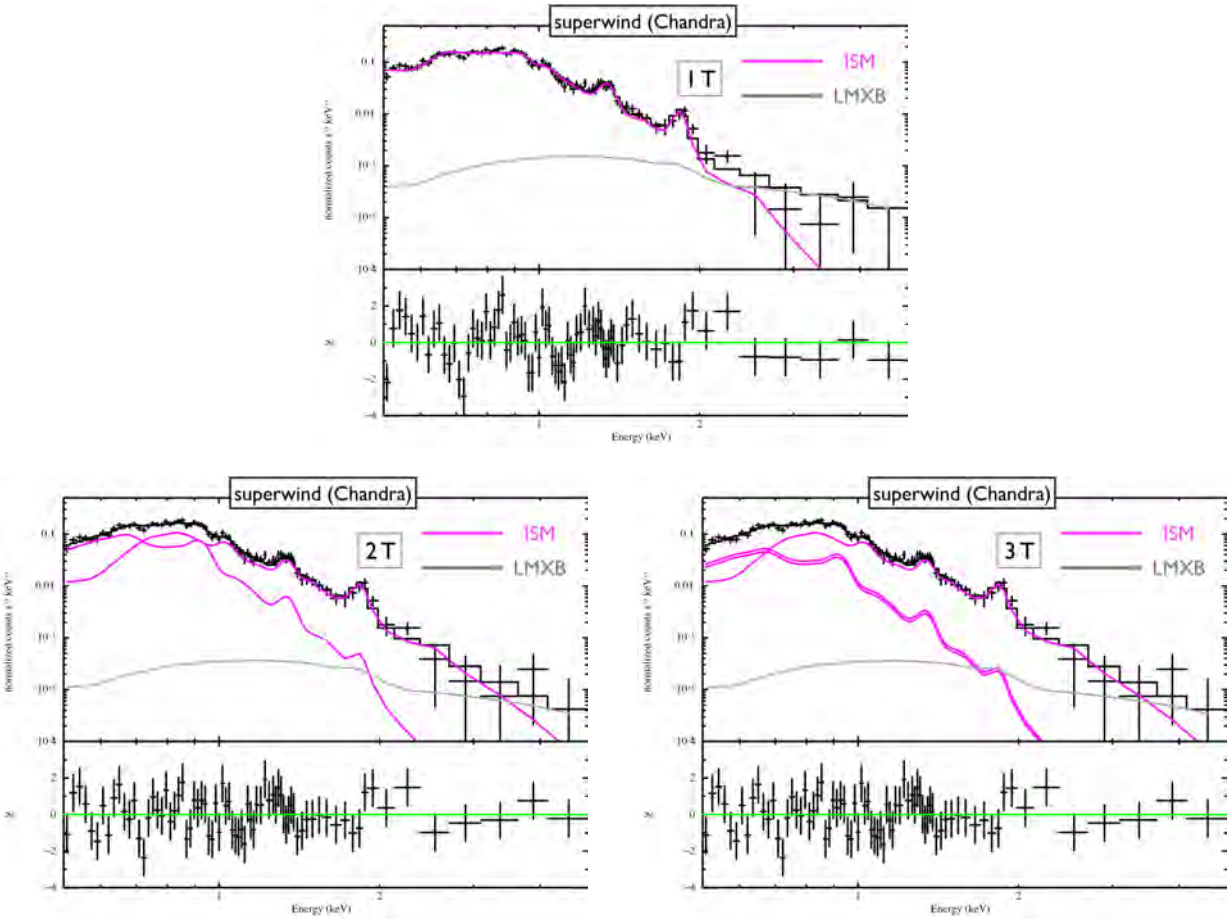

Figure 6.5 The same as Figure 6.2 but obtained by *Chandra*.

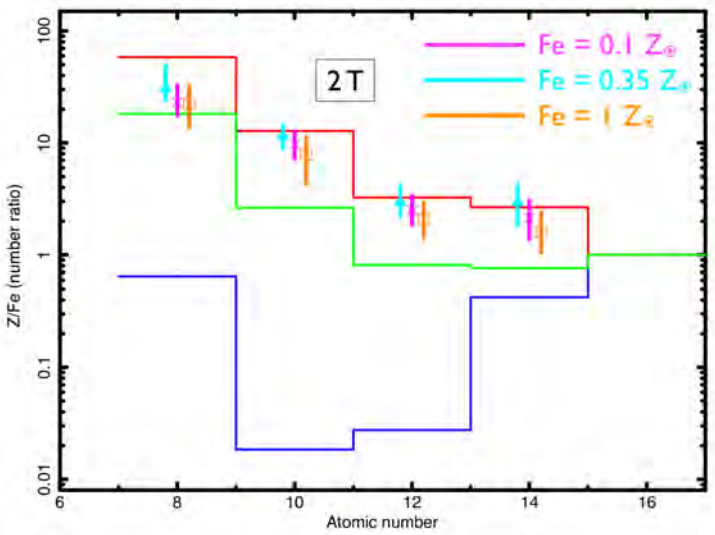

Figure 6.6 The same as Figure 6.3 but obtained by *Chandra*.

Table 6.2 Best fit parameters for the superwind region by *Chandra*.

Region	Superwind			
Model	$1T$	$2T$	$2T$ (Fe fix)	$3T$
$zphabs$ ($\times 10^{21}$ [cm^{-1}])	$1.8^{+0.6}_{-0.9}$	$1.5^{+1.0}_{-1.1}$	$1.5^{+0.9}_{-1.0}$	$1.5^{+1.0}_{-1.1}$
$kT_{\rm ISM}$ [keV]	0.31±0.02	$0.22^{+0.05}_{-0.02}$	$0.22^{+0.05}_{-0.02}$	$0.22^{+68}_{-0.22}$
O [Z$_\odot$]	$0.25^{+0.13}_{-0.07}$	$0.32^{+0.60}_{-0.20}$	$0.32^{+0.18}_{-0.12}$	$0.31^{+0.30}_{-0.12}$
Ne [Z$_\odot$]	$0.43^{+0.21}_{-0.12}$	$0.93^{+0.99}_{-0.53}$	$0.93^{+0.30}_{-0.29}$	$0.92^{+0.82}_{-0.31}$
Mg, Al [Z$_\odot$]	$0.53^{+0.27}_{-0.17}$	$0.78^{+1.1}_{-0.6}$	$0.78^{+0.32}_{-0.31}$	$0.77^{+0.39}_{-0.29}$
Si, S, Ar, Ca [Z$_\odot$]	$1.1^{+0.6}_{-0.4}$	$0.71^{+1.1}_{-0.8}$	$0.71^{+0.61}_{-0.52}$	$0.70^{+0.60}_{-0.32}$
Fe, Ni [Z$_\odot$]	$0.14^{+0.06}_{-0.03}$	$0.25^{+0.38}_{-0.14}$	0.25 (fix)	$0.25^{+0.16}_{-0.06}$
$Norm_{\rm ISM}$				
$kT_{\rm ISM2}$ [keV]		$0.56^{+0.06}_{-0.08}$	0.56±0.04	$0.22^{+68}_{-0.22}$
$Norm_{\rm ISM2}$				
$kT_{\rm ISM3}$ [keV]				$0.56^{+0.16}_{-0.07}$
$Norm_{\rm ISM3}$				
O/Fe*	$1.7^{+1.7}_{-0.9}$	$1.3^{+2.3}_{-0.8}$	$1.3^{+0.6}_{-0.3}$	$1.3^{+2.3}_{-0.8}$
Ne/Fe*	$3.0^{+2.8}_{-1.5}$	$3.7^{+5.9}_{-2.3}$	$3.7^{+1.1}_{-0.9}$	$3.7^{+5.9}_{-2.3}$
Mg/Fe*	$3.7^{+3.7}_{-1.9}$	$3.1^{+5.1}_{-2.0}$	$3.1^{+1.1}_{-0.8}$	$3.1^{+5.1}_{-1.9}$
Si/Fe*	$7.8^{+8.3}_{-4.4}$	$2.8^{+4.7}_{-1.9}$	$2.8^{+1.2}_{-1.0}$	$2.8^{+4.7}_{-1.9}$
$kT_{\rm LMXB}$ [keV]	10.0 (fix)	←	←	←
$Norm_{\rm LMXB}{}^\ddagger$ ($\times 10^{-6}$)	6.0±3.4	$1.4^{+4.1}_{-1.4}$	$1.4^{+4.0}_{-1.4}$	$1.4^{+4.1}_{-1.4}$
$\chi^2/d.o.f$	96/68	71/66	71/67	71/64

* Normalization of the *apec* model divided by a solid angle Ω, assumed in a uniform-sky ARF calculation (20' radius), i.e. $Norm = (1/\Omega)\int n_e n_H\, dV/(4\pi(1+z)^2)D_A^2)$ cm^{-5} sr^{-1} in unit of 10^{-14}, where D_A is the angular diameter distance.

† Surface brightness of the $power-law$ model in the unit of photons s^{-1} cm^{-2} sr^{-1} keV^{-1} at 1 keV.

‡ i.e. $Norm = \int n_e n_H\, dV/(4\pi D^2)$ cm^{-5} sr^{-1} in the unit of 3.02×10^{-15}, where D is the distance to the source.

⋆ Abundance ratios of [Z/Fe] to solar ratios of [Z/Fe]$_\odot$.

Table 6.3 Physical parameters for the two-temperature model in the superwind region

Parameters \ Plasma	ISM1	ISM2
kT [keV]	$0.22^{+0.05}_{-0.02}$	$0.56^{+0.06}_{-0.08}$
L^* [10^{39} erg s^{-1}]	$0.46^{+0.56}_{-0.26}$	$0.41^{+0.12}_{-0.10}$
n_H [$f^{-1/2}$ 10^{-2} cm^{-3}]	$6.4^{+7.6}_{-5.2}$	$4.2^{+2.7}_{-2.4}$
P/k [$f^{-1/2}$ 10^5 K cm^{-3}]	$1.6^{+2.7}_{-1.3}$	$2.7^{+2.3}_{-1.7}$
$E_{th}{}^{\dagger}$ [$f^{1/2}$ 10^{53} erg]	$5.6^{+5.0}_{-2.7}$	$9.5^{+3.1}_{-2.8}$
$t_{cool}{}^{\ddagger}$ [$f^{1/2}$ Myr]	$14.3^{+78.2}_{-8.5}$	$56.0^{+89.5}_{-26.5}$

* Unabsorbed luminosity in 0.5–10.0 keV assuming the distance to 3.4 [Mpc].

† Thermal energy.

‡ Radiative cooling time using 3 kT / Λn_e.

6.3 Disk region with *XMM-Newton*

To extract a physical properties of hot gas fulfilling the disk region of NGC 253, *XMM-Newton* is utilized because a contribution of point sources associated with starburst activities is still high even in the soft band below 1 keV. To improve line-to-continuum ratio, we excluded point sources with a radius of 10 arcsec as shown in Figure 6.7 by WAVDETECT algorithm in the CIAO software package which search for significant X-ray sources. To define the disk region, we adopt the optical disk B25 but excluding point sources and the central 2 arcmin to distinguish from the superwind and nuclear regions. The background region was selected from a source-free region.

The same analysis as the superwind region was carried out for the disk region. After background subtraction, we try to model a spectrum with the ISM (one-, two- or three-temperature plasma) and a sum of a point source emission. In obtained spectra, two strong instrumental fluorescent lines of Al (∼1.49 keV) and Si (∼1.74 keV) were not subtracted properly. Since the first line was subtracted too much which gave rise to a large residual around 1.49 keV, we ignored the energy band between 1.45 keV and 1.55 keV. On the other hand, because the second fluorescent line was not subtracted enough, we add a gaussian component to make up for this residual fixing the line energy to 1.74 keV. We did not ignore this energy band because this is informative for the abundance ratio of Si/Fe. Although we extracted a background region from other three regions in different CCD chips, these instrument lines were not subtracted properly. Difference of the background level in a different CCD chip detector on the same detector was reported in Lumb et al. (2002).

Then, we proceeded to spectral analysis taking measures the well-known instrument problem. Resultant spectra and the best fit parameters are shown in Figure 6.8 and Table 6.4. In the 1 T ISM model, residuals corresponding to O VII and Fe L around 0.8 keV emission lines still reside, which indicates that 1 T ISM cannot emit all of observed emission lines. For the 2 T ISM model, the fit improves dramatically from $\chi/d.o.f = 118/81$ to 83/79 and residuals in the 1 T ISM model disappear. We added one more plasma and found that the fit slightly improved. As the lowest-temperature plasma is responsible for mainly O VII emission line only, all of three plasmas does not necessarily be required. Thus, from this point of view, we concluded that the 2 T model is enough. However, we extracted abundance ratios for both 2 T and 3 T models fixing the Fe abundance to the best fit values as indicated in Table 6.4 and confirmed that resulting abundance ratios are consistent with cases fixing the Fe

abundance to 0.1 and 1 $Z_{\odot}$, respectively. These results are shown in Figure 6.9 and 6.10.

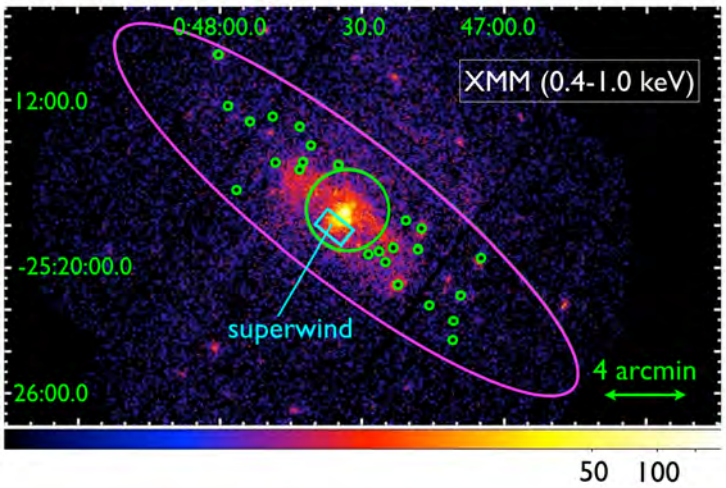

Figure 6.7 *XMM-Newton* MOS1 image in 0.4–1.0 keV. Magenta ellipse and green circles indicate the optical disk and removed regions for spectral analysis. Smaller green circles are circular regions with a radius 10 arcsec corresponding to point-source positions, while the larger green circle shows a circular region with a radius of 2 arcmin to avoid a contamination from the nuclear and the superwind regions. Cyan rectangle is the superwind region. As the disk region, we extracted a region within the optical disk but excluding point sources and the central 2 arcmin.

6.3.1 Physical parameters in the disk region

To extract physical parameters in the disk region, we adopt the best fit model of the two-temperature model , i.e., $2T$ with Fe abundance not fixed, as shown in Table 6.4. We assume a spheroidal volume of 6.1×10^{67} [cm^{-3}] excluding the central 2 arcmin and the removed point sources regions. Obtained parameters are summarized in Table 6.5. As a typical distance from the nuclear region to the disk region, we adopted 2.6×10^{3} [pc] which indicated a distance from the nuclear region to the middle point between the edge of the central $2'$ region in the disk and the boundary of the optical disk and the extracted halo region.

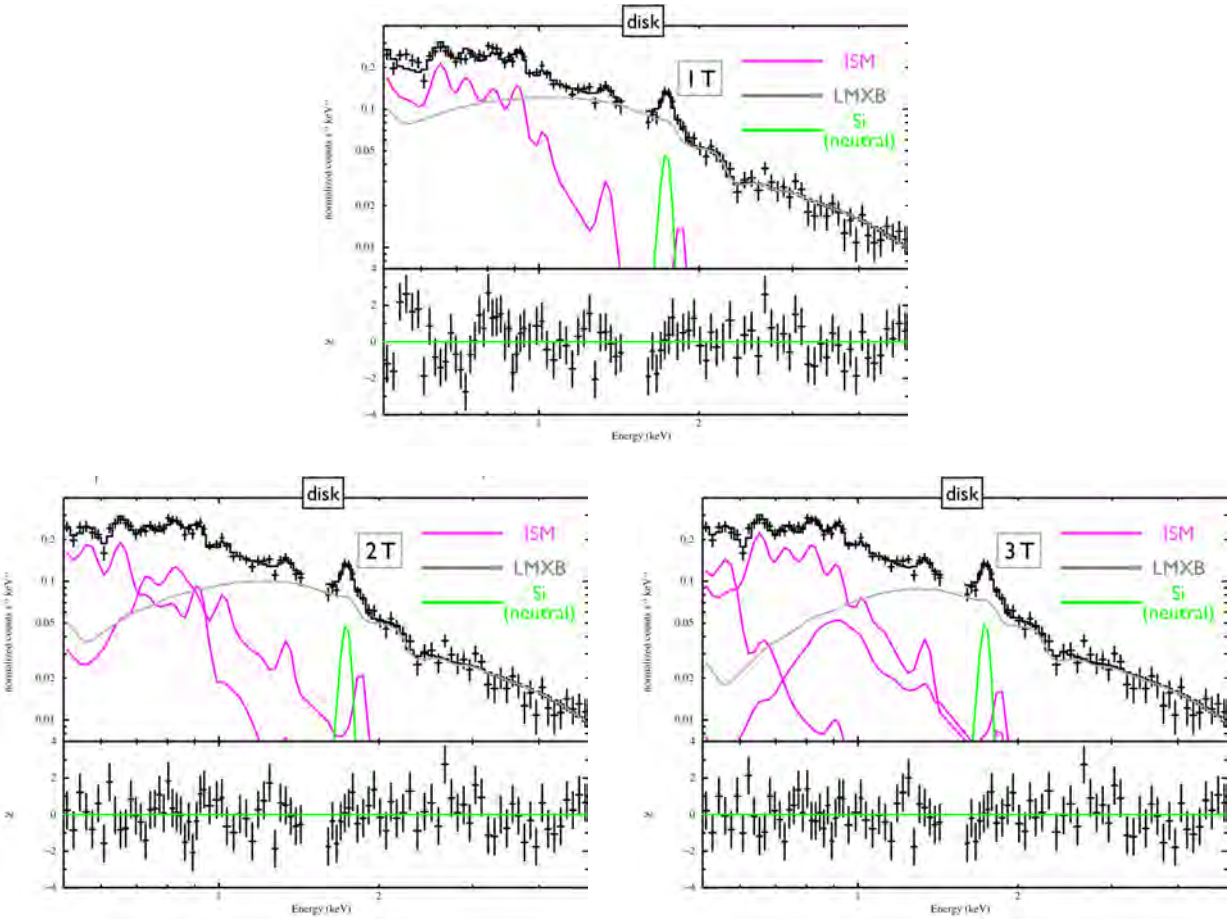

Figure 6.8 Spectra obtained by *XMM-Newton* MOS detectors at the energy band of 0.5 and 5.0 keV in the disk region after background subtraction. Each spectrum is fitted with the ISM consisting of one- (top), two- (bottom left) or three-temperature (bottom right) thermal plasmas, the sum of the emission from point sources and an instrumental line of Si fixing the line energy to 1.74 keV. The energy band between 1.45 keV and 1.55 keV was ignored to remove another instrumental line of Al.

Table 6.4 Best fit parameters for the disk region by *XMM-Newton*.

Region	Disk				
Model	$1T$	$2T$	$2T$ (Fe fix)	$3T$	$3T$ (Fe fix)
$zphabs$ ($\times 10^{21}$ [cm^{-1}])	<0.4	$1.0^{+1.4}_{-0.9}$	$1.0^{+1.4}_{-0.8}$	2.0±1.3	2.0±1.2
$kT_{\rm ISM}$ [keV]	0.32±0.02	0.20±0.02	0.20±0.02	$0.10^{+0.85}_{-0.10}$	$0.09^{+0.11}_{-0.09}$
O [Z$_\odot$]	$0.66^{+101}_{-0.35}$	$0.28^{+0.33}_{-0.09}$	$0.28^{+0.10}_{-0.07}$	$0.38^{+0.31}_{-0.12}$	$0.38^{+0.18}_{-0.13}$
Ne [Z$_\odot$]	$1.1^{+10.8}_{-0.63}$	$0.51^{+0.79}_{-0.21}$	$0.51^{+0.18}_{-0.16}$	$0.30^{+0.34}_{-0.12}$	$0.30^{+0.21}_{-0.12}$
Mg, Al [Z$_\odot$]	$1.4^{+5.3}_{-0.7}$	$0.49^{+0.92}_{-0.26}$	$0.49^{+0.29}_{-0.21}$	$0.45^{+0.55}_{-0.22}$	$0.45^{+0.27}_{-0.18}$
Si, S, Ar, Ca [Z$_\odot$]	$6.3^{+150}_{-1.6}$	$1.1^{+1.6}_{-0.6}$	$1.1^{+0.8}_{-0.5}$	$0.90^{+1.2}_{-0.43}$	$0.90^{+0.67}_{-0.41}$
Fe, Ni [Z$_\odot$]	$0.36^{+3.7}_{-0.24}$	$0.19^{+0.22}_{-0.06}$	0.19 (fix)	$0.21^{+0.13}_{-0.07}$	0.21 (fix)
$Norm_{\rm ISM}$*	$3.9^{+9.1}_{-3.8}$	19^{+53}_{-15}	19^{+51}_{-12}	96^{+851}_{-86}	154^{+784}_{-143}
$kT_{\rm ISM2}$ [keV]		$0.57^{+0.08}_{-0.21}$	$0.57^{+0.07}_{-0.25}$	$0.29^{+0.04}_{-0.06}$	$0.29^{+0.03}_{-0.05}$
$Norm_{\rm ISM2}$*		$5.3^{+8.5}_{-3.6}$	$5.3^{+7.6}_{-2.0}$	22^{+28}_{-16}	22^{+27}_{-15}
$kT_{\rm ISM3}$ [keV]				$0.86^{+0.12}_{-0.23}$	$0.86^{+0.12}_{-0.20}$
$Norm_{\rm ISM3}$*				$2.9^{+2.7}_{-1.8}$	$2.9^{+2.7}_{-1.8}$
O/Fe*	$1.8^{+861}_{-1.8}$	$1.5^{+3.4}_{-1.0}$	$1.5^{+0.5}_{-0.4}$	$1.8^{+3.0}_{-1.1}$	$1.8^{+0.9}_{-0.6}$
Ne/Fe*	$3.1^{+97.8}_{-3.0}$	$2.7^{+7.7}_{-2.0}$	$2.7^{+0.9}_{-0.8}$	$1.4^{+3.1}_{-0.9}$	$1.4^{+1.0}_{-0.6}$
Mg/Fe*	$4.0^{+53.0}_{-3.8}$	$2.6^{+8.6}_{-2.0}$	$2.6^{+1.5}_{-1.1}$	$2.2^{+4.9}_{-1.5}$	$2.2^{+1.3}_{-0.9}$
Si/Fe*	$17.4^{+1310}_{-16.3}$	$5.6^{+15.9}_{-4.4}$	$5.6^{+4.1}_{-2.6}$	$4.3^{+10.4}_{-2.9}$	$4.3^{+3.2}_{-2.0}$
$kT_{\rm LMXB}$ [keV]	10.0 (fix)	←	←	←	←
$Norm_{\rm LMXB}$‡ ($\times 10^{-4}$)	5.7±0.2	$5.6^{+0.4}_{-0.3}$	$5.6^{+0.4}_{-0.3}$	5.6±0.3	5.6±0.3
$\chi^2/d.o.f$	118/81	83/79	83/80	78/77	78/78

* Normalization of the *apec* model divided by a solid angle Ω, assumed in a uniform-sky ARF calculation (20' radius), i.e. $Norm = (1/\Omega)\int n_e n_H\, dV/(4\pi(1+z)^2)D_A^2)$ cm^{-5} sr^{-1} in unit of 10^{-14}, where D_A is the angular diameter distance.

† Surface brightness of the $power-law$ model in the unit of photons s^{-1} cm^{-2} sr^{-1} keV^{-1} at 1 keV.

‡ i.e. $Norm = \int n_e n_H dV/(4\pi D^2)$ cm^{-5} sr^{-1} in the unit of 3.02×10^{-15}, where D is the distance to the source.

* Abundance ratios of [Z/Fe] to solar ratios of [Z/Fe]$_\odot$.

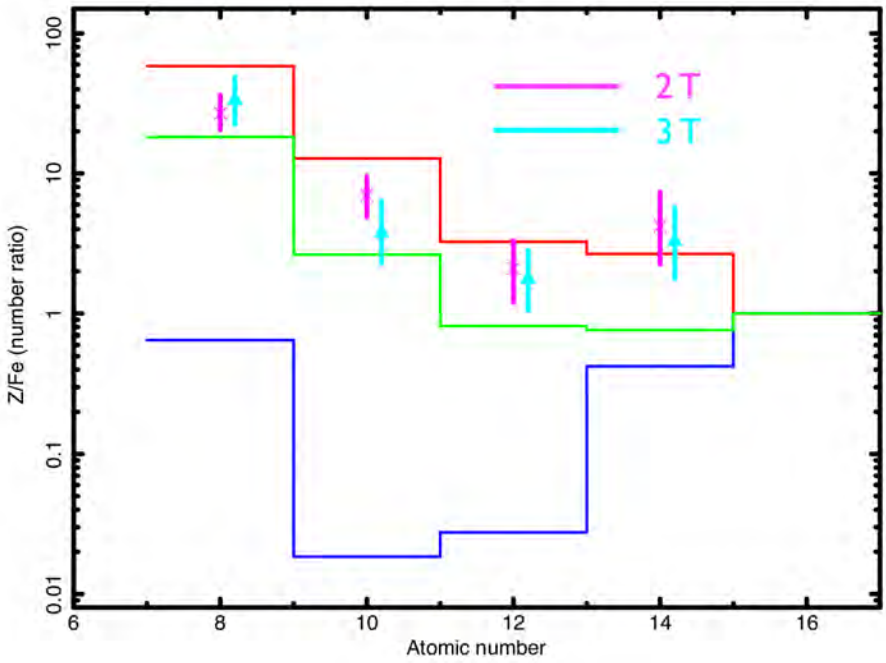

Figure 6.9 Number ratios of O, Ne, Mg, and Si to Fe calculated from resultant abundance ratios for the 2 T and 3 T models with *XMM-Newton* in the disk region. As comparisons, the number ratios for the solar abundance, SN II and SN Ia products are also plotted (Anders & Grevesse, 1989; Iwamoto et al., 1999; Nomoto et al., 2006).

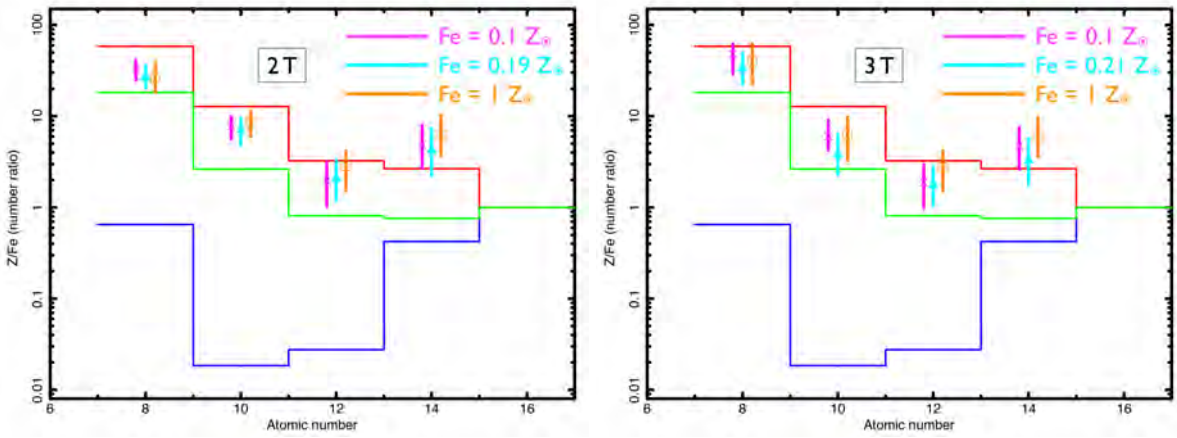

Figure 6.10 Abundance ratios of O, Ne, Mg, and Si to Fe for the 2 T (left) and 3 T (right) models with *XMM-Newton* in the disk region. In each panel, the abundance of the Fe element is fixed to 0.1, the best fit values as shown in Table 7.2 and 1 $Z_{\odot}$.

Table 6.5 Physical parameters for the two-temperature model in the disk region

Parameters \ Plasma	ISM1	ISM2
kT [keV]	0.20±0.02	$0.57^{+0.08}_{-0.21}$
L^* [10^{39} erg s^{-1}]	$1.1^{+2.2}_{-0.6}$	$0.7^{+0.7}_{-0.3}$
n_H [$f^{-1/2}$ 10^{-3} cm^{-3}]	$1.9^{+3.3}_{-1.7}$	$1.0^{+1.3}_{-0.8}$
P/k [$f^{-1/2}$ 10^3 K cm^{-3}]	$4.3^{+8.9}_{-3.9}$	$6.6^{+9.7}_{-5.7}$
E_{th}† [$f^{1/2}$ 10^{55} erg]	$5.6^{+6.6}_{-3.3}$	$8.6^{+7.1}_{-5.5}$
t_{cool}‡ [$f^{1/2}$ 10^2 Myr]	$4.4^{+42.0}_{-2.9}$	$42.2^{+197.3}_{-30.7}$

* Unabsorbed luminosity in 0.5–10.0 keV assuming the distance to 3.4 [Mpc].

† Thermal energy.

‡ Radiative cooling time using 3 kT / Λn_e.

7 Analysis & Results: Halo region of NGC 253

7.1 Energy spectrum from the halo region obtained by *Suzaku*

The NGC 253 and offset region images obtained by *Suzaku* in 0.4 – 2 keV is shown in Figure 7.1. There are clear halo emission up to 8 kpc from the disk, but the surface brightness is less than that of the disk region. Careful treatment of the background subtraction and stray-light contamination from the brighter area are hence important. We first investigate the spectral analysis procedure.

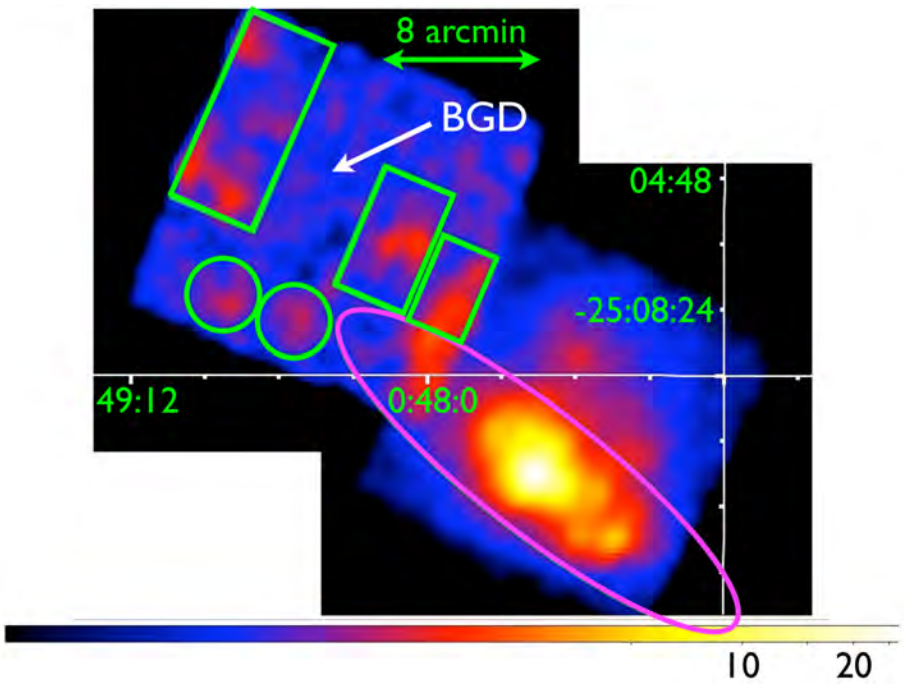

Figure 7.1 Merged XIS1 image of the offset region and NGC 253 in 0.4–2.0 keV in the unit of cts $(10\ \mathrm{ks})^{-1}$ $(256\ \mathrm{pixel})^{-1}$. Magenta ellipse indicates an optical disk of NGC 253. The background region was selected in the offset region but excluding the optical disk and green circles and rectangles.

7.1.1 Background estimation

We evaluated the background using the offset region just next to NGC 253 as shown in Figure 7.1, because it is difficult to take a background region in the FOV. In the offset region, we excluded point sources by WAVDETECT algorithm and some bright regions by eye for diffuse emission along with the optical disk, which are indicated in Figure 7.1. Then we obtained an energy spectra for OFFSET region. First, we subtract the non X-ray background using the dark Earth data, in the same way as previous chapters. Next we fit the spectrum with typical X-ray background model with the Galactic foreground emission and the CXB (e.g. Yoshino et al., 2009; Kushino et al., 2002). The model is expressed by an Xspec-model as $apec_{\rm LHB}$ + $phabs$ × ($apec_{\rm MWH}$+ $power\text{-}law$). A result of a spectrum fitting of the offset region is shown in Figure 7.2 and resultant parameters are summarized in Table 7.1. We used this spectrum afterwords as the background emission for analysis of the halo region.

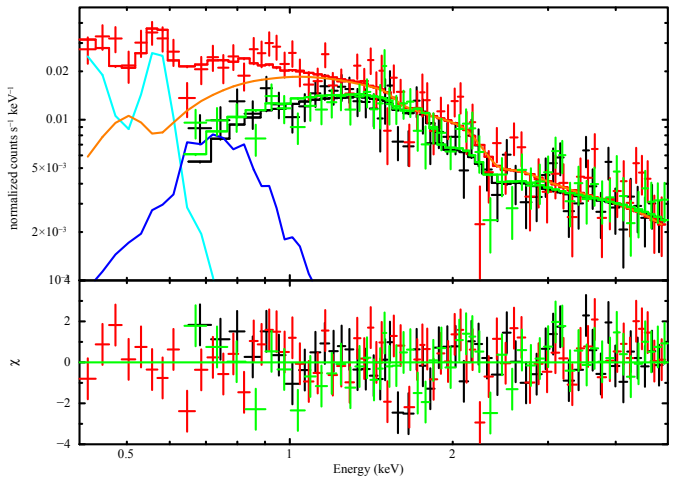

Figure 7.2 A spectrum of the OFFSET region as defined in Figure 6.1 fitted with the typical X-ray background model as below: $apec_{\rm LHB}$ + $phabs$×($apec_{\rm MWH}$ + $power-law$). Cyan, blue and orange indicate LHB, MWH and CXB components for XIS1. Black and green lines correspond to XIS0 and XIS3, respectively.

Table 7.1 Best fit parameters of the OFFSET region.

REGION	OFFSET
$kT_{\rm LHB}$ [keV]	$0.07^{+0.02}_{-0.01}$
$Norm_{\rm LHB}(\times10^2)^*$	$2.3^{+10.2}_{-1.7}$
$kT_{\rm MWH}$ [keV]	$0.29^{+0.10}_{-0.06}$
$Norm_{\rm MWH}$ $(\times10^{-4})^*$	$1.8^{+1.1}_{-0.7}$
Γ (fix)	1.4 (fix)
$SB^\dagger$	8.7±0.3
$\chi^2/d.o.f$	196/171

* Normalization of the *apec* model divided by a solid angle Ω, assumed in a uniform-sky ARF calculation (20' radius), i.e. $Norm = (1/\Omega)\int n_e n_H\, dV/(4\pi(1+z)^2)D_A^2)$ cm^{-5} sr^{-1} in unit of 10^{-14}, where D_A is the angular diameter distance.
† Surface brightness of the $power-law$ model in the unit of photons s^{-1} cm^{-2} sr^{-1} keV^{-1} at 1 keV.

7.1.2 Estimation for the stray-light from the central bright region

Considering the *Suzaku* angular resolution (1′.8 as a half-power diameter), stray-light as a contamination emission from the brighter central region has to be evaluated

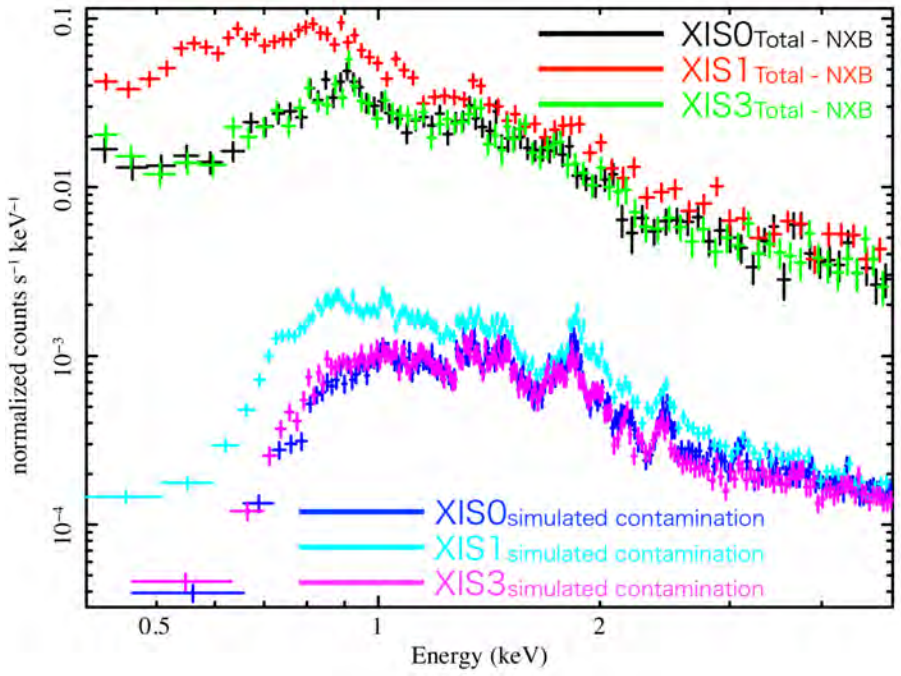

Figure 7.3 Spectral comparison between NXB subtracted spectra of *Suzaku* XIS0 (black), XIS1 (red) and XIS3 (green) in the halo region and simulated spectra which show the contamination from the brighter central region.

before extracting physical properties of hot ISM in the halo region itself. We extract a central 20″ region around the nuclear region covering the nuclear region discussed in §5, the brightest point source and the superwind region. This region includes about two thirds of the total flux of a central 90″ region in our interesting energy band between 0.4 keV and 5.0 keV despite the area of <5 %. This selected region can be considered to be a point-like region compared to the *Suzaku* angular resolution. Then, a spectrum fitting for this selected region is performed and the spectrum is represented well by three thin thermal plasmas and a *power-law* component with $\chi^2/d.o.f = 261/227$. Note that not physical interpretation of adopted models but the goodness of the fit is important to describe the emission empirically. We input these parameters and a flux into a ray-tracing simulator (xissimarfgen ftool: Ishisaki et al. (2007)), and compared the spectra of the halo and simulated stray-light as shown in Figure 7.3. An estimated count rate from the inner bright region is about 2-3 $\times 10^{-3}$ cts s^{-1}, which is less than 4 % compared to NXB subtracted spectra in the halo region at the energy range between 0.4 and 5.0 keV. It is below the uncertainty of the foreground and subtracted NXB. Thus, we conclude that the contamination from the inner brighter emission is negligible.

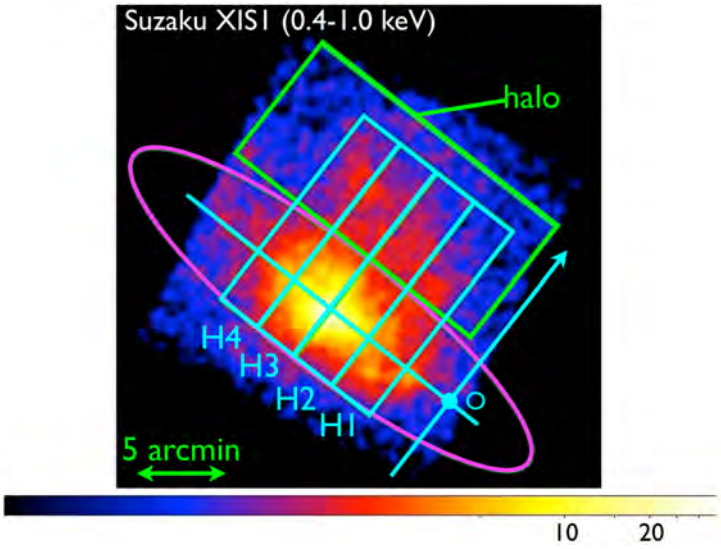

Figure 7.4 *Suzaku* XIS1 image of NGC 253 in 0.4–1.0 keV in the unit of cts (101 ks)$^{-1}$ (64 pixel)$^{-1}$. Magenta ellipse and green rectangle indicate an optical disk and the extracted region as the whole halo region. Cyan rectangles divided into 4 regions denoted as H1, H2, H3 and H4 are the extracted region for analysis of surface brightness profiles.

7.1.3 Spectral fitting of the whole halo region

We construct the energy spectrum for the halo region shown in Figure 7.4. The spectrum, as shown in Figure 7.5, shows strong emission including Oxygen emission lines below 1 keV, and above 2 keV band. The former is considered to be thin-thermal plasma emission from the hot ISM, and latter is to be a sum of point sources such as low-mass X-ray binaries (LMXBs) which is responsible for the hard energy band, respectively. The ISM component is represented by a sum of *apec* model. The LMXB component is represented by a bremsstrahlung emission of $kT = 10$ keV as the same as in Yamasaki et al. (2009).

We use the all CCD (BI:XIS 1 and FI: XIS 0 and XIS3) data simultaneously, but found a discrepancy in flux for each detector. As shown in Chapter 4, we multiply scaling factors relative to XIS 0 for the total flux and keep the physical parameters between the detector, as the same as Akamatsu et al. (2011).

As a first step, *apec* model was utilized to express the ISM. However, residuals around some emission lines such as Fe L shell and He-like Mg lines still resided. Thus, we varied metal abundances by using *vapec* model which allowed us to vary each abundance and these metal abundances were linked to each other in two-temperature and three-temperature models. We combined metal abundances into five groups as

O, Ne, (Mg & Al), (Si, S, Ar, & Ca), and (Fe & Ni) based on the metal synthesis mechanism of SN. Finally, we fitted the halo region spectra with the following model: $apec_{\rm LHB}$ + $phabs\times$ $apec_{\rm MWH}$ + $phabs\times phabs_{\rm Galactic}\times$($vapec_{\rm 1T,2T,or\ 3T}$ + *zbremss* + *power-law*). The first two terms indicate the Galactic foreground emissions and the first absorption factor (*phabs*) and the second one ($phabs_{\rm Galactic}$) in the third term correspond to column densities of NGC 253 itself and our Galaxy fixing to the Galactic value (Kalberla et al., 2005) as described in §4.1. Resultant spectra and the best fit parameters are shown in Figure 7.5 and Table 7.2.

We extracted abundance ratios to the Fe element for other four groups. Generally, the abundance ratio to the O or Fe elements is often used due to a relatively-small statistical error for the soft plasma emitting O VII, O VIII and Fe L emission lines. In our case, to discuss the abundance ratios of Ne and Mg whose emission lines are nearby Fe L lines fixing the Fe element is thought to be preferable. Resulting abundance ratios to Fe are also summarized in Table 7.2. Although this is the first results for extracting the abundance ratios in the halo region of NGC 253 thanks to *Suzaku* with good sensitivity for a soft plasma, we cannot constrain these ratios well.

To constrain the abundance ratios more tightly, we fixed Fe to the best fit parameters and then we extracted the metal abundances for other four groups. In general, for the soft plasma with a temperature of below $\sim$0.5 keV, a normalization and an abundance in *vapec* model are correlated strongly. In such a soft plasma, a dominant emission mechanism is emission lines from various heavy elements with various ionized states, and not a continuum emission such as bremsstrahlung from hydrogen and helium. This gives rise to the situation that a contribution by line emissions and the continuum emission cannot be distinguished separately from an observed spectrum, but keeping the abundance ratios constant in principle unless a temperature does not change significantly. Therefore, we tried this "Fe fixed" analysis.

Resultant spectra, number ratios calculated from obtained abundance ratios and the best fit parameters fixing the Fe element to the best fit values are shown in Figure 7.5, 7.6 and Table 7.2. In Figure 7.6, as comparisons, we plotted the number ratios for the solar abundance, SN II and SN Ia products (Anders & Grevesse, 1989; Iwamoto et al., 1999; Nomoto et al., 2006). To confirm the indication of this analysis, we extracted the abundance ratios fixing the Fe element to 0.1 $Z_{\odot}$ or 1 $Z_{\odot}$ for all 1 T, 2 T and 3 T models, and confirmed that the abundance ratios are almost consistent with the values obtained by fixing Fe to the best fit values. This suggests that abundance ratios do not change for our "Fe fixed" analysis ranging from 0.1 $Z_{\odot}$ to 1 $Z_{\odot}$. Resulting abundance ratios and the best fit parameters are indicated in Figure 7.7 and Table

7.2.

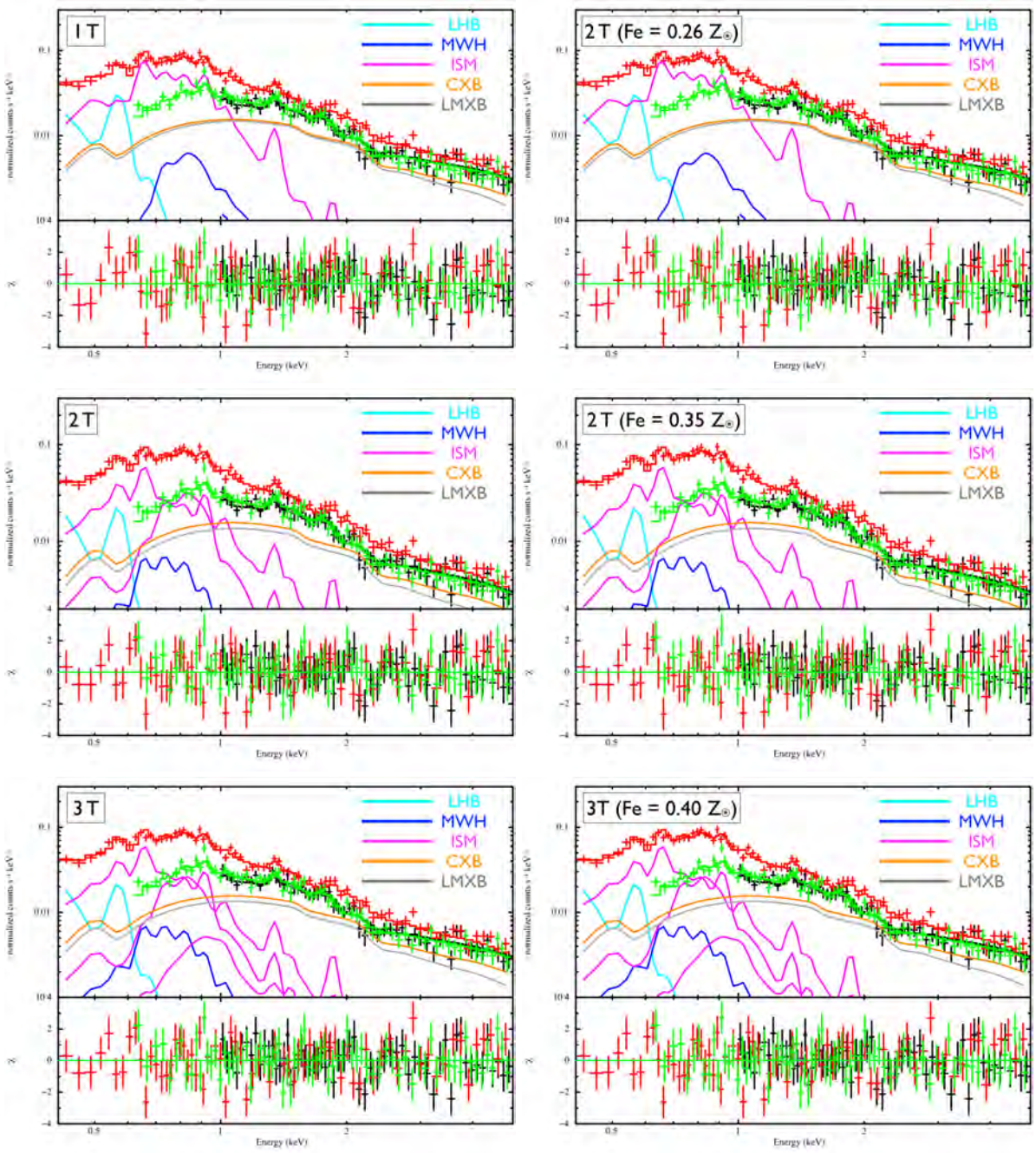

Figure 7.5 *Suzaku* spectra at the energy range between 0.5 and 5.0 keV in the halo region of NGC 253. The lines show the best-fit model that consists of $apec_{\rm LHB}$ (cyan), *phabs*× $apec_{\rm MWH}$ (blue), *phabs*×$phabs_{\rm Galactic}$ *zbremss* + *power-law* (gray and orange) and *phabs*×$phabs_{\rm Galactic}$ $apec_{\rm ISM}$ (magenta). As the ISM component, 1 T (top), 2 T (middle) and 3 T (bottom) thin thermal plasmas are adopted, respectively. A Fe abundance in the ISM component is linked to each other and is set to be free (left) and fixed to the best fit values (right) obtained by a spectral fitting individually.

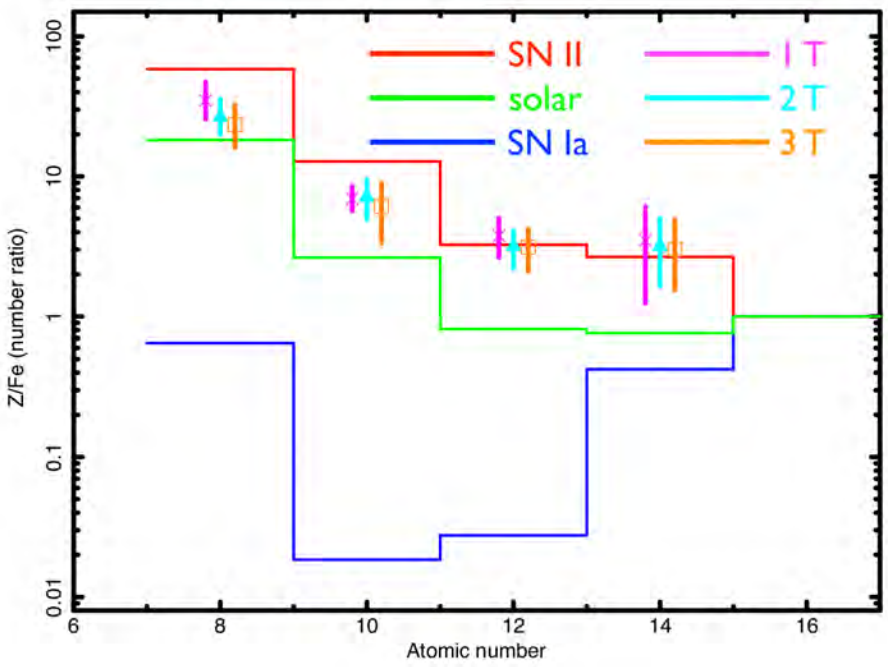

Figure 7.6 Number ratios of O, Ne, Mg, and Si to Fe calculated from resultant abundance ratios for the 1 T, 2 T and 3 T models with *Suzaku* in the halo region. As comparisons, the number ratios for the solar abundance, SN II and SN Ia products are also plotted (Anders & Grevesse, 1989; Iwamoto et al., 1999; Nomoto et al., 2006).

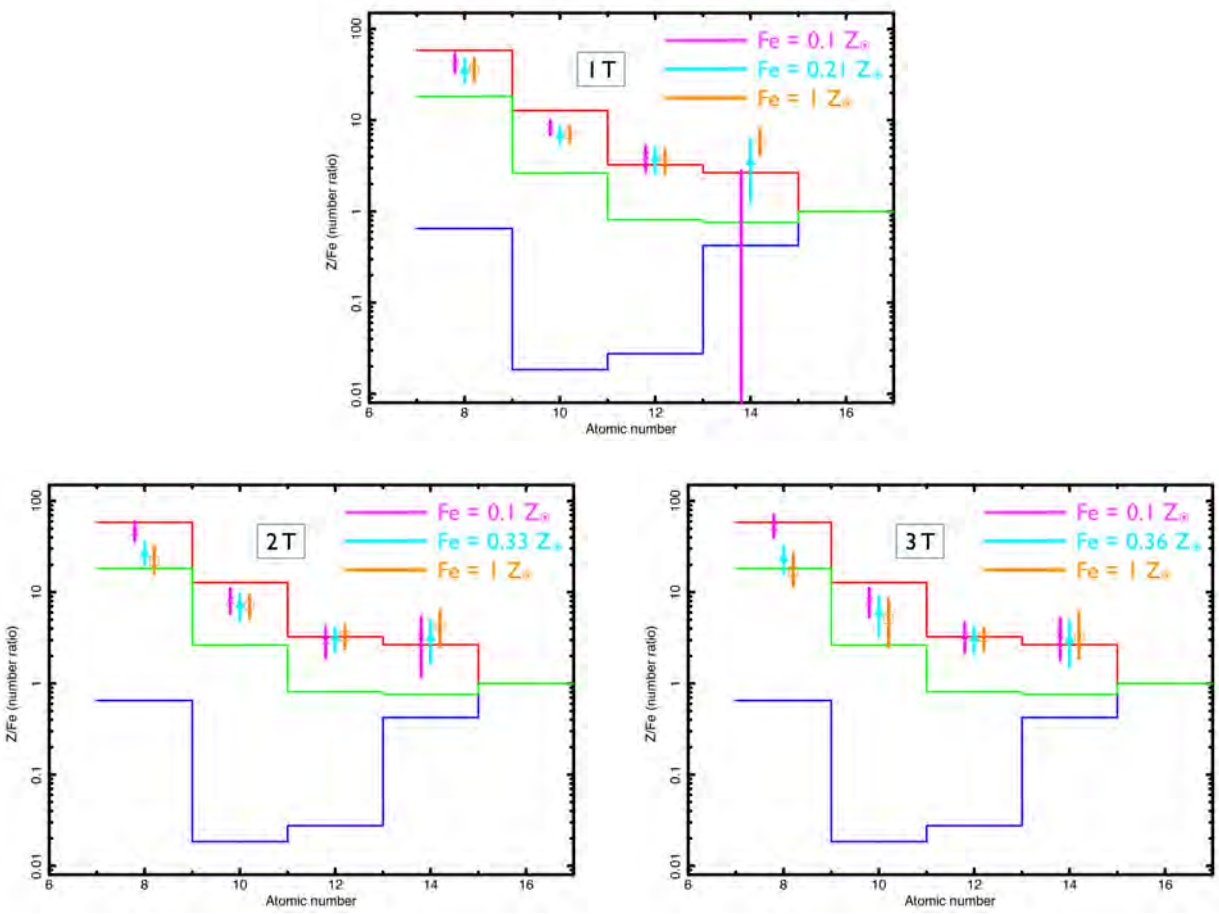

Figure 7.7 Abundance ratios of O, Ne, Mg, and Si to Fe for the 1 T (left), 2 T (middle) and 3 T (right) models with *Suzaku* in the halo region. In each panel, the abundance of the Fe element is fixed to 0.1, the best fit values as shown in Table 7.2 and 1 $Z_{\odot}$.

Table 7.2 Best fit parameters for the halo region by *Suzaku*.

Region	Halo					
Model	$1T$	$1T$ (Fe fix)	$2T$	$2T$ (Fe fix)	$3T$	$3T$ (Fe fix)
f (XIS1)	1.13±0.05	$1.13^{+0.05}_{-0.04}$	1.11±0.05	1.11±0.05	1.11±0.05	1.11±0.05
f (XIS3)	0.88±0.04	0.88±0.04	0.87±0.04	0.87±0.04	0.87±0.04	0.87±0.04
$kT_{\rm LHB}$ [keV]	$0.09^{+0.01}_{-0.02}$	$0.09^{+0.01}_{-0.02}$	$0.07^{+0.02}_{-0.01}$	$0.07^{+0.02}_{-0.01}$	$0.07^{+0.02}_{-0.01}$	$0.07^{+0.02}_{-0.01}$
$Norm_{\rm LHB}{}^{*}/f$	83^{+159}_{-32}	83^{+152}_{-31}	232^{+868}_{-162}	232^{+861}_{-164}	233^{+774}_{-165}	233^{+855}_{-165}
$kT_{\rm MWH}$ [keV]	$0.64^{+0.13}_{-0.41}$	$0.64^{+0.13}_{-0.42}$	$0.28^{+0.10}_{-0.06}$	$0.28^{+0.10}_{-0.06}$	$0.28^{+0.10}_{-0.06}$	$0.28^{+0.10}_{-0.06}$
$Norm_{\rm MWH}{}^{*}/f$	0.75±0.26	$0.75^{+0.26}_{-0.22}$	$1.8^{+1.0}_{-0.7}$	$1.8^{+1.0}_{-0.7}$	$1.9^{+0.7}_{-0.8}$	$1.8^{+1.0}_{-0.8}$
Γ (fix)	1.4 (fix)	←	←	←	←	←
$SB^{\dagger}$	8.6±0.3	8.6±0.3	$8.7^{+0.3}_{-0.2}$	8.7±0.3	8.7±0.3	8.7±0.3
$zphabs$ ($\times10^{21}$ [cm^{-1}])	<0.3	<0.3	<0.6	<0.5	<0.8	<0.7
$kT_{\rm ISM}$ [keV]	0.30±0.02	0.30±0.02	$0.22^{+0.03}_{-0.02}$	$0.22^{+0.01}_{-0.02}$	$0.22^{+0.03}_{-0.07}$	$0.22^{+0.03}_{-0.22}$
O [$Z_{\odot}$]	$0.50^{+1.51}_{-0.24}$	$0.50^{+0.21}_{-0.19}$	$0.51^{+0.34}_{-0.18}$	$0.51^{+0.17}_{-0.14}$	$0.52^{+0.37}_{-0.20}$	$0.52^{+0.18}_{-0.12}$
Ne [$Z_{\odot}$]	$0.69^{+2.00}_{-0.32}$	$0.69^{+0.16}_{-0.13}$	$0.94^{+0.86}_{-0.43}$	$0.94^{+0.30}_{-0.29}$	$0.94^{+1.16}_{-0.50}$	$0.94^{+0.38}_{-0.37}$
Mg, Al [$Z_{\odot}$]	$1.2^{+2.1}_{-0.61}$	$1.2^{+0.35}_{-0.32}$	$1.4^{+1.3}_{-0.7}$	$1.4^{+0.39}_{-0.42}$	$1.6^{+2.2}_{-0.8}$	1.6±0.5
Si, S, Ar, Ca [$Z_{\odot}$]	$1.2^{+6.8}_{-1.1}$	$1.2^{+0.41}_{-0.37}$	$1.4^{+2.1}_{-0.8}$	$1.4^{+0.85}_{-0.69}$	$1.6^{+2.6}_{-1.0}$	$1.6^{+0.9}_{-0.7}$
Fe, Ni [$Z_{\odot}$]	$0.26^{+0.74}_{-0.12}$	0.26 (fix)	$0.35^{+0.29}_{-0.14}$	0.35 (fix)	$0.40^{+0.48}_{-0.19}$	0.40 (fix)
$Norm_{\rm ISM}{}^{*}/f$	41^{+33}_{-30}	41^{+12}_{-7}	32^{+42}_{-13}	32^{+28}_{-8}	32^{+58}_{-32}	32^{+51}_{-32}
$kT_{\rm ISM2}$ [keV]			$0.61^{+0.22}_{-0.09}$	$0.61^{+0.18}_{-0.09}$	$0.59^{+0.19}_{-0.59}$	$0.59^{+0.19}_{-0.59}$
$Norm_{\rm ISM2}{}^{*}/f$			$10^{+6.3}_{-4.9}$	$10^{+3.9}_{-3.0}$	$7.4^{+11.2}_{-7.4}$	$7.4^{+4.2}_{-7.4}$
$kT_{\rm ISM3}$ [keV]					$0.94^{+64}_{-0.94}$	$0.94^{+64}_{-0.94}$
$Norm_{\rm ISM3}{}^{*}/f$					$1.7^{+17.8}_{-1.7}$	$1.7^{+7.5}_{-1.7}$
O/Fe*	$1.9^{+12.5}_{-1.7}$	$1.9^{+0.7}_{-0.5}$	$1.5^{+2.6}_{-1.0}$	$1.5^{+0.5}_{-0.4}$	$1.3^{+2.9}_{-0.9}$	$1.3^{+0.5}_{-0.4}$
Ne/Fe*	$2.6^{+16.6}_{-2.3}$	$2.6^{+0.6}_{-0.5}$	$2.7^{+6.0}_{-1.9}$	$2.7^{+0.9}_{-0.8}$	$2.3^{+7.4}_{-1.8}$	2.3±1.1
Mg/Fe*	$4.7^{+19.1}_{-4.1}$	$4.7^{+1.6}_{-1.4}$	$3.9^{+8.8}_{-2.8}$	$3.9^{+1.1}_{-1.2}$	$3.8^{+13.4}_{-3.0}$	$3.8^{+1.3}_{-1.2}$
Si/Fe*	$1.9^{+52.5}_{-4.6}$	$4.6^{+3.5}_{-3.0}$	$4.2^{+13.1}_{-3.2}$	$4.2^{+2.4}_{-2.0}$	$4.0^{+15.4}_{-3.3}$	$4.0^{+2.5}_{-1.9}$
$kT_{\rm LMXB}$ [keV]	10.0 (fix)	←	←	←	←	←
$Norm_{\rm LMXB}{}^{\ddagger}/f$ ($\times10^{-3}$)	1.2±0.1	1.2±0.1	1.1±0.1	1.1±0.1	$1.1^{+0.1}_{-0.8}$	$1.1^{+0.1}_{-0.9}$
$\chi^2/d.o.f$	438/367	438/368	415/365	415/366	414/363	414/364

* Normalization of the *apec* model divided by a solid angle Ω, assumed in a uniform-sky ARF calculation (20' radius), i.e. $Norm = (1/\Omega)\int n_e n_H\, dV/(4\pi(1+z)^2)D_A^2)$ cm^{-5} sr^{-1} in unit of 10^{-14}, where D_A is the angular diameter distance.

† Surface brightness of the $power-law$ model in the unit of photons s^{-1} cm^{-2} sr^{-1} keV^{-1} at 1 keV.

‡ i.e. $Norm = \int n_e n_H\, dV/(4\pi D^2)$ cm^{-5} sr^{-1} in the unit of 3.02×10^{-15}, where D is the distance to the source.

* Abundance ratios of [Z/Fe] to solar ratios of $[{\rm Z/Fe}]_{\odot}$.

7.1.4 Physical parameters in the halo region

We extracted physical parameters in the halo region as is the case of previous sections for the two-temperature model as indicated in Table 7.2. We assumed a spherical shape with a radius of 13.8′ corresponding to a radius of the optical disk and calculated a volume of the halo region to 9.4×10^{67} [cm^3]. Resultant parameters are shown in Table 7.3. As a typical distance from the nuclear region to the halo region, we adopted 6.9×10^3 [pc] which indicated a distance from the nuclear region to the middle point in the extracted halo region.

Table 7.3 Physical parameters for the two-temperature model in the halo region

Parameters \ Plasma	ISM1	ISM2
kT [keV]	$0.22^{+0.03}_{-0.02}$	$0.61^{+0.22}_{-0.09}$
L^* [10^{38} erg s^{-1}]	$3.8^{+2.4}_{-0.5}$	$2.3^{+1.0}_{-0.7}$
n_H [$f^{-1/2}$ 10^{-4} cm^{-3}]	$6.5^{+7.4}_{-4.1}$	$3.7^{+2.9}_{-2.5}$
P/k [$f^{-1/2}$ 10^3 K cm^{-3}]	$1.7^{+2.4}_{-1.1}$	$2.6^{+3.7}_{-1.9}$
E_{th}† [$f^{1/2}$ 10^{55} erg]	$3.3^{+1.2}_{-0.9}$	$5.0^{+3.7}_{-1.9}$
t_{cool}‡ [$f^{1/2}$ 10^3 Myr]	$1.4^{+3.0}_{-0.8}$	$11.5^{+37.1}_{-6.0}$

* Unabsorbed luminosity in 0.5–10.0 keV assuming the distance to 3.4 [Mpc].

† Thermal energy.

‡ Radiative cooling time using 3 kT / Λn_e.

7.2 Investigating the hardness maps and profiles

7.2.1 Hardness ratio map

In this section, a more detailed spatial structure is investigated by a hardness ratio map, which indicates the temperature distribution in the halo. A hardness ratio map is simple and useful a probe to trace the temperature change unless other factors such as an absorption gradient and a multi-temperature plasma make it harder or softer apparently.

In the halo region, the absorption gradient is relatively small and indeed the hard-

ness map is created in Bauer et al. (2008). However, a combination of a higher sensitivity in the soft energy band below 1 keV and a lower background level by *Suzaku* allows us to show a better quality map.

Firstly, we prepare *Suzaku* images in both 0.4–0.8 keV and 0.8–1.0 keV bands with a binning factor of 50 corresponding to 52″ per 1 bin. We select these energy bands because a shape of the soft thermal plasma around 0.2 keV become sensitive to its temperature and almost the same number of X-ray photons are detected. We estimated the intensity of foreground XRB emission using the result of the OFFSET region, and the NXB backgrounds from the dark Earth data. Using simulators *xisnxbgen* and *xissim*, large number of photons corresponding to 10 Msec for NXB and 1.6 Msec for XRB are accumulated to make a smooth background image. The hardness ratio map is made after the estimated background subtraction. We remove pixels with a negative value which fails to infer the correct background after background subtraction and these pixels are exhibited with white color.

Resultant hardness map is shown in Figure 7.8. In the hardness map, the disk region is harder than the other places such as the halo region except for edge regions of the detector and gradually the hardness value becomes smaller along with the minor axis of the disk. However, this is not real but mainly caused by the absorption gradient. This trend is consistent with the obtained by Bauer et al. (2008). Generally to utilize edge regions of the detector in image analysis seems to be dangerous, because to estimate an effective area and a sensitivity of these pixels is difficult which gives rise to significant under/overestimate of a background evaluation between a simulator and genuine edge pixels.

7.2.2 The surface brightness and hardness ratio profile

As a next step, we extract hardness profiles with error bars to discuss the temperature distribution more quantitatively. In this analysis, we derive projected surface brightness profiles from each H1, H2, H3 and H4 region and the integrated regions, i.e., a sum of H1, H2, H3 and H4 as shown in Figure 7.4, along with a minor axis perpendicular to the disk. We estimate the background level using the OFFSET region and subtract them from each profile with the statistical error. The background count in most bins is less than 20 % compared to the total count.

Obtained surface brightness profiles for H1, H2, H3 and H4 are shown in Figure 7.9. There are sharp peaks associated with the disk, and flat extents of the halo in all regions. Surface brightness profiles of spiral galaxies along with a minor axis perpendicular to the disk in X-rays are represented well by an exponential func-

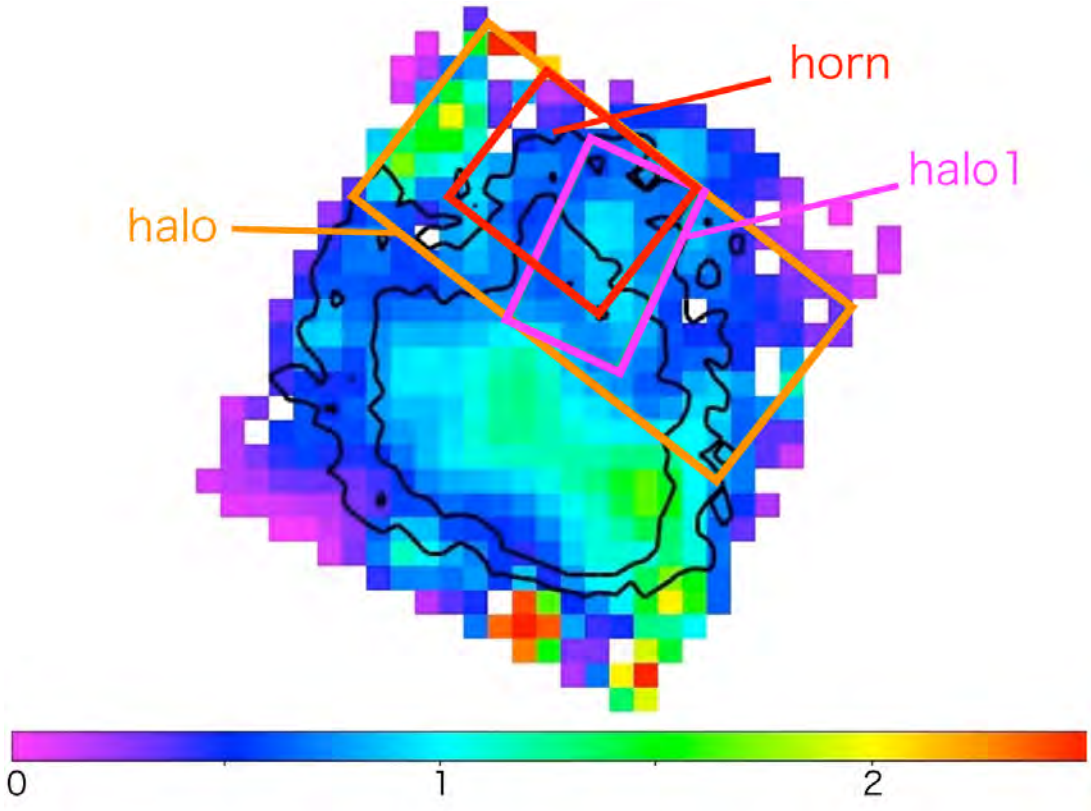

Figure 7.8 Hardness map of 0.8–1.0 keV to 0.4–0.8 keV by *Suzaku* with the binning factor of 50 corresponding to 52″. The expected counts from the NXB and foreground emission are subtracted. The map is smoothed to pick up a structure of the emission in the halo region with a kernel of $\sigma = 104''$ which is almost the same as the *Suzaku* angular resolution. Orange, red and magenta rectangles indicate the extracted region for spectral analysis. Black-color contours obtained in the 0.4–1.0 keV band are shown together to emphasize the horn structure in the halo region.

tion empirically (Strickland et al., 2004; Yamasaki et al., 2009). This structure can be confirmed in resultant surface brightness profiles regardless of smoothed surface brightnesses caused by the large angular resolution.

Then the hardness profiles are shown in Figure 7.10. A hardness value become smaller with increasing distance from the disk plane until the halo region. This trend is consistent with the obtained by the hardness map. However, hardness values seem to be roughly constant in the halo region within the statistical error, which suggests that no significant temperature change is found in the halo region. We convert the hardness value to corresponding temperature assuming an absorbed single thermal plasma and plot them for comparison in Figure 7.10 as magenta lines. The column density of 1×10^{20} cm^{-2} is also adopted considering the case of no intrinsic

absorption by NGC 253. Column densities for intrinsic absorption of 5×10^{20} cm^{-2} and 10×10^{20} cm^{-2} are adopted considering upper limits of our spectral analysis as shown in Table 7.2 and the radio observation (Koribalski et al., 1995). Corresponding temperature is 0.26–0.50 keV, 0.24–0.45 keV and 0.22–0.35 keV for cases of (1, 5 and 10)$\times10^{20}$ cm^{-2}, respectively, and this is consistent with the obtained temperature by spectral analysis (see Table 7.2 and 7.4) Thus, it is suggested that temperature in the halo region is rather uniform. The temperature in the halo region above 2 kpc away from the disk is constant within 20 %. In total disk and halo area, the temperature is distributed between 0.2–0.5 keV. The multi-temperature plasma is represented by a two-temperature *apec* model, due to characteristic emission lines. Note that the temperature estimation is also affected by the significant absorption gradient or complex spectral shape, which may exist in the nuclear and the disk regions.

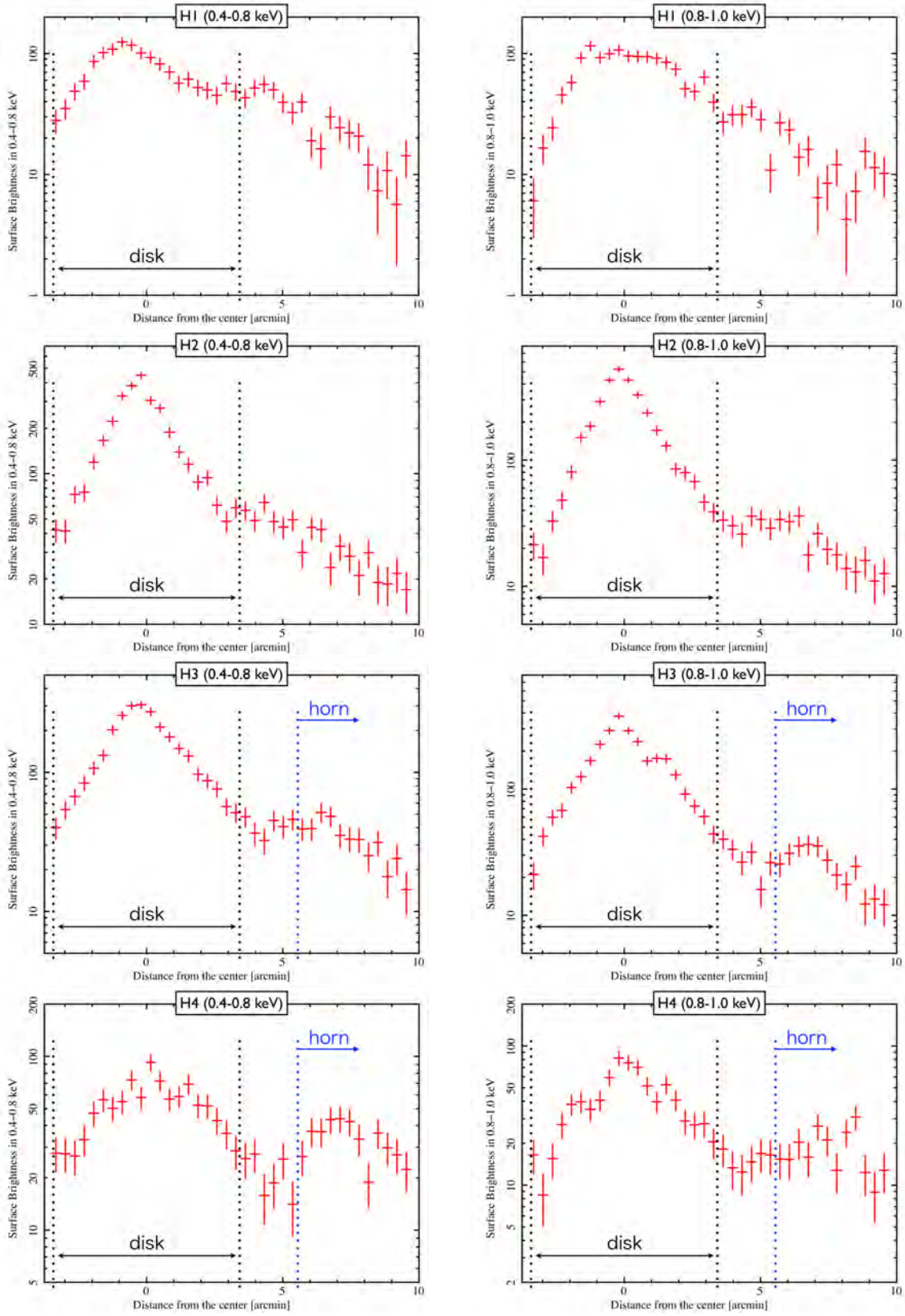

Figure 7.9 Surface brightness profiles in 0.4–0.8 keV (left) and 0.8–1.0 keV (right) for H1 to H4 defined in Figure 7.4. Black and blue dashed lines in each profile show a range of the disk region and the horn region defined for spectral analysis.

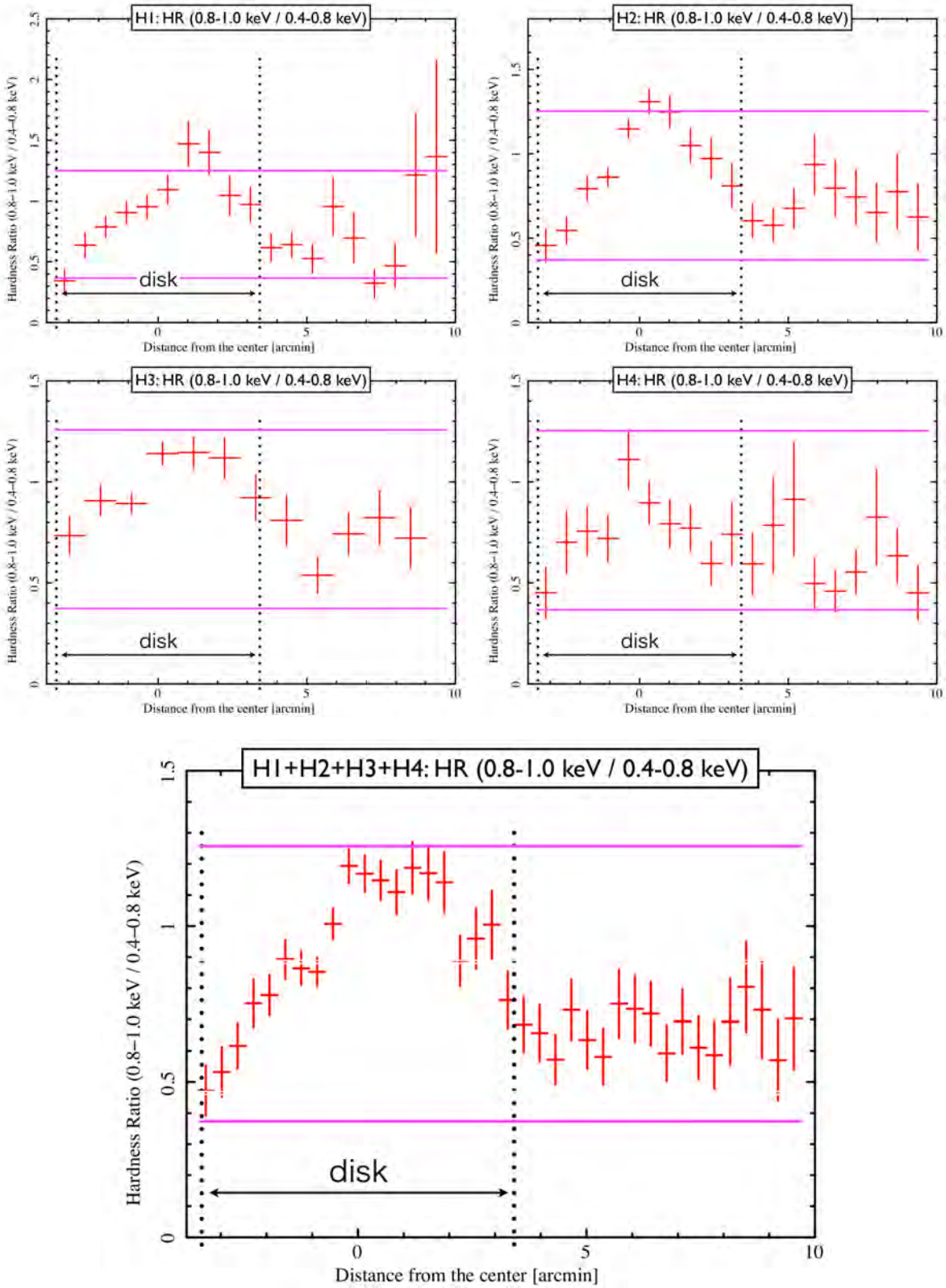

Figure 7.10 Hardness map of 0.8–1.0 keV to 0.4–0.8 keV for H1, H2, H3 and H4 regions and the integrated region (H1 + H2 + H3 + H4). Two magenta lines indicate corresponding temperatures of 0.2 and 0.6 keV for the one-temperature model with with $5{\times}10^{20}$ cm^2.

7.3 Energy spectra for selected regions

We selected several regions, from the harness map and surface brightness profile, to investigate the spectral feature and non-uniformity of the halo. First we conduct spectral analysis of an interesting region denoted as halo1 in Figure 7.8 which has a higher hardness ratio and seems to be diffuse. Then, resultant spectra and the best fit parameters for the halo1 and the halo excluding halo1 are shown in Figure 7.11 and Table 7.4. As a result, for both regions, one- or two-temperature models seems to be preferable statistically because after adding the third temperature plasma the goodness of fit does not improve at all or gets worse. For both cases, resulting temperatures are consistent with the statistical errors between the halo1 and the halo excluding halo1 regions. Despite a rough estimate in the sense that no error bars are taken into account, it is suggested that temperature in the halo region are uniform in an arcmin scale corresponding to a kpc scale.

A characteristic structure in the surface brightness profile is a bump-like profiles in H3 and H4 regions (see profiles of H3 in 0.8–1.0 keV and H4 in 0.4–0.8 keV). This structure can be seen predominantly in both H3 and H4 almost outside 5.5 arcmin (= 5.3 kpc) away from the disk plane. This feature is reported by Pietsch et al. (2000). This excess component can be confirmed in all regions of both energy bands and interpreted caused by the emission from ISM in the halo region. This bump-like structure can be characterized by not only X-ray but also other observations in different wavelengths such as radio and IR (e.g. Boomsma et al., 2005; Kaneda et al., 2009). Boomsma et al. (2005) argue that the observed H I plume was dragged up from the disk due to the outflow and the head of this H I plume corresponds to this bump-like region. In Kaneda et al. (2009), dust temperature of this area is higher significantly based on the hardness map compared to other regions in the halo caused by a shock heating through interaction between the X-ray outflow and pre-existing HI halo clouds. Therefore, to pursue the origin of this horn region whether this region can be considered as a part of the static halo or the outflow is very scientifically interesting and important to draw a picture of the outflow phenomenon.

We extract spectra from this region ($5.7' \times 6.8' = 5.5 \times 6.5$ kpc^2) based on the observed surface brightnesses in H3 and H4 (see Figure 7.8, hereafter the horn region) and spectral analysis is carried out. Resultant spectra, abundance ratios and the best fit parameters are shown in Figures 7.12 and 7.13 and Table 7.5. We also confirm the consistency between abundance ratios for fixing the Fe abundance to 0.1, 0.42 and 1 $Z_\odot$ (see Figure 7.13 bottom). For both regions, the two-temperature model seems to

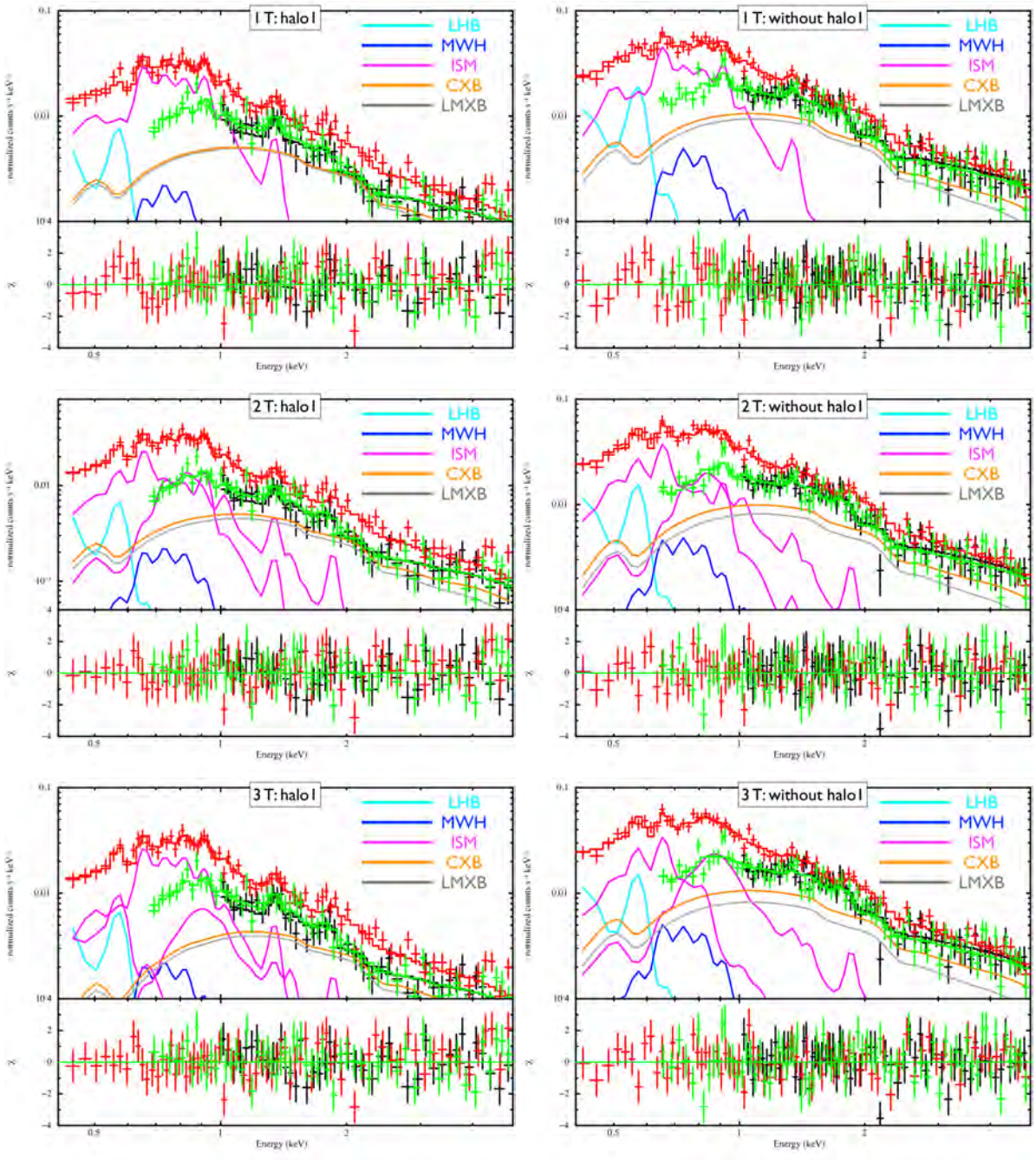

Figure 7.11 *Suzaku* spectra at the energy range between 0.5 and 5.0 keV in the halo1 (left) and the halo region excluding halo1 (right). The lines show the best-fit model that consists of $apec_{\rm LHB}$ (cyan), *phabs*× $apec_{\rm MWH}$ (blue), *phabs*×$phabs_{\rm Galactic}$ *zbremss* + *power-law* (gray and orange) and *phabs*×$phabs_{\rm Galactic}$ $apec_{\rm ISM}$ (magenta). As the ISM component, 1 T (top), 2 T (middle) and 3 T (bottom) thin thermal plasmas are adopted, respectively. A Fe abundance in the ISM component is linked to each other.

be favorable since the abundance ratio Si/Fe in the one-temperature model is too high to be acceptable and the lowest temperature in the three-temperature model cannot be distinguished from the middle temperature plasma. Resultant temperatures be-

Table 7.4 Best fit parameters for the halo1 and the whole halo region excluding halo1 by *Suzaku*.

Region	halo1			without halo1		
Model	$1T$	$2T$	$3T$	$1T$	$2T$	$3T$
f (XIS1)	$1.28^{+0.10}_{-0.09}$	$1.27^{+0.10}_{-0.09}$	$1.26^{+0.10}_{-0.09}$	$1.06^{+0.06}_{-0.05}$	$1.05^{+0.06}_{-0.05}$	1.06±0.05
f (XIS3)	0.89±0.07	0.89±0.07	0.88±0.07	0.86±0.05	0.85±0.05	0.84±0.04
$kT_{\rm LHB}$ [keV]	0.07±0.02	$0.07^{+0.02}_{-0.01}$	$0.07^{+0.02}_{-0.01}$	0.08±0.01	0.07±0.02	0.07±0.02
$Norm_{\rm LHB}{}^{*}/f$	155^{+487}_{-100}	228^{+953}_{-165}	227^{+968}_{-165}	98^{+168}_{-50}	190^{+757}_{-134}	190^{+705}_{-132}
$kT_{\rm MWH}$ [keV]	$0.31^{+0.12}_{-0.07}$	$0.29^{+0.10}_{-0.06}$	$0.29^{+0.10}_{-0.06}$	$0.33^{+0.34}_{-0.09}$	$0.29^{+0.10}_{-0.06}$	$0.28^{+0.08}_{-0.05}$
$Norm_{\rm MWH}{}^{*}/f$	$1.5^{+1.0}_{-0.7}$	$1.7^{+0.9}_{-0.8}$	$1.7^{+1.0}_{-0.7}$	$1.3^{+0.9}_{-0.8}$	$1.7^{+1.1}_{-0.7}$	$1.8^{+0.6}_{-0.7}$
Γ (fix)	1.4 (fix)	←	←	←	←	←
$SB^{\dagger}$	8.7±0.3	8.7±0.3	8.7±0.3	8.7±0.3	8.7±0.3	8.7±0.3
$zphabs$ ($\times 10^{21}$ [cm^{-1}])	<1.1	<1.2	<2.9	<0.5	<1.3	<0.9
$kT_{\rm ISM}$ [keV]	0.31±0.02	0.23±0.04	$0.11^{+0.03}_{-0.02}$	0.29±0.03	$0.21^{+0.04}_{-0.02}$	$0.08^{+1.8}_{-0.08}$
O [$Z_{\odot}$]	$0.70^{+125}_{-0.44}$	$0.61^{+1.49}_{-0.32}$	$0.67^{+0.34}_{-0.18}$	$0.24^{+0.46}_{-0.07}$	$0.38^{+0.34}_{-0.15}$	$0.43^{+0.29}_{-0.13}$
Ne [$Z_{\odot}$]	$1.0^{+63}_{-0.62}$	$1.2^{+3.4}_{-0.9}$	$0.67^{+0.86}_{-0.43}$	$0.36^{+0.58}_{-0.17}$	$0.58^{+0.62}_{-0.35}$	<0.01
Mg, Al [$Z_{\odot}$]	$1.9^{+158}_{-1.2}$	$2.0^{+3.3}_{-1.3}$	$1.6^{+1.3}_{-0.7}$	$0.55^{+0.85}_{-0.32}$	$0.63^{+1.0}_{-0.41}$	$0.50^{+0.97}_{-0.42}$
Si, S, Ar, Ca [$Z_{\odot}$]	$2.1^{+968}_{-2.1}$	$1.9^{+5.5}_{-1.2}$	$1.5^{+2.1}_{-0.8}$	<2.2	$0.76^{+1.5}_{-0.57}$	$0.64^{+0.92}_{-0.46}$
Fe, Ni [$Z_{\odot}$]	$0.37^{+28}_{-0.22}$	$0.43^{+1.13}_{-0.25}$	$0.43^{+0.29}_{-0.14}$	$0.12^{+0.18}_{-0.04}$	$0.21^{+0.24}_{-0.09}$	$0.27^{+0.28}_{-0.10}$
$Norm_{\rm ISM}{}^{*}/f$	39^{+55}_{-39}	34^{+126}_{-21}	109^{+3294}_{-107}	67^{+20}_{-40}	51^{+114}_{-30}	838^{+1538}_{-838}
$kT_{\rm ISM2}$ [keV]		$0.59^{+0.50}_{-0.15}$	$0.29^{+0.22}_{-0.09}$		$0.62^{+0.19}_{-0.12}$	0.21±0.02
$Norm_{\rm ISM2}{}^{*}/f$		12^{+23}_{-9}	56^{+259}_{-56}		17^{+19}_{-10}	34^{+66}_{-15}
$kT_{\rm ISM3}$ [keV]			$0.84^{+0.22}_{-0.09}$			$0.79^{+0.08}_{-0.07}$
$Norm_{\rm ISM3}{}^{*}/f$			$8.6^{+15.1}_{-6.6}$			15^{+15}_{-8}
O/Fe*	$1.9^{+882}_{-1.9}$	$1.4^{+10.5}_{-1.2}$	$1.6^{+260}_{-1.5}$	$2.0^{+7.2}_{-1.5}$	$1.8^{+4.1}_{-1.3}$	$1.6^{+2.6}_{-1.0}$
Ne/Fe*	$2.8^{+450}_{-2.8}$	$2.8^{+23.5}_{-2.6}$	$1.6^{+170}_{-1.6}$	$3.1^{+9.4}_{-2.4}$	$2.8^{+7.2}_{-2.2}$	<0.06
Mg/Fe*	$5.2^{+1120}_{-5.2}$	$4.7^{+25.2}_{-4.2}$	$3.9^{+78}_{-3.8}$	$4.6^{+13.9}_{-3.8}$	$3.0^{+10.8}_{-2.5}$	$1.8^{+6.7}_{-1.7}$
Si/Fe*	$5.7^{+6840}_{-5.7}$	$4.5^{+37.6}_{-4.1}$	$3.6^{+704}_{-3.5}$	$0.3^{+29.5}_{-0.3}$	$3.6^{+15.2}_{-3.2}$	$2.4^{+6.7}_{-2.0}$
$kT_{\rm LMXB}$ [keV]	10.0 (fix)	←	←	←	←	←
$Norm_{\rm LMXB}{}^{\ddagger}/f$ ($\times 10^{-3}$)	$1.3^{+0.2}_{-0.1}$	$1.2^{+0.2}_{-0.1}$	1.2±0.1	1.2±0.1	1.1±0.1	1.0±0.1
$\chi^2/d.o.f$	371/336	359/334	358/332	439/373	422/371	428/369

* Normalization of the *apec* model divided by a solid angle Ω, assumed in a uniform-sky ARF calculation (20' radius), i.e. $Norm = (1/\Omega)\int n_e n_H\, dV/(4\pi(1+z)^2)D_A^2)$ cm^{-5} sr^{-1} in unit of 10^{-14}, where D_A is the angular diameter distance.
† Surface brightness of the $power-law$ model in the unit of photons s^{-1} cm^{-2} sr^{-1} keV^{-1} at 1 keV.
‡ i.e. $Norm = \int n_e n_H dV/(4\pi D^2)$ cm^{-5} sr^{-1} in the unit of 3.02×10^{-15}, where D is the distance to the source.
* Abundance ratios of [Z/Fe] to solar ratios of $[{\rm Z/Fe}]_{\odot}$.

tween both regions and abundance ratios of every 4 element are consistent with each other to within the statistical error.

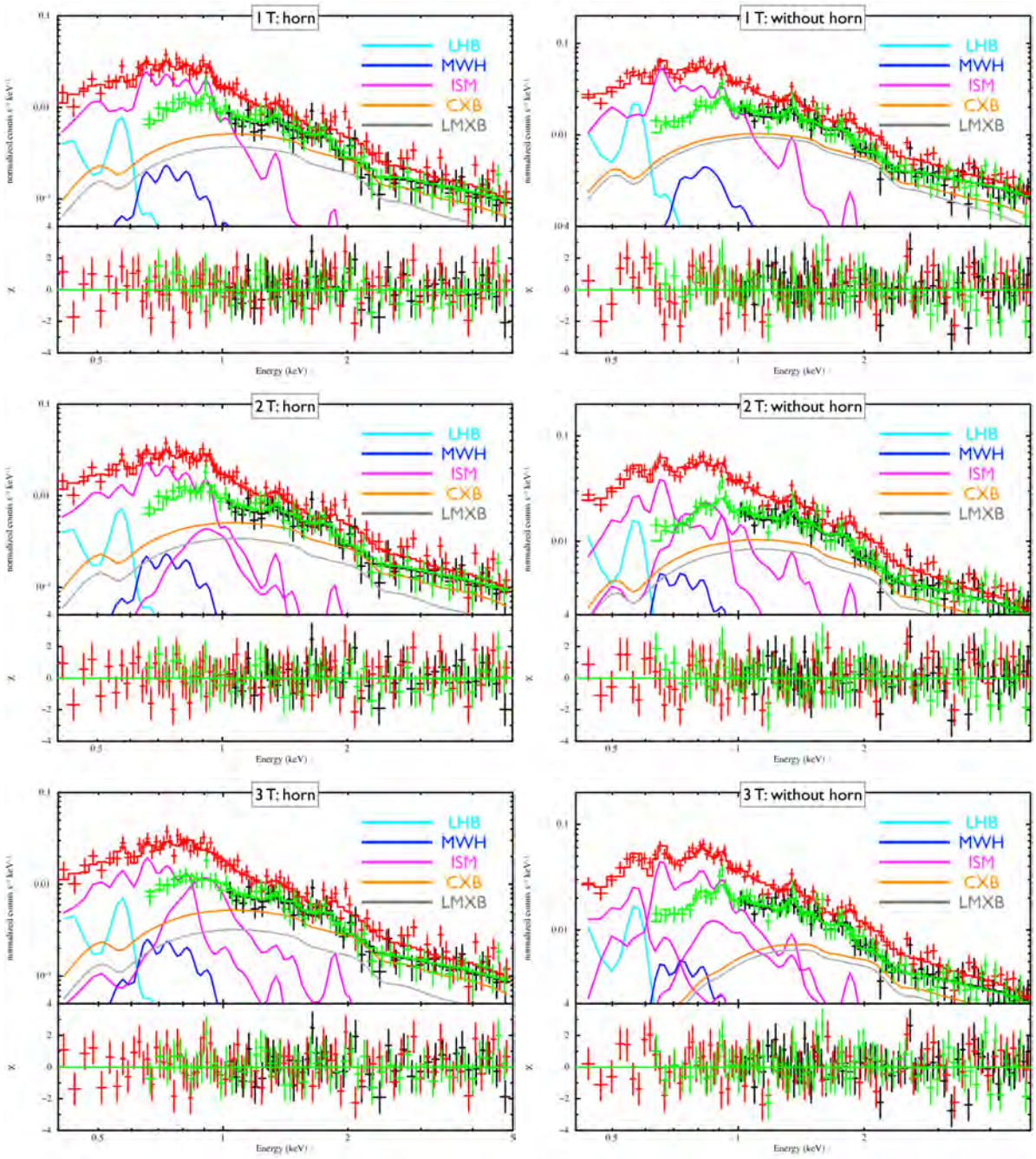

Figure 7.12 The same as Figure 7.11 but in the horn (left) and the halo region excluding the horn region (right).

Table 7.5 Best fit parameters for the horn region and the whole halo region excluding horn by *Suzaku*.

Region	horn			without horn		
Model	$1T$	$2T$	$3T$	$1T$	$2T$	$3T$
f (XIS1)	$1.13^{+0.09}_{-0.08}$	1.12±0.09	1.15±0.09	1.17±0.06	1.15±0.06	1.18±0.06
f (XIS3)	$0.92^{+0.08}_{-0.07}$	$0.91^{+0.08}_{-0.07}$	$0.90^{+0.08}_{-0.07}$	0.93±0.05	0.92±0.05	0.90±0.05
$kT_{\rm LHB}$ [keV]	0.07±0.02	0.07±0.02	$0.07^{+0.02}_{-0.01}$	$0.09^{+0.02}_{-0.01}$	$0.07^{+0.02}_{-0.01}$	$0.07^{+0.02}_{-0.01}$
$Norm_{\rm LHB}{}^{*}/f$	175^{+135}_{-587}	208^{+872}_{-155}	241^{+605}_{-176}	85^{+184}_{-34}	275^{+963}_{-203}	226^{+923}_{-164}
$kT_{\rm MWH}$ [keV]	$0.30^{+0.10}_{-0.06}$	$0.29^{+0.10}_{-0.06}$	$0.27^{+0.07}_{-0.05}$	$0.63^{+0.12}_{-0.43}$	$0.28^{+0.10}_{-0.06}$	$0.29^{+0.10}_{-0.06}$
$Norm_{\rm MWH}{}^{*}/f$	$1.6^{+0.8}_{-0.7}$	$1.8^{+1.1}_{-0.7}$	$1.9^{+1.0}_{-0.7}$	0.76±0.26	$1.8^{+1.1}_{-0.8}$	$1.7^{+1.0}_{-0.7}$
Γ (fix)	1.4 (fix)	←	←	←	←	←
$SB^{\dagger}$	8.7±0.3	8.7±0.3	8.7±0.3	8.6±0.3	8.7±0.3	8.7±0.3
$zphabs$ ($\times 10^{21}$ [cm^{-1}])	<0.5	<0.9	<0.7	<1.4	<1.6	$2.9^{+0.6}_{-0.7}$
$kT_{\rm ISM}$ [keV]	$0.29^{+0.03}_{-0.05}$	0.24±0.04	$0.09^{+0.18}_{-0.09}$	$0.32^{+0.06}_{-0.03}$	$0.21^{+0.04}_{-0.03}$	$0.09^{+0.02}_{-0.09}$
O [$Z_{\odot}$]	$0.29^{+1.16}_{-0.16}$	$0.31^{+0.78}_{-0.15}$	$0.24^{+0.19}_{-0.09}$	$0.44^{+6.29}_{-0.22}$	$0.36^{+0.35}_{-0.14}$	$0.44^{+0.20}_{-0.15}$
Ne [$Z_{\odot}$]	$0.54^{+1.81}_{-0.28}$	$0.62^{+1.66}_{-0.34}$	<0.02	$0.47^{+7.9}_{-0.28}$	$0.56^{+0.77}_{-0.29}$	$0.26^{+0.13}_{-0.09}$
Mg, Al [$Z_{\odot}$]	$0.71^{+1.73}_{-0.59}$	$1.2^{+4.0}_{-0.9}$	$0.80^{+1.21}_{-0.70}$	$0.80^{+4.55}_{-0.51}$	$0.81^{+1.25}_{-0.45}$	$0.42^{+0.29}_{-0.19}$
Si, S, Ar, Ca [$Z_{\odot}$]	$1.6^{+17.4}_{-1.5}$	$2.0^{+8.1}_{-1.6}$	$1.2^{+1.4}_{-0.8}$	$1.4^{+9.5}_{-1.1}$	$0.86^{+1.59}_{-0.55}$	$0.47^{+0.37}_{-0.25}$
Fe, Ni [$Z_{\odot}$]	$0.24^{+1.54}_{-0.12}$	$0.42^{+1.06}_{-0.25}$	$0.42^{+0.28}_{-0.22}$	$0.15^{+1.19}_{-0.08}$	$0.19^{+0.22}_{-0.08}$	$0.17^{+0.10}_{-0.06}$
$Norm_{\rm ISM}{}^{*}/f$	63^{+67}_{-55}	57^{+109}_{-39}	2204^{+6392}_{-2197}	55^{+145}_{-51}	51^{+164}_{-31}	7616^{+3854}_{-9121}
$kT_{\rm ISM2}$ [keV]		$0.91^{+0.50}_{-0.15}$	$0.22^{+0.04}_{-0.02}$		$0.63^{+0.14}_{-0.09}$	$0.27^{+0.03}_{-0.05}$
$Norm_{\rm ISM2}{}^{*}/f$		$4.3^{+8.1}_{-3.1}$	64^{+57}_{-27}		20^{+26}_{-11}	201^{+152}_{-76}
$kT_{\rm ISM3}$ [keV]			$0.86^{+0.06}_{-0.10}$			$0.74^{+0.27}_{-0.22}$
$Norm_{\rm ISM3}{}^{*}/f$			11^{+9}_{-5}			30^{+44}_{-18}
O/Fe*	$1.2^{+10.8}_{-1.1}$	$0.75^{+5.67}_{-0.64}$	$0.58^{+1.64}_{-0.36}$	$2.9^{+100}_{-2.7}$	$1.9^{+4.4}_{-1.3}$	$2.6^{+3.4}_{-1.5}$
Ne/Fe*	$2.2^{+17.3}_{-2.1}$	$1.5^{+12.0}_{-1.3}$	<0.10	$3.1^{+125}_{-3.0}$	$2.9^{+8.9}_{-2.2}$	$1.6^{+2.2}_{-0.9}$
Mg/Fe*	$2.9^{+17.3}_{-2.8}$	$2.9^{+27.6}_{-2.7}$	$1.9^{+8.6}_{-1.8}$	$5.2^{+76.2}_{-5.0}$	$4.1^{+14}_{-3.3}$	$2.5^{+4.2}_{-1.6}$
Si/Fe*	$6.5^{+150}_{-6.4}$	$4.7^{+54.3}_{-4.4}$	$2.9^{+10.8}_{-2.4}$	$9.2^{+157}_{-9.0}$	$4.4^{+17.2}_{-3.7}$	$2.8^{+5.0}_{-2.0}$
$kT_{\rm LMXB}$ [keV]	10.0 (fix)	←	←	←	←	←
$Norm_{\rm LMXB}{}^{\ddagger}/f$ ($\times 10^{-3}$)						
$\chi^2/d.o.f$	349/347	345/345	351/343	433/383	412/381	406/379

* Normalization of the *apec* model divided by a solid angle Ω, assumed in a uniform-sky ARF calculation (20' radius), i.e. $Norm = (1/\Omega)\int n_e n_H\, dV/(4\pi(1+z)^2)D_A^2)$ cm^{-5} sr^{-1} in unit of 10^{-14}, where D_A is the angular diameter distance.

† Surface brightness of the $power-law$ model in the unit of photons s^{-1} cm^{-2} sr^{-1} keV^{-1} at 1 keV.

‡ i.e. $Norm = \int n_e n_H dV/(4\pi D^2)$ cm^{-5} sr^{-1} in the unit of 3.02×10^{-15}, where D is the distance to the source.

* Abundance ratios of [Z/Fe] to solar ratios of [Z/Fe]$_{\odot}$.

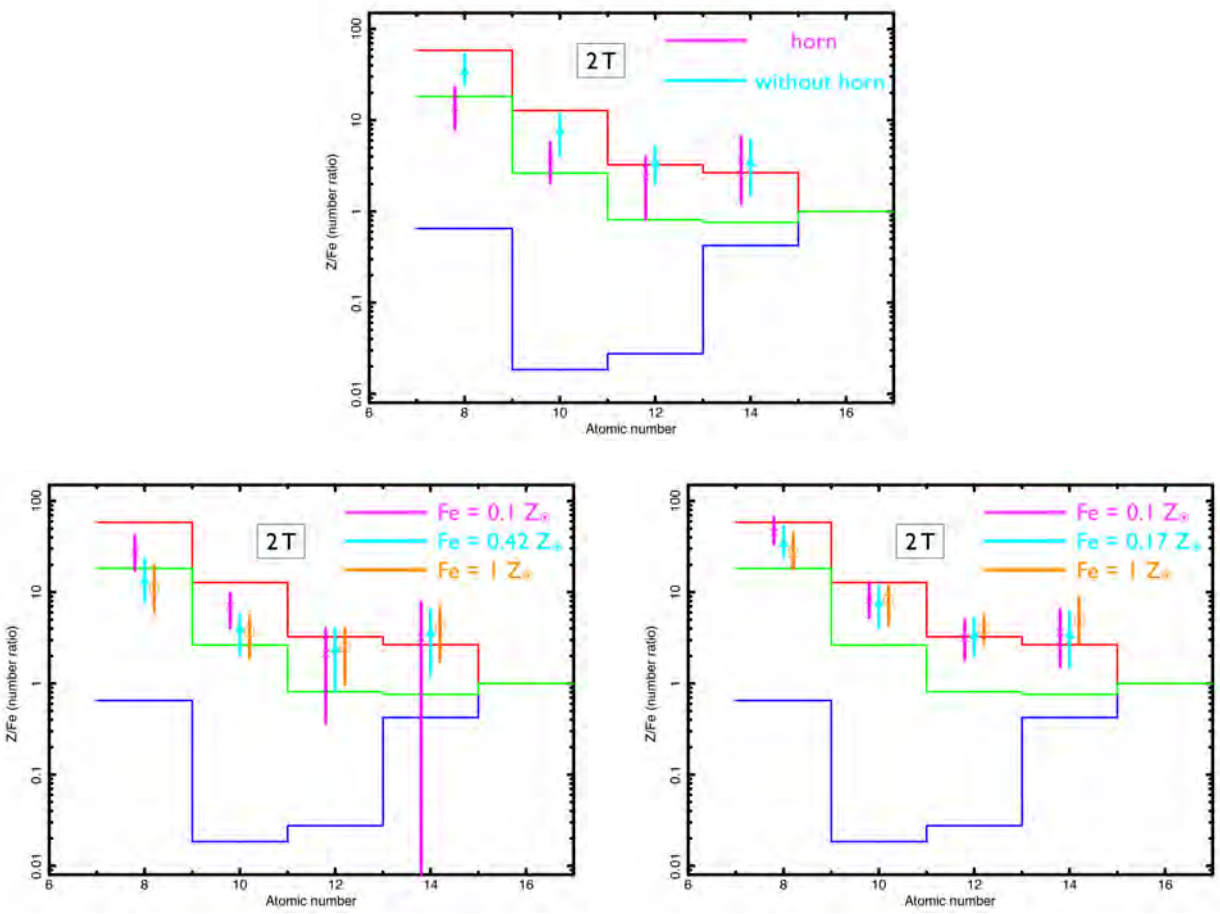

Figure 7.13 Abundance ratios of O, Ne, Mg, and Si to Fe for both horn and the other region in the halo (top). Bottom panels show results of abundance ratios fixing the Fe element to be 0.1, the best fit values as shown in Table 7.5 and 1 $Z_{\odot}$.

8 Discussion

In this section, we merge our results and discuss whether observed hot gas properties can confront inconsistency with the standard scenario of the starburst-driven outflows or not. To answer this question, we argue the following three points:

1. Can hot gas in the nuclear region be considered to be powered by type II supernovae ?
2. Can hot gas in the halo be considered to be the same origin as the inner regions from a view of the chemical composition ?
3. If anything the above idea is acceptable, can hot gas in the nuclear region reach out to 10 kpc away from the disk in the halo region dynamically ?

For the first question, we pursue the origin of observed hot gas in the nuclear region utilizing Fe I and F XXV emission lines. For the second, we compare resultant abundance patterns in three regions, i.e., the inner superwind, disk and halo regions. For the last question, we construct a simple model and inquire whether hot gas in the nuclear region can travel to the halo region or not and if anything can reach, we constrain the condition to reach within observed physical parameters.

8.1 Origin of the Emission in Nuclear

8.1.1 Possible contribution from point sources

CVs and active binaries are bright point sources that emit Fe lines with typical luminosities of $L_{2-10\ \mathrm{keV}} \sim 10^{31} - 10^{32}$ erg s^{-1} and $L_{2-10\ \mathrm{keV}} < 10^{31}$ erg s^{-1}, respectively. The luminosity in P1 corresponds to 10^{7-8} sources, or a number density of $\sim$100–1000 pc^{-3}. We can also estimate the number density from line flux of CVs which are relatively luminous compared to active binaries. The typical luminosity of the Fe I line is on the order of 10^{29-30} erg s^{-1} (Ezuka & Ishida, 1999), which leads to the large number 10^{7-8} sources and a number density of $\sim$500–5000 pc^{-3}. The number density of CVs and active binaries are both $10^{-5} - 10^{-4}$ pc^{-3} in the Galaxy (e.g. Rogel et al., 2008; Favata et al., 1995). Even at Galactic center, the expected number density of CVs is on the order of $10^{-2} - 10^{-1}$ pc^{-3}, assuming that their number density can be scaled from the stellar density (Muno et al., 2003). Therefore

the contribution of these point sources seems low. HMXBs are also one of candidates with typical luminosity of 10^{33-34} erg s^{-1} for Fe I fluorescent line (Torrejón et al., 2010). This corresponds to 10^{3-4} HMXBs or $10^{-2}-10^{-1}$ pc^{-3} in P1. Considering the number of HMXBs in the Galaxy (∼100), contribution of HMXBs also seems low, unless extreme number of HMXBs are produced by star forming activity, or population of undetected obscured HMXBs (Walter et al., 2006) is much larger.

8.1.2 Hot diffuse gas of SNR origin

Supernova remnants (SNRs) likely make the biggest contribution as a diffuse plasma. Considering the fact that the plasma temperature of a SNR decreases gradually with time, middle-age or young SNRs are mainly responsible for emitting ionized Fe lines. The luminosity and thermal energy of young or middle-aged SNRs in LMC are 10^{36-37} erg s^{-1} and 10^{51-52} erg, respectively (Hughes et al., 1998). Both the luminosity and thermal energy of the higher-temperature plasma of NGC 253 correspond to about 100–1000 and 10–100 young or middle-aged SNRs, respectively. We also estimated the number of SNRs using the observed Fe mass (20±2 $M_\odot$) and Fe mass ejection per one Type II SN (8.4×10^{-2} $M_\odot$; Iwamoto et al., 1999). The resultant number of SNRs is about 240±20 which is consistent with the estimated value by the luminosity. This suggests that the very dense massive star cluster in P1 exists, which is consistent with the results of the mid infrared observations.

8.1.3 Column density of molecular clouds

Molecular clouds that are irradiated by surrounding X-ray sources would emit a fluorescent Fe I line. We assume that the incident X-ray is photoelectrically absorbed by the molecular gas that subtends an angle $\Delta\Omega$ seen from the continuum source. The line flux of the Fe I K line can be estimated as

$$I_{6.4\ \mathrm{keV}} = \left(\frac{\Delta\Omega}{4\pi}\right)\epsilon\int_{7.1\ \mathrm{keV}}^{\infty} dE \int ds\ n_{\mathrm{Fe}}\sigma_{\mathrm{Fe}}(E)F(E), \tag{8.1}$$

where ϵ, n_{Fe}, $\sigma_{\mathrm{Fe}}(E)$ and $F(E)$ indicate the fluorescence yield of Fe I K line (ϵ = 0.34), the density of the molecular gas, the photoelectric cross section, and the X-ray source intensity, respectively. Assuming a thermal bremsstrahlung spectrum for the continuum source, the X-ray source intensity, $F(E) \propto \exp(-E/k_BT)$, can be determined in the 6.0–7.5 keV band. The Fe column density is written as $\int n_{\mathrm{Fe}}ds = Z_{\mathrm{Fe}}N_H$, where Z_{Fe} and N_H represent the elemental abundance of iron to hydrogen and the column density of the required molecular gas, respectively. The photoelectric cross

section of Fe above 7.1 keV is approximated as $\sigma_{\rm Fe}(E) = 3.8 \times 10^{-20}(E/7.1\ {\rm keV})^{-2.58}$ cm^2 as described in Nobukawa et al. (2008). Substituting these values, we obtain

$$N_H = (1.0^{+1.1}_{-0.8}) \times 10^{24} \left(\frac{\Omega}{2\pi}\right)^{-1}\ {\rm cm}^{-2}. \tag{8.2}$$

The solid angle $\Omega = 2\pi$ corresponds to the case that the X-ray sources are distributed entirely behind the molecular gas. This column density was consistent with the molecular clouds observed in the radio observation (Sakamoto et al., 2011) to within the statistical errors. Thus, the observed Fe I line flux is explained by the emission from the NGC 253 nucleus and the dense molecular clouds in the nuclear region.

8.2 Origin of the Hot Gas in Disk and Halo

In this section, we discuss the origin of the hot gas in disk and halo regions. Firstly, we plot abundance patterns of 4 elements, i.e., O, Ne, Mg and Si relative to Fe for the superwind, disk and halo regions together for comparison as shown in Figure 8.1. For each region, we adopt abundance patterns of the best fit model based on not necessarily the statistics but physically-accepted result. The two-temperature model in each region is adopted because the third temperature plasma is not required physically and also goodness of fit does not improve statistically and only one-temperature plasma can not cover all of the observed emission lines. As shown in Figure 8.1, one can find an interpretation straightforwardly that the hot gas in the halo region derive from the inner superwind furthermore inside the disk region since abundance patterns for every element match each other within the statistical errors. We include systematic error on abundance patterns as shown in §A.

8.3 Dynamics of the hot gas and the Possibility of the Outflow Toward the Outside of NGC 253

As discussed above, the hot gas in the halo region can be regarded as the inner superwind gas origin based on points of view of a chemical composition of the hot gas. In this section, we investigate a dynamics of the hot gas and finally discuss the possibility that the hot gas in the halo region can escape from the potential of NGC 253 or not in the future.

We focus on a temperature and density relationship which can provide us a hint of the hot gas dynamics. Figure 8.2 indicates a hardness profile in 0.8–1.0 keV to 0.4–0.8 keV and a surface brightness profiless in 0.4–0.8 keV obtained in H2 and H3 regions.

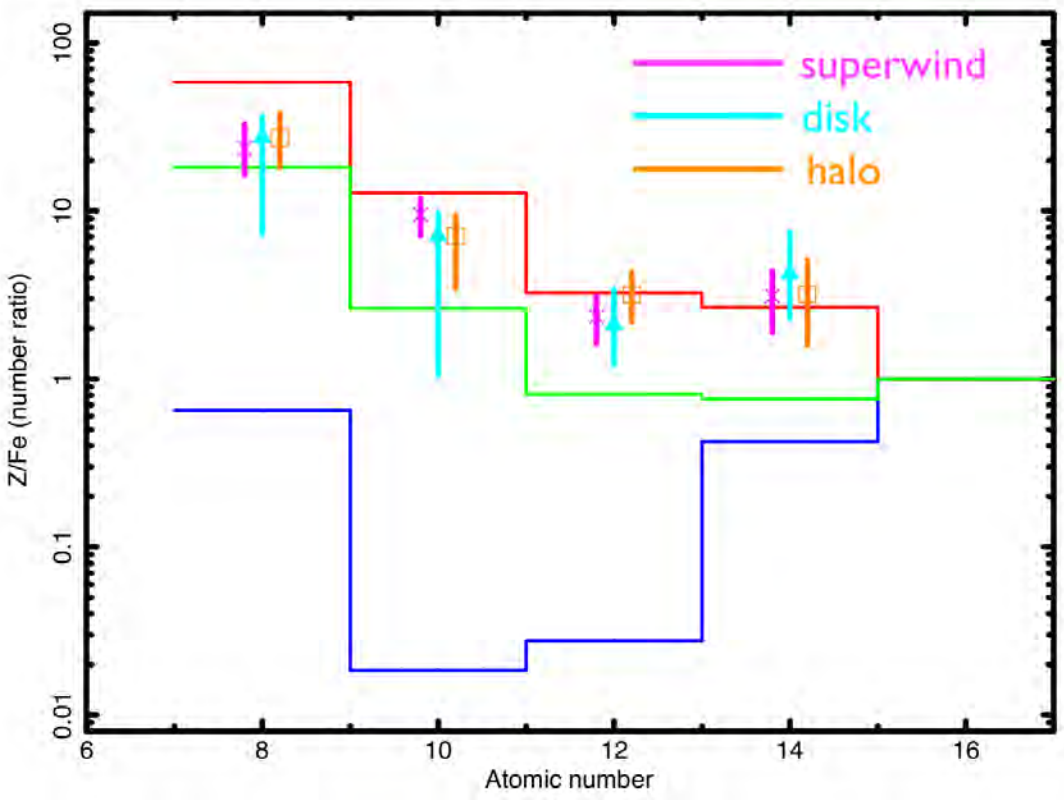

Figure 8.1 Abundance ratios of O, Ne, Mg, and Si to Fe for the superwind (magenta), disk (cyan) and halo (orange) regions, respectively.

The hardness ratio can converted to the temperature of ISM if one assume a model for a spectrum. As a simple model, we assume an absorbed ISM model because in this energy band, according to spectral fittings in the disk and the halo regions, ISM is considered to be dominant in spectral components. As a column density and an abundance pattern, we adopt 5×10^{20} cm^{-2} based on the radio observation of the H I distribution (Koribalski et al., 1995) and those of the obtained in the halo region. This column density corresponds to almost the boundary column density between the disk and the halo regions and the difference of abundance patterns between the disk and the halo is enough small compared to the statistical errors in this conversion process. We adopt a linear correlation between the hardness ratio and the temperature and the obtained data are represented well with a slope of 2.2±0.2 and a constant factor of -0.07±0.09. The expected temperature profile is shown in Figure 8.3 (left).

Next, we try to extract a physical parameter which directly reflects density of the hot gas. Thus, we focus on the surface brightness for H2 and H3 regions because if we assume that depth of the hot gas is the same the surface brightness is directly $\propto \Lambda(T)\ n^2$. As the emissivity denoted as $\Lambda\ (T)$, we adopt values in Sutherland

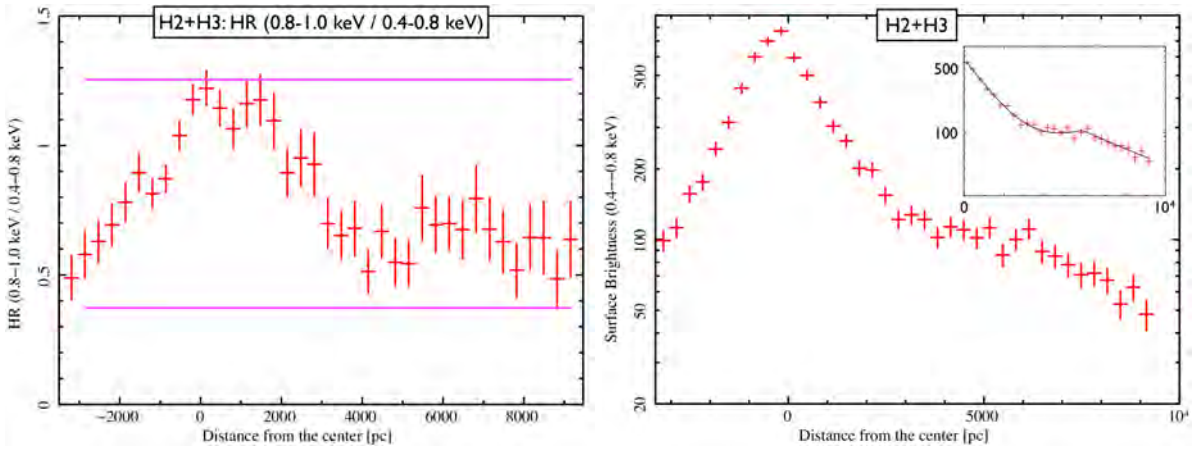

Figure 8.2 Hardness profile (left) and surface brightness profile in 0.4–0.8 keV (right) in H2 and H3. Two magenta lines indicate corresponding temperatures for the one-temperature model with a specific absorption column density. 0.2 keV and 0.6 keV with 5×10^{20} cm^2. The small panel in the right figure shows a close-up view of the disk to the halo fitted with the double exponential model.

& Dopita (1993) with the abundance of [Fe/H] = 0.5 which is nearly equal to the obtained in our analysis.

Finally, we plot the expected temperatures and the surface brightness together (see Figure 8.4). Black and green points indicates the north and the south halo, while the red is the halo. Compared to the halo region, in the disk region, it seems to be a correlation between the temperature and the surface brightness. Thus, we plot the known physical conditions of $\gamma = 4/3$ and $5/3$ corresponding to the radiation field and adiabatic expansion and also $\gamma = 6/3$ for a comparison. It is suggested that in both disk regions, an adiabatic expansion is allowable while in the halo region a free expansion is acceptable considering a decline of the surface brightness and a constant of the temperature. The abundance choice of [Fe/H] = 0.5 does not affect this result since not absolute but relative values of the emissivity between 0.2 keV and 0.6 keV are important in this analysis.

As a next step, to infer the possibility that the hot gas in the halo region can escape from the host galaxy, we try to constrain a velocity of the hot gas. Based on the result that the temperature of the hot gas in the halo region is nearly constant any cooling process do not work efficiently. We focus on this result and assume the following simple model. In our simple model, temperature of the hot gas cools only through a radiative cooling whose timescale is described as

$$t_{cool}\ (R,t)\ [\mathrm{s}] = \frac{kT}{n(R)\Lambda(T)} \tag{8.3}$$

where kT, $n(R)$ and $\Lambda(T)$ are temperature, the density of the hot gas and cooling rate

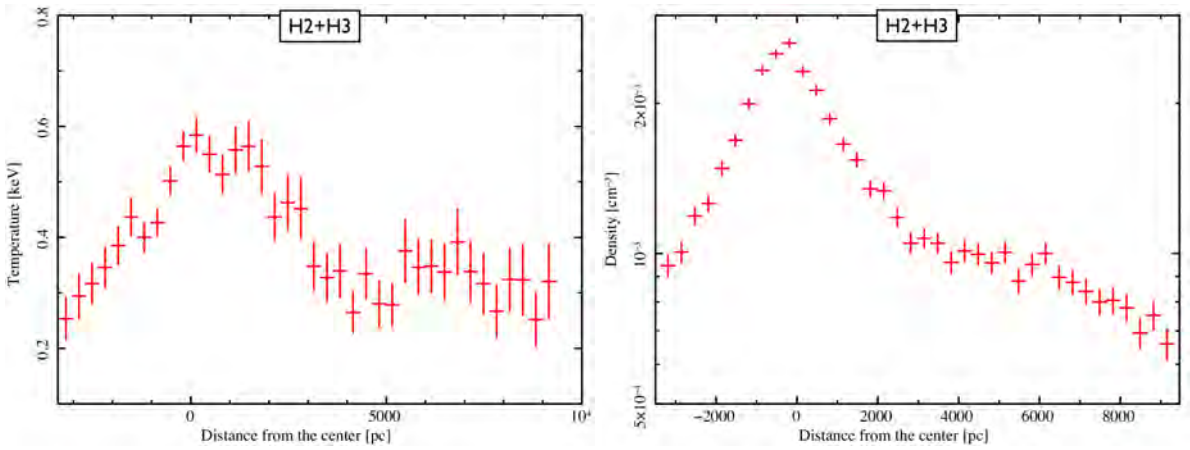

Figure 8.3 The estimated temperature profile from the hardness profile (left) and the estimated density profile from the surface brightness profile (right) in H2 and H3 regions.

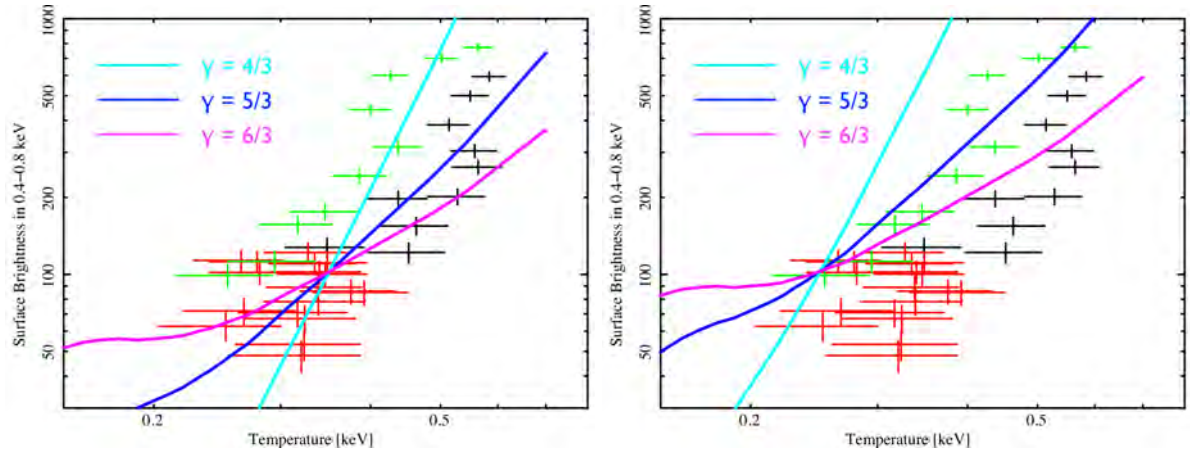

Figure 8.4 Expected temperatures from the hardness ratio in 0.8–1.0 keV to 0.4–0.8 keV vs the surface brightness profile in 0.4–0.8 keV. Black, green and red colors show the data sets obtained from the north disk, south disk and halo regions, respectively. Cyan, blue and magenta lines indicate power of 6, 3 and 2 corresponding to $\gamma = 4/3$, 5/3 and 6/3 respectively. These lines are plotted together to compare the data obtained from the north (left) and south (right) disk regions.

in units of keV, cm^{-3} and erg cm^{-3} s^{-1}, respectively. The density profile of the hot gas is derived from the surface brightness profile by fitting the surface brightness with a double exponential model, taking a square root of the double exponential model and normalizing the model to reproduce the observed density in the halo region. In this analysis, we regard $\Lambda(T)$ as a constant because in our interesting energy band of 0.3 to 0.6 keV $\Lambda(T)$ changes only ∼30%. We assume that the hot gas moves with a constant bulk speed v in the unit of km s^{-1} from the inner superwind region up to 10 kpc perpendicular to the disk plane along with the minor axis in the halo region. In

a specific time period Δt [s], the hot gas loses an energy of $\sim \Delta t \times n(R)\Lambda(T)$ which gives rise to a temperature reduction satisfying the following relation:

$$T(t + \Delta t) = T - \Delta t \frac{n(R)\Lambda(T)}{k}, \tag{8.4}$$

where k is Boltzmann constant in the unit of erg K^{-1}. Equation 8.3 can be written as

$$t_{cool}\ (R', t') \ = \ t_{cool}\ (R + v\Delta t, t + \Delta t) = \frac{kT(t + \Delta t)}{n(R + v\Delta t)\Lambda(T(t + \Delta t))}. \tag{8.5}$$

Utilizing these equations, we can extract arbitrary temperature and cooling time at a specific time or distance at the constant bulk velocity. Input parameters are an initial temperature at the starting point, i.e., in the inner superwind region, a time interval, the density profile and the bulk speed. As the density profile, we utilize the expected density profile from the surface brightness profile as shown in Figure 8.3. To extract the lower limit of the bulk velocity, the most steepest gradient within the 90 % error when we fit observed temperatures linearly in the halo region is utilized. Specifically, the best fit parameters of this linear fitting are (-1.0±11)×10^{-6} [keV / kpc] + 0.32±0.07 [keV]. Thus, we adopt -1.2×10^{-5} [keV / kpc] as the temperature gradient. As the initial temperature, we adopt 0.41 keV which is the highest temperature in the statistical error to extract the lower limit and Δt is selected to give enough data points over 100. Allowable ranges of the bulk speed reproducing the observed flat temperature are searched and resultant profiles are shown in Figure **??**. For the plasma with a temperature of 0.41 keV, roughly the bulk speed of >25 km s^{-1} is required to reproduce the obtained flat temperature profile.

8.4 Energetics for the Galactic-Scale Starburst-Driven Outflow

In this section, we discuss the galactic-scale starburst-driven outflow in the aspect of energetics. In this section, we discuss how much time has it been needed to supply an energy or a mass from the nuclear region to the halo region and the consistency with the observed SN rate or the typical starburst durations. Here, we assume that for simplicity the input energy and mass from the nuclear region reside in the halo region during their cooling time scales. The verification for this assumption is confirmed in the last part of this section. However, if the energy and mass loading to outside the host galaxy can not be negligible the expected timescales may underestimate. Total thermal energy in the nuclear region is ∼10^{54} erg while ∼10^{56} erg in the

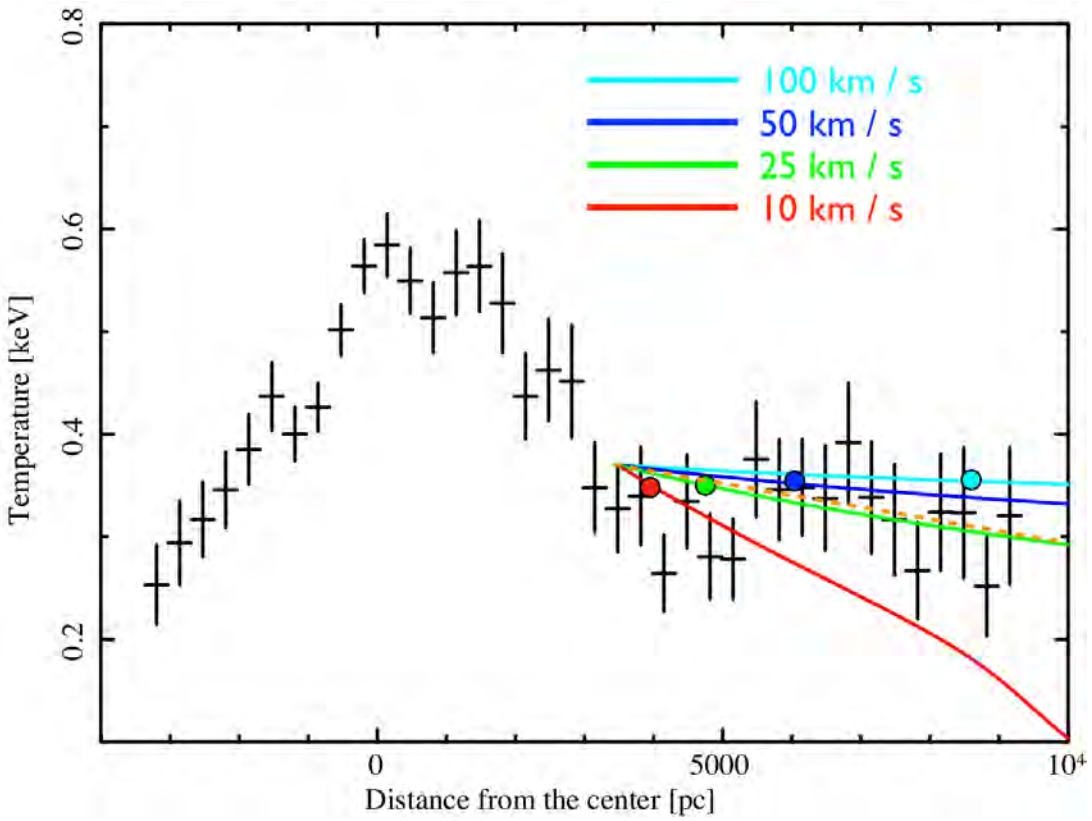

Figure 8.5 Temperature profile as a function of the distance from the galactic center along with the minor axis with bulk velocities of 10 (red), 25 (green), 50 (blue) and 100 (cyan) km s^{-1}, respectively. Circles on each line show travel time of 50 Myr for each bulk velocity from the innermost halo region.

halo region. Considering the typical lifetime $\sim 10^{4\text{-}5}$ yr of supernova remnants, the starburst duration of $10^{6\text{-}7}$ yr can supply the whole thermal energy from the nuclear to the halo region. This starburst duration is consistent with the typical starburst duration corresponding to the lifetime of massive stars. On the other hand, 10^5 type II supernovae are needed to explain the thermal energy in the halo region assuming 10^{51} erg per a supernova. This requires 0.01–0.1 supernova rate by assuming the typical starburst duration to be $10^{6\text{-}7}$ yr. This is consistent with the expected supernova rate of $\sim$0.1 or less in the nuclear region by radio observations (Rieke et al., 1988; Ulvestad & Antonucci, 1997). We can infer the total plasma mass of the hot gas using the volume and the observed plasma density. The calculated total plasma mass in both the nuclear and the halo regions are $\sim 8\times10^7$ $M_\odot$ and $\sim 3\times10^5$ $M_\odot$, respectively. Also from this point of view, considering the typical lifetime $\sim 10^{4\text{-}5}$ yr of supernova remnants, the starburst duration of $\sim 3\times10^{6\text{-}7}$ yr can provide the whole plasma mass from the nuclear to the halo region. These timescales are enough smaller than that of the cooling time of the hot gas (>1 Gyr) in the halo region.

8.5 Hot Gas Outflow Observation with Next Generation X-ray Satellite, *Astro-H*

In this thesis, to verify the galactic-scale starburst-driven outflow observationally, we focus on the chemical aspect because it seems to be difficult to detect an outflow motion of the hot gas on the order of several 100 km s^{-1} expected from observations using present X-ray CCDs on board X-ray observatories in operation. In the near future, next generation X-ray satellite, *Astro-H* (Takahashi et al., 2010), will be launched in 2013. The *Astro-H* mission, 6th in series of the ISAS/JAXA's X-ray astronomy program, is a combination of X-ray spectroscopy (3-80 keV) provided by multi-layer coating, focusing hard X-ray mirrors and pixel detectors, and high energy-resolution soft X-ray spectroscopy (0.3–10 keV) supplied by the Soft X-ray Spectrometer (hereafter SXS) (Mitsuda et al., 2010). Especially, here, we emphasize the capability of the SXS associated with a measurement of the hot gas outflow. The SXS can achieve high resolution below 10 eV (requirement: 7 eV, goal: 4 eV) which is over an order of magnitude higher than those of the present X-ray CCDs and spectroscopy for spatially extended sources at the same time (Mitsuda et al., 2010). Both the *Astro-H* and the expected spectrum obtained from the SXS are shown in Figure 8.6. Finally, we show the expected spectrum assuming an energy resolution 5 eV, a temperature of 0.2 keV, a flux of 10^{-13} erg s^{-1} cm^{-2} in 0.5–10 keV which is comparable with the hot gas in the halo region of NGC 253, an exposure time 1 Ms and a bulk speed of 100 km s^{-1} as shown in Figure 8.6. We can observe the shift from the redshift of 0 and obtain the hot gas outflow velocity of 73^{+26}_{-25}, 110^{+24}_{-20} and 100^{+17}_{-14} km s^{-1} with exposure times of 200, 500 and 1000 ks, respectively. Thus, we expect the *Astro-H* to reveal the picture of the galactic-scale starburst-driven outflow.

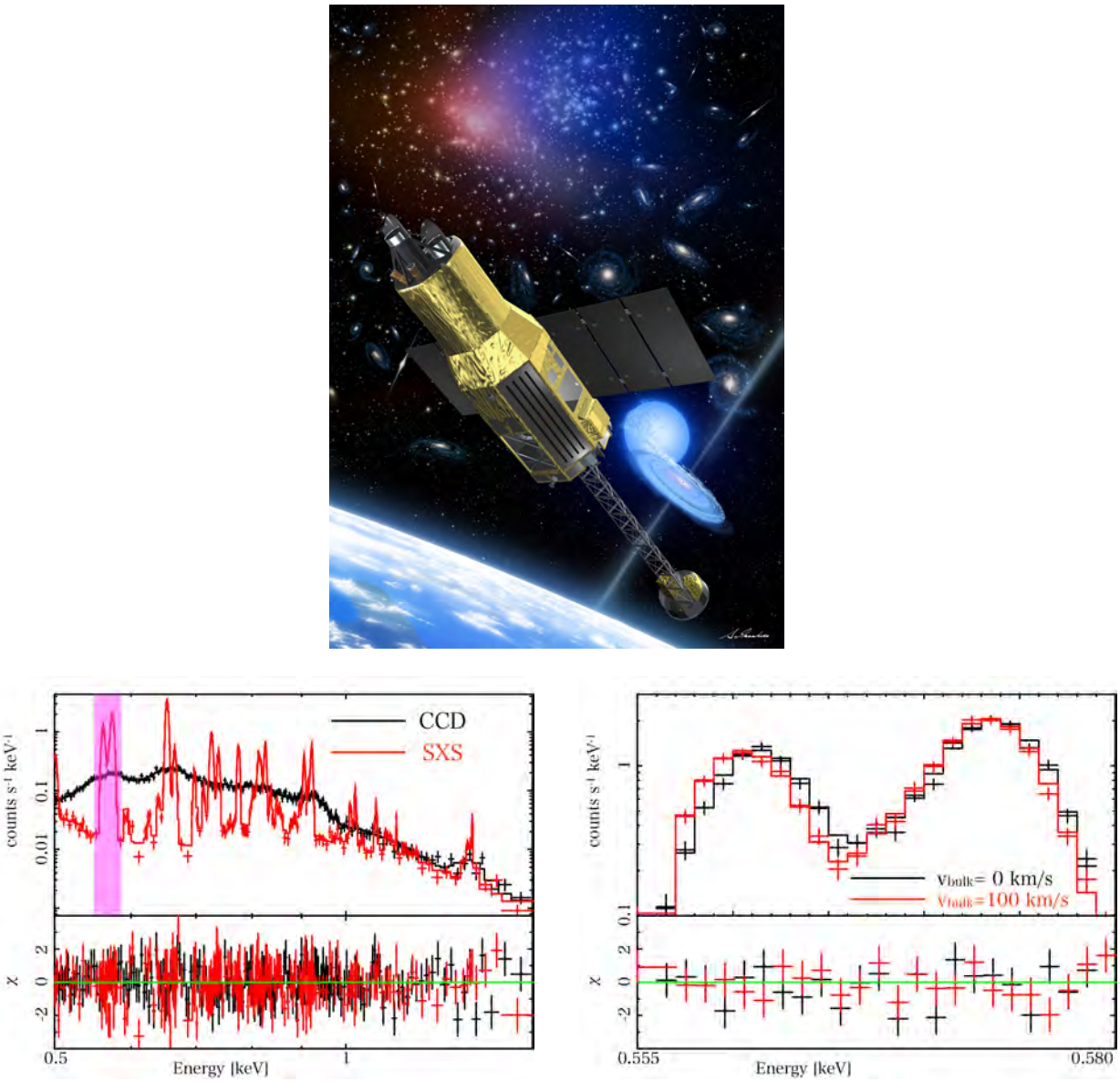

Figure 8.6 Top: overview of the next generation satellite, *Astro-H* (http://astro-h.isas.jaxa.jp/gallery/satelite/). Bottom left: spectrum comparison obtained from the present X-ray CCDs (black) and the SXS on board *Astro-H* (red). Bottom right: close-up view of the magenta colored region in the bottom left Figure. This narrow band includes oxygen forbidden (561 eV) and resonance (574 eV) emission lines. As a comparison, the redshifted thermal plasma (red) with a bulk speed of 100 km s^{-1} is also plotted. These simulations are provided by Norio Sekiya (private communication).

9 Conclusions

We have analyzed starburst galaxy NGC 253 utilizing three X-ray observatories to observationally investigate the possible galactic-scale outflow from the nuclear region, through the disk and the halo, to the intergalactic space. We mainly focused on the following aspects:

- The chemical composition of the gas to consider the possibility of SN II origin associated with the starburst activity.
- The temperature and density distribution of the disk and halo gas to investigate if the distribution can be explained by gas expansion and to constrain the bulk velocity.

We analyzed 4 regions in NGC 253 as we have shown in previous chapters. In this chapter, we combine these results and to obtain conclusions and suggestions on the outflow of NGC 253. The followings are our main results.

1. In the nuclear star-forming region of NGC 253, an X-ray bright region of $8'' \times 3''$ (128×48 pc^{-2}) above 4 keV is found. There are intense Fe XXV and Fe I line emissions. The surface brightness of the Fe XXV emission line is not uniform and associated with molecular clouds within $0.5''$. The neutral Fe I line seems to be more extended. The sum of emission from the point sources is difficult to reproduce the luminosity of the hard X-ray emission unless the extreme number of the sources are assumed. The 10–1000 SNRs due to high star forming activity can supply the mass and energy of the extended hot plasma.
2. The X-ray emission in the disk and halo of NGC 253 are investigated. A 100 pc scale superwind outflow cone which is found by Hα emission is bright in X-rays. The X-ray spectra from the superwind, disk and halo regions are well described by $kT = \sim$0.2 keV and 0.6 keV thin thermal plasma emission characterized by lines from O, Ne, Mg and Si. The hardness profiles of the disk region decreases rapidly, while that in the halo region is flat out to 10 kpc. The flatness in the halo indicates that the temperature does not vary more than $\sim 20\%$.
3. For three regions, i.e., the inner superwind, disk and halo regions, the abundance patterns relative to Fe obtained by the two-temperature thin thermal

emission model are consistent within the statistical errors. The abundance pattern is consistent with the SN II origin.

4. An excess component is found in surface brightness profiles of a part of the halo region defined as the horn region in this thesis, which is characterized also in the IR observation. No significant change on temperature and abundance patterns suggests that the horn region is a part of the halo or of the halo origin.
5. We discussed how gas expands from the disk to the halo, assuming the halo gas originates from the hot gas produced by the starburst activity in the disk. The density and temperature distribution estimated by the hardness ratio and the surface brightness suggests that the gas is adiabatically expands in the disk region while it freely expands in the halo region. From the condition that the gas is not cooled by radiative cooling, we estimated that the bulk velocity to be $\gtrsim 25$ km s^{-1}.

Appendix A
Systematic error on abundance patterns

To evaluate a systematic error on abundance patterns, we derive two-dimensional contours for each element relative to Fe in the best fit models of each region and also the one-temperature model of the halo region. Figures A.1, A.2, A.3 and A.4 show resultant contours and the best fit values on abundance patterns are summarized in Table A.1.

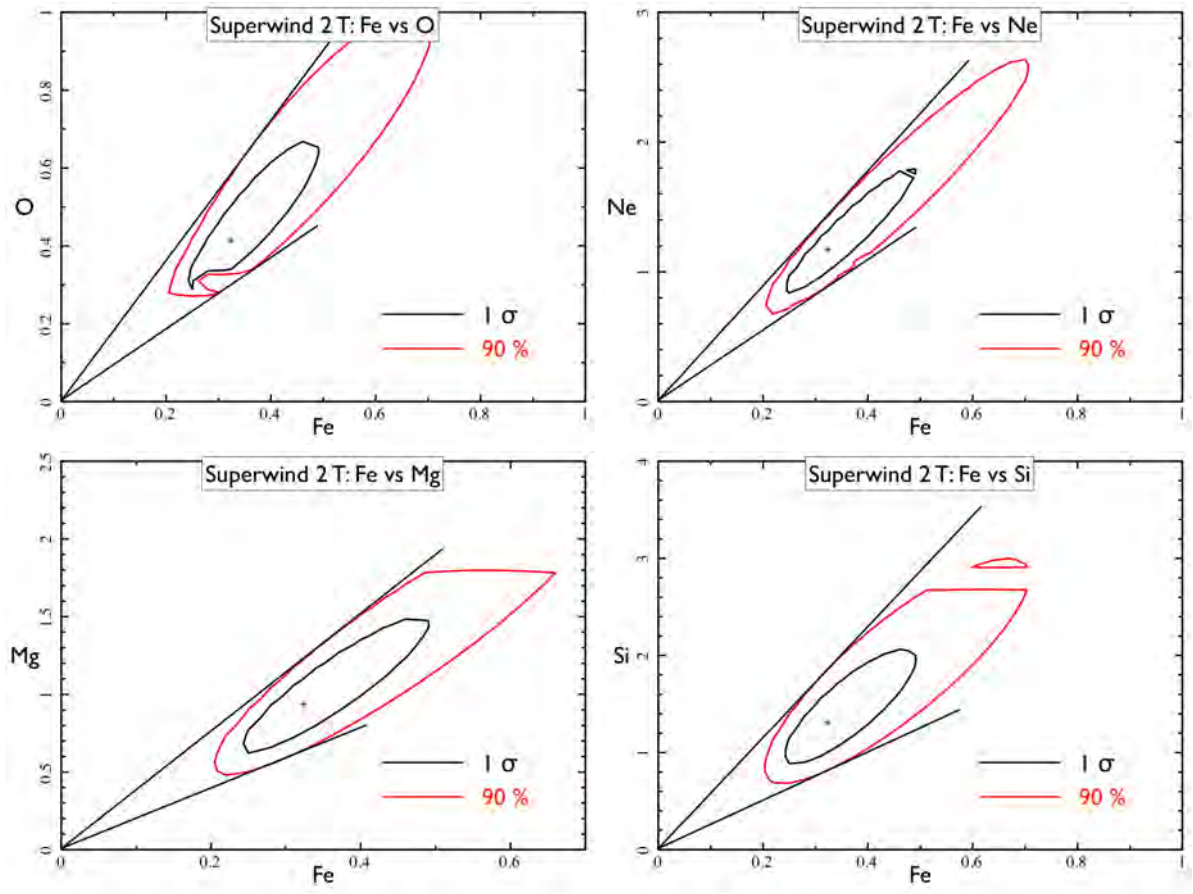

Figure A.1 Two contours of each element relative to Fe for the two-temperature model in the superwind region.

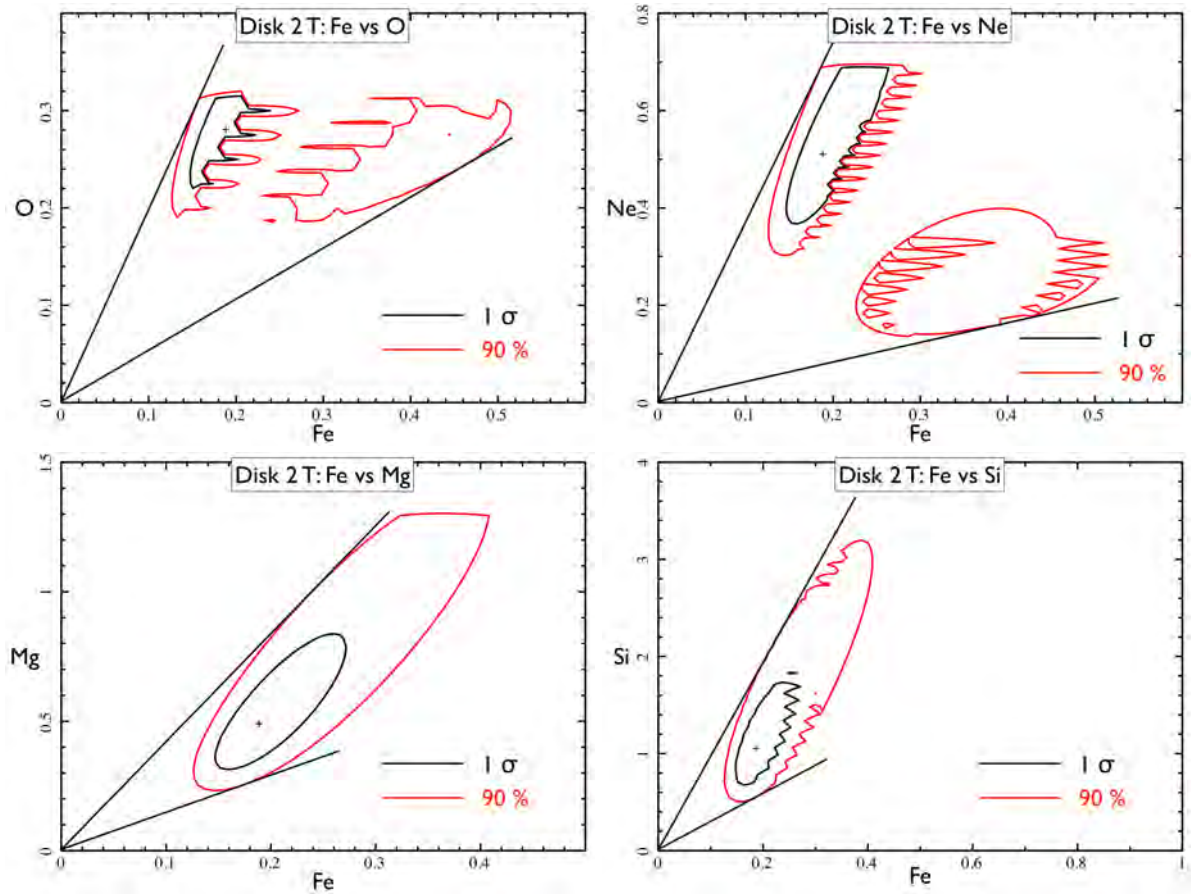

Figure A.2 The same as Figure A.1 but the disk region.

Table A.1 Abundance patterns from two contours in each model of each region.

Region	Superwind	Disk	Halo	
Model	$2T$	$2T$	$2T$	$1T$
O/Fe*	$1.3^{+0.5}_{-0.4}$	$1.5^{+0.5}_{-0.9}$	$1.5^{+0.6}_{-0.5}$	$1.9^{+0.7}_{-0.5}$
Ne/Fe*	3.6±0.9	$2.7^{+1.0}_{-2.3}$	$2.7^{+0.9}_{-1.4}$	$2.6^{+0.7}_{-0.5}$
Mg/Fe*	2.9±0.9	$2.6^{+1.6}_{-1.1}$	$3.9^{+1.4}_{-1.2}$	4.7±1.5
Si/Fe*	$4.1^{+1.7}_{-1.6}$	$5.6^{+4.2}_{-2.6}$	$4.2^{+2.5}_{-2.1}$	$4.6^{+4.5}_{-4.6}$

* Abundance ratios of [Z/Fe] to solar ratios of $[Z/Fe]_{\odot}$.

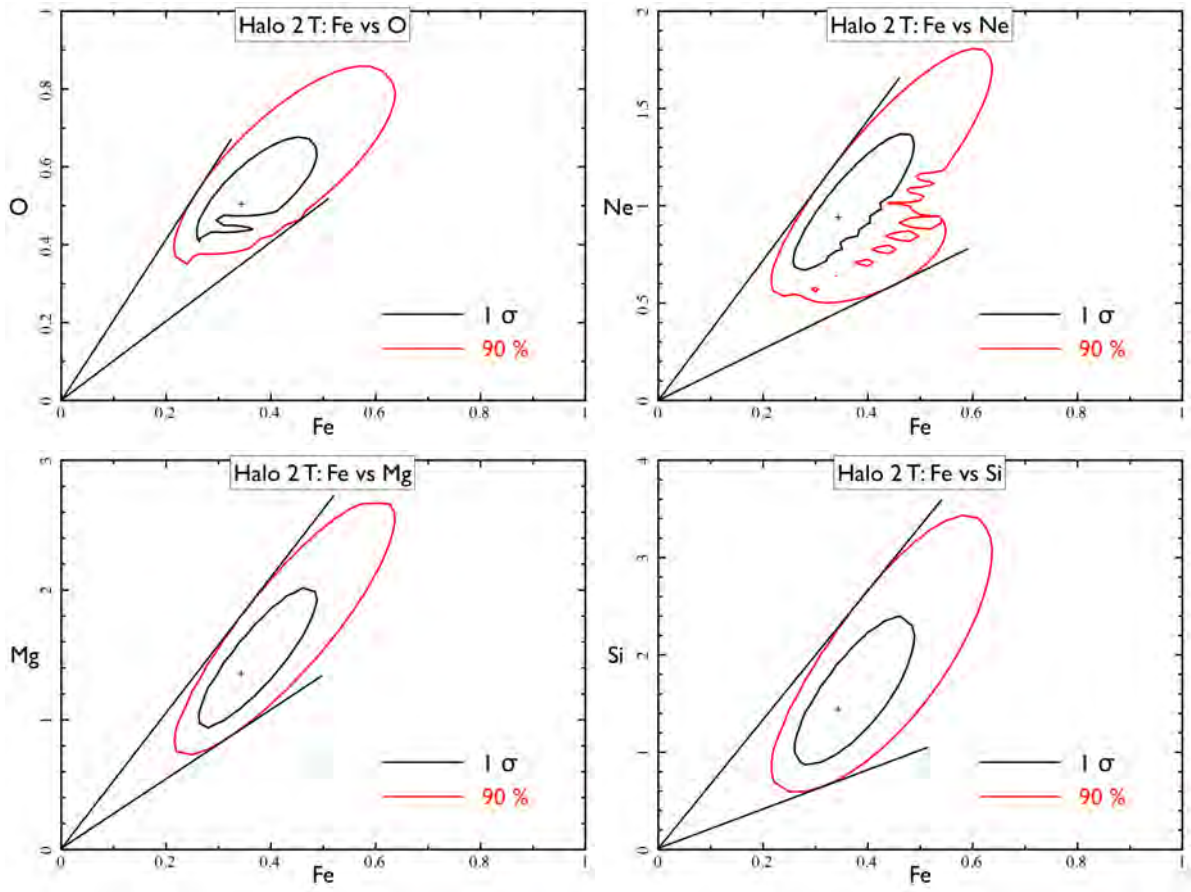

Figure A.3 The same as Figure A.1 but the halo region.

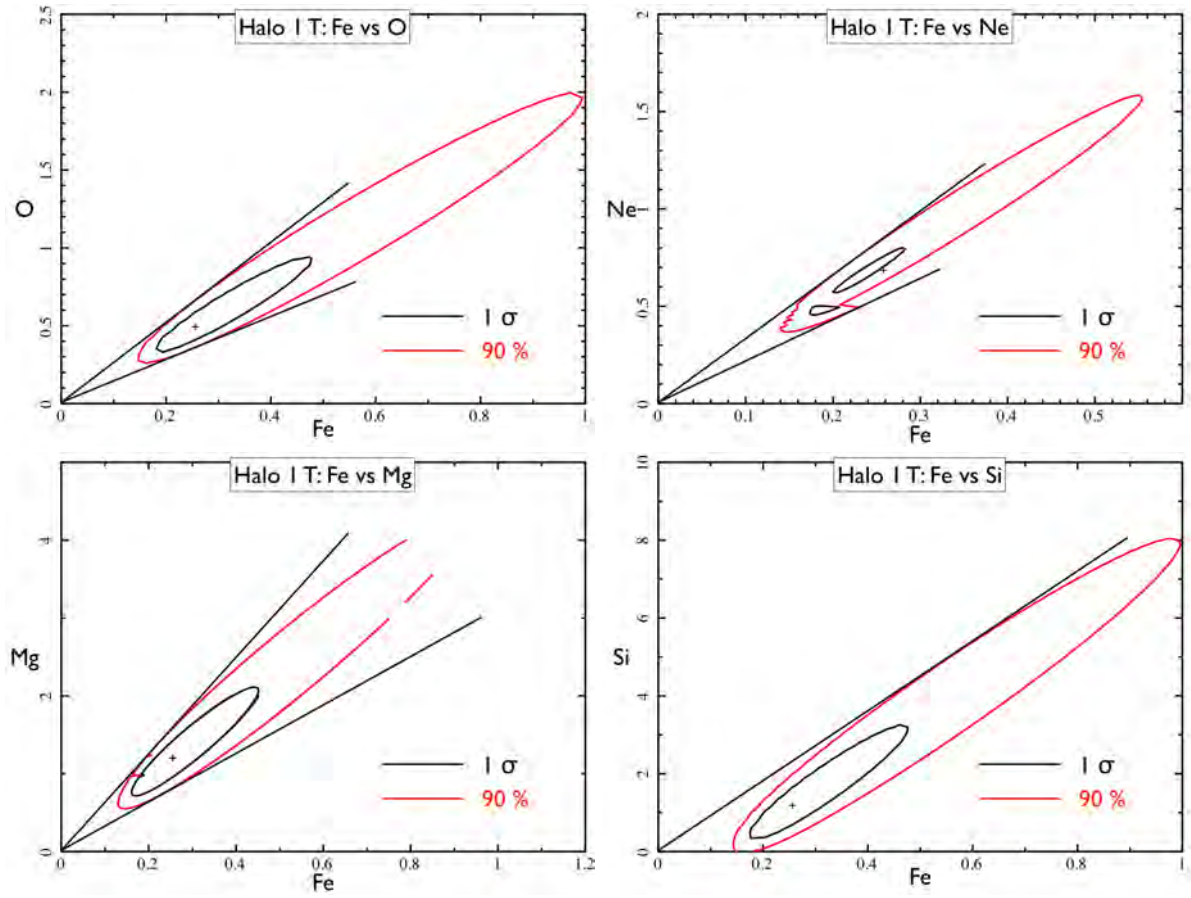

Figure A.4 The same as Figure A.3 but for the one-temperature model.

Appendix B
Conversion to number ratios

In this thesis, we convert the obtained value normalized by solar ratios using the specific abundance table (Anders & Grevesse, 1989) in fitting processes to number ratios to Fe atom which is independent of the abundance table we adopt. Throughout this thesis, we adopt the abundance table of Anders & Grevesse (1989). Thus, for instance, the observed abundance pattern O/Fe of 1.2 is converted to the number ratio relative to Fe atom of 1.2×(8.51e-4/4.68e-5) ∼22 tabulated in Table B.1.

Table B.1 All abundances are number relative to H (Anders & Grevesse, 1989).

Element		Element		Element	
H	1.00e+0	Na	2.14e-6	Sc	1.26e-9
He	9.77e-2	Mg	3.80e-5	Ti	9.77e-8
Li	1.45e-11	Al	2.95e-6	V	1.00e-8
B	1.41e-11	Si	3.55e-5	Cr	4.68e-7
Be	3.98e-10	P	2.82e-7	Mn	2.45e-7
C	3.63e-4	S	1.62e-5	Fe	4.68e-5
N	1.12e-4	Cl	1.88e-7	Co	8.60e-8
O	8.51e-4	Ar	3.63e-6	Ni	1.78e-6
F	3.63e-8	K	1.32e-7	Cu	1.62e-8
Ne	1.23e-4	Ca	2.29e-6	Zn	3.98e-8

References

Abdo, A. A., et al. 2010, ApJL, 709, L152

Akamatsu, H., Hoshino, A., Ishisaki, Y., Ohashi, T., Sato, K., Takei, Y., & Ota, N. 2011, PASJ, 63, 1019

Anders, E., & Grevesse, N. 1989, gca, 53, 197

Bauer, M., Pietsch, W., Trinchieri, G., Breitschwerdt, D., Ehle, M., Freyberg, M. J., & Read, A. M. 2008, AAP, 489, 1029

Bauer, M., Pietsch, W., Trinchieri, G., Breitschwerdt, D., Ehle, M., & Read, A. 2007, A&A, 467, 979

Boller, T., Keil, R., Hasinger, G., Costantini, E., Fujimoto, R., Anabuki, N., Lehmann, I., & Gallo, L. 2003, A&A, 411, 63

Boomsma, R., Oosterloo, T. A., Fraternali, F., van der Hulst, J. M., & Sancisi, R. 2005, A&A, 431, 65

Buote, D. A., Zappacosta, L., Fang, T., Humphrey, P. J., Gastaldello, F., & Tagliaferri, G. 2009, ApJ, 695, 1351

Carral, P., Hollenbach, D. J., Lord, S. D., Colgan, S. W. J., Haas, M. R., Rubin, R. H., & Erickson, E. F. 1994, ApJ, 423, 223

Cooper, J. L., Bicknell, G. V., Sutherland, R. S., & Bland-Hawthorn, J. 2008, ApJ, 674, 157

Dalcanton, J. J., et al. 2009, ApJS, 183, 67

de Vaucouleurs, G. 1958, ApJ, 128, 465

Ezuka, H., & Ishida, M. 1999, ApJS, 120, 277

Favata, F., Micela, G., & Sciortino, S. 1995, A&A, 298, 482

Garnett, D. R. 2002, ApJ, 581, 1019

Grimm, H.-J., Gilfanov, M., & Sunyaev, R. 2003, MNRAS, 339, 793

Heckman, T. M., Armus, L., & Miley, G. K. 1990, ApJS, 74, 833

Heesen, V., Beck, R., Krause, M., & Dettmar, R.-J. 2009, Astronomische Nachrichten, 330, 1028

—. 2011, A&A, 535, A79

Henkel, C., Tarchi, A., Menten, K. M., & Peck, A. B. 2004, A&A, 414, 117

House, L. L. 1969, ApJS, 18, 21

Hughes, J. P., Hayashi, I., & Koyama, K. 1998, ApJ, 505, 732

Ishisaki, Y., et al. 2007, PASJ, 59, 113

Israel, F. P., White, G. J., & Baas, F. 1995, A&A, 302, 343

Iwamoto, K., Brachwitz, F., Nomoto, K., Kishimoto, N., Umeda, H., Hix, W. R., & Thielemann, F.-K. 1999, ApJS, 125, 439

Jansen, F., et al. 2001, A&A, 365, L1

Kalberla, P. M. W., Burton, W. B., Hartmann, D., Arnal, E. M., Bajaja, E., Morras, R., & Pöppel, W. G. L. 2005, A&A, 440, 775

Kaneda, H., Yamagishi, M., Suzuki, T., & Onaka, T. 2009, ApJL, 698, L125

Katayama, H., Takahashi, I., Ikebe, Y., Matsushita, K., & Freyberg, M. J. 2004, A&A, 414, 767

Kennicutt, Jr., R. C. 1998, ApJ, 498, 541

Keto, E., Hora, J. L., Fazio, G. G., Hoffmann, W., & Deutsch, L. 1999, ApJ, 518, 183

Kokubun, M., et al. 2007, PASJ, 59, 53

Konami, S., Matsushita, K., Tsuru, T. G., Gandhi, P., & Tamagawa, T. 2011, PASJ, 63, 913

Koribalski, B., Whiteoak, J. B., & Houghton, S. 1995, PASA, 12, 20

Koyama, K., et al. 2007, PASJ, 59, 23

Kushino, A., Ishisaki, Y., Morita, U., Yamasaki, N. Y., Ishida, M., Ohashi, T., & Ueda, Y. 2002, PASJ, 54, 327

Lehnert, M. D., & Heckman, T. M. 1996, ApJ, 472, 546

Lumb, D. H., Warwick, R. S., Page, M., & De Luca, A. 2002, A&A, 389, 93

Martín, S., Aladro, R., Martín-Pintado, J., & Mauersberger, R. 2010, A&A, 522, A62

Matsubayashi, K., Sugai, H., Hattori, T., Kawai, A., Ozaki, S., Kosugi, G., Ishigaki, T., & Shimono, A. 2009, ApJ, 701, 1636

Mauersberger, R., Henkel, C., Wielebinski, R., Wiklind, T., & Reuter, H.-P. 1996, A&A, 305, 421

Misaki, K., et al. 2004, in Society of Photo-Optical Instrumentation Engineers (SPIE) Conference Series, Vol. 5168, Society of Photo-Optical Instrumentation Engineers (SPIE) Conference Series, ed. O. Citterio & S. L. O'Dell, 294–305

Mitsuda, K., et al. 2007, PASJ, 59, 1

Mitsuda, K., et al. 2010, in Society of Photo-Optical Instrumentation Engineers (SPIE) Conference Series, Vol. 7732, Society of Photo-Optical Instrumentation Engineers (SPIE) Conference Series

Mitsuishi, I., Yamasaki, N. Y., & Takei, Y. 2011, ApJL, 742, L31

Mori, H., et al. 2005, PASJ, 57, 245

Müller-Sánchez, F., González-Martín, O., Fernández-Ontiveros, J. A., Acosta-Pulido, J. A., & Prieto, M. A. 2010, ApJ, 716, 1166

Muno, M. P., et al. 2003, ApJ, 589, 225

Nobukawa, M., et al. 2008, PASJ, 60, 191

Nomoto, K., Tominaga, N., Umeda, H., Kobayashi, C., & Maeda, K. 2006, Nuclear Physics A, 777, 424

O'Halloran, B., Satyapal, S., & Dudik, R. P. 2006, ApJ, 641, 795

Origlia, L., Ranalli, P., Maiolino, R., & Comastri, A. 2005, in Astrophysics and Space Science Library, Vol. 329, Starbursts: From 30 Doradus to Lyman Break Galaxies, ed. R. de Grijs & R. M. González Delgado, 56P

Pagel, B. E. J. 2002, in Astronomical Society of the Pacific Conference Series, Vol. 253, Chemical Enrichment of Intracluster and Intergalactic Medium, ed. R. Fusco-Femiano & F. Matteucci, 489

Pence, W. D. 1980, ApJ, 239, 54

Persic, M., et al. 1998, A&A, 339, L33

Pettini, M., Shapley, A. E., Steidel, C. C., Cuby, J.-G., Dickinson, M., Moorwood, A. F. M., Adelberger, K. L., & Giavalisco, M. 2001, ApJ, 554, 981

Pietsch, W., Vogler, A., Klein, U., & Zinnecker, H. 2000, A&A, 360, 24

Pietsch, W., et al. 2001, A&A, 365, L174

Pizzolato, N., Ventura, P., D'Antona, F., Maggio, A., Micela, G., & Sciortino, S. 2001, A&A, 373, 597

Ptak, A., Serlemitsos, P., Yaqoob, T., Mushotzky, R., & Tsuru, T. 1997, AJ, 113, 1286

Radovich, M., Kahanpää, J., & Lemke, D. 2001, A&A, 377, 73

Ranalli, P., Comastri, A., Origlia, L., & Maiolino, R. 2008, MNRAS, 386, 1464

Read, A. M., & Ponman, T. J. 2003, A&A, 409, 395

Rieke, G. H., Lebofsky, M. J., & Walker, C. E. 1988, ApJ, 325, 679

Rogel, A. B., Cohn, H. N., & Lugger, P. M. 2008, ApJ, 675, 373

Sakamoto, K., Mao, R.-Q., Matsushita, S., Peck, A. B., Sawada, T., & Wiedner, M. C. 2011, ApJ, 735, 19

Serlemitsos, P. J., et al. 2007, PASJ, 59, 9

Shapley, A. E., Steidel, C. C., Pettini, M., & Adelberger, K. L. 2003, ApJ, 588, 65

Shopbell, P. L., & Bland-Hawthorn, J. 1998, ApJ, 493, 129

Songaila, A. 1997, ApJL, 490, L1

Strickland, D. K., & Heckman, T. M. 2007, ApJ, 658, 258

Strickland, D. K., Heckman, T. M., Colbert, E. J. M., Hoopes, C. G., & Weaver, K. A. 2004, ApJS, 151, 193

Strickland, D. K., Heckman, T. M., Weaver, K. A., & Dahlem, M. 2000, AJ, 120, 2965

Strickland, D. K., Heckman, T. M., Weaver, K. A., Hoopes, C. G., & Dahlem, M. 2002, ApJ, 568, 689

Strickland, D. K., & Stevens, I. R. 2000, MNRAS, 314, 511

Strüder, L., et al. 2001, A&A, 365, L18

Suchkov, A. A., Berman, V. G., Heckman, T. M., & Balsara, D. S. 1996, ApJ, 463, 528

Sutherland, R. S., & Dopita, M. A. 1993, ApJS, 88, 253

Takahashi, T., et al. 2010, in Society of Photo-Optical Instrumentation Engineers (SPIE) Conference Series, Vol. 7732, Society of Photo-Optical Instrumentation Engineers (SPIE) Conference Series

Tawa, N., et al. 2008, PASJ, 60, 11

Torrejón, J. M., Schulz, N. S., Nowak, M. A., & Kallman, T. R. 2010, ApJ, 715, 947

Tripp, T. M., Savage, B. D., & Jenkins, E. B. 2000, ApJL, 534, L1

Tsuru, T. G., et al. 2007, PASJ, 59, 269

Turner, J. L., & Ho, P. T. P. 1985, ApJL, 299, L77

Turner, M. J. L., et al. 2001, A&A, 365, L27

Ulvestad, J. S., & Antonucci, R. R. J. 1997, ApJ, 488, 621

Veilleux, S., Cecil, G., & Bland-Hawthorn, J. 2005, ARA&A, 43, 769

Vogler, A., & Pietsch, W. 1999, A&A, 342, 101

Walter, R., et al. 2006, A&A, 453, 133

Weaver, K. A., Heckman, T. M., Strickland, D. K., & Dahlem, M. 2002, ApJL, 576, L19

Webster, B. L., & Smith, M. G. 1983, MNRAS, 204, 743

Weiß, A., Kovács, A., Güsten, R., Menten, K. M., Schuller, F., Siringo, G., & Kreysa, E. 2008, A&A, 490, 77

Westmoquette, M. S., Smith, L. J., & Gallagher, III, J. S. 2011, MNRAS, 414, 3719

Yamasaki, N. Y., Sato, K., Mitsuishi, I., & Ohashi, T. 2009, PASJ, 61, 291

Yoshino, T., et al. 2009, PASJ, 61, 805

Yoshizawa, M., & Wakamatsu, K. 1975, A&A, 44, 363